

MODELLING OF POTENTIAL ENERGY SURFACES FOR PHOTOCHEMISTRY: CONICAL INTERSECTIONS AND APPLICATION TO OPTICAL CONTROL

Sergi Ruiz-Barragán

Dipòsit legal: Gi. 1856-2014
<http://hdl.handle.net/10803/283964>



<http://creativecommons.org/licenses/by-nc-nd/4.0/deed.ca>

Aquesta obra està subjecta a una llicència Creative Commons Reconeixement-NoComercial-SenseObraDerivada

Esta obra está bajo una licencia Creative Commons Reconocimiento-NoComercial-SinObraDerivada

This work is licensed under a Creative Commons Attribution-NonCommercial-NoDerivatives licence

DOCTORAL THESIS:

Modelling of potential energy surfaces for
photochemistry: Conical intersections and
application to optical control

Sergi Ruiz-Barragán
2014

Doctoral programme in Experimental Sciences and Sustainability

Supervised by:
Dr. Lluís Blancafort

This manuscript has been presented to opt for the doctoral degree
from the University of Girona

Dr. Lluís Blancafort, professor agregat del departament de Química de la Universitat de Girona,

I DECLARE:

That the thesis titles “**Modelling of potential energy surfaces for photochemistry: Conical intersections and application to optical control**”, presented by Sergi Ruiz to obtain a doctoral degree, has been completed under my supervision and meets the requirements to opt for an International Doctorate.

For all intents and purposes, I hereby sign this document.

Signature

Girona, 31st July 2014

*“No passa res si caus,
ens passa a tots,
l’importat és aixecar-se sempre.”*

Acknowledgments

Primer de tot m'agradaria donar les gracies al Ministerio de Ciencia e Innovación per la beca pre-doctoral BES-2009-029177 associada al projecte CTQ2008-06696, del qual també m'he beneficiat durant la meva formació com investigador.

Seguint amb aquesta línia, m'agradaria agrair al meu tutor la oportunitat que em va donar amb la beca FPI associada a un tema totalment nou per mi, que m'ha acabat resultant apassionant i que m'ha acabat agradant molt. A més a més, es va saber adaptar al que a mi més m'agradava, que era la programació. Gracies Lluís per aquests anys, he apres moltíssim.

Dins del IQC, hi ha un altre tutor important per mi, que em va guiar al final de la carrera i al inici del doctorat, amb el que vaig fer el treball de final de màster. Vaig aprendre molt amb tu, sobretot programació. Gracies Pedro.

L'IQC també m'ha donat moltes satisfaccions, no només a nivell acadèmic.

Dins del grup mantindre molts amics i companys, amb els que he passat molts grans moments: pelegrinatges IQC, congressos, cremats o les JODETE; i bon moments al despatx del parc i al 177. Són uns 7 anys des de el primer dia que vaig entrar al 166, amb un Saboo a la mà. Moltes petites anècdotes. Gracies Dani, Carme, Eloy, Silvia, Edu, Ferran, Pata, Cris, Eugene, Marc, Vero. Amb menció especial als que van fer el màster amb mi, que va ser força divertit, Laia, Merce (tot i que no ets IQC!) i Majid.

Aquesta tesis no hagués estat possible sense el recolzament de la meva família. Com molts sabeu, la meva família m'ha donat moltes avan-

tatges i facilitats per fer el que he volgut i com ho he volgut. Se que us sentiu orgullosos del que he aconseguit, però us heu se sentir més orgullosos dels esforços que heu fet per mi. Gracies papa i mama. Potser de forma més moral, els meus amics i coneguts han estat també un punt essencial en aquest anys de tesis. Molta gent ha estat en el meu costat en aquest anys, però en primer lloc m'agradaria donar un moment per tota la gent de l'associació Aula Manga UdG. Són molts esforços, però la recompensa sol valer la pena. Grans fites que hem anat aconseguit durant aquest temps acompanyat de moments realment divertits. Menció especial per la secretaria, que d'una manera o d'una altre m'ha anat ajudant molt, no només en l'associació. Sobretot en l'inici d'aquesta tesis. Gracies Iria. En segon lloc voldria agrair a una amiga molt especial, de les persones més importants per mi. M'ha ajudat en tot i més i sempre ha estat al meu costat, encara que no ens podem veure massa. El viatge a Japó va ser molt divertit, realment. Gracies Miru. Finalment, i possiblement el més important per mi ara mateix, gracies Andrea. Aquest tram final de tesis ha estat realment molt agradable amb tu al meu costat. Gracies.



List of Publications

This thesis is presented as a compendium of publications.

Published articles included in this thesis:

1. S. Ruiz-Barragán, M. Robb, Ll. Blancafort, **Conical Intersection Optimization Based on a Double Newton-Raphson Algorithm Using Composed Steps**, *J. Chem. Theory Comput.* (Impact factor: 5.389, 1st quartile), 9, **2013**, 1433-1442
2. S. Ruiz-Barragán, Ll. Blancafort, **Photophysics of fulvene under the non-resonant stark effect. Shaping the conical intersection seam**, *Faraday Discuss.* (Impact factor: 3.821, 1st quartile), 163, **2013**, 497-512

Articles in preparation included in this thesis:

3. S. Ruiz-Barragán, K. Morokuma, Ll. Blancafort, **Conical Intersection Optimization using Composed Steps inside the ONIOM scheme. QM:MM with mechanical embedding and microiterations**

List of Abbreviations

B-O	Born-Oppenheimer
BFGS	Broyden-Fletcher-Goldfarb-Shanno
BS	Branching Space
CASSCF	Complete Active Space Self Consistent Field
CG	Composed Gradient
CI	Conical Intersection
CS	Composed Steps
DPDBF	DiPhenyl DiBenzoFulvene
DNR	Double Newton-Raphson
EE	Electronic Embedding
ES	Excited State
FC	Frank-Condon
GS	Ground State
HF	Hartree-Fock
IS	Intersection Space
LA	Link Atom
LAC	Link Atom Connection
LAH	Link Atom Host
MCSCF	Multi-Configurational Self-Consistent Field
MCTDH	Multi-Configurational Time-Dependent Hartree
ME	Mechanical Embedding
MECI	Minimum Energy Conical Intersection
MM	Molecular Mechanics
N-R	Newton-Raphson
ONIOM	Own N-layer Integrated molecular Orbital molecular Mechanics

PEH	Potential Energy Hypersurface
PES	Potential Energy Surface
QM	Quantum Mechanics
SCF	Self-Consistent Field
TDSE	Time-Dependent Schrodinger Equation
TISE	Time-Independent Schrodinger Equation
TS	Transition State
UFF	Universal Force Field

List of Tables

6.1	Averages of MECI searches with CG, CG-CS and DNR algorithms, including the distance from starting point, number of cycles and energy difference.	121
6.2	Average of number of steps required to reach degeneracy threshold of 0.005 and 0.001 a.u. and the relative energy of S_1 with respect to the MECI for the eleven test cases, with DNR-CS, CG-CS and CG algorithms.	121
6.3	Averages of number of cycles of MECI searches with CG, CG-CS and DNR algorithms inside ME-ONIOM with 18 systems.	124
6.4	Relative energy of the critical points of DPDBF inside the totally frozen crystal cage, with respect to the minimum. Values in eV.	127
6.5	Relative energy of the critical points of the DPDBF inside crystal cage with one free solvation layer, with respect to the minimum. Values in eV	127

List of Figures

1.1	Scheme of absorption (a) and emission (b) in atoms. Each line is a transition to a low state in emission or a high state in absorption.	14
1.2	Scheme of <i>Stokes' shift</i> between molecular absorption (A) and emission (E) spectra.	16
1.3	Scheme of Frank-Condon principle and Kasha's rule between two PES of two electronic states with their associated vibronic states. The arrows correspond to absorption (A) and emission (E) processes.	18
1.4	Two examples of radiationless relaxation of two singlets (a) and singlet and excited triplet state (b).	19
1.5	a) Typical form of a conical intersection plotted in the direction of the BS. b) Example of seam plotted in one direction of the BS and the other direction with large second order components.	21
1.6	The two kinds of CI, sloped (a) and peaked (b), with the typical trajectories (shown with red arrows): in the sloped CI, the trajectories go to the GS minimum and, in the peaked CI, a photoproduct is accessible.	23
1.7	a) Molecular structure of ethylene in the minimum potential energy point of S_0 . b) Molecular structure of the MECI between the S_1 - S_0 states of the ethylene.	25

1.8	Potential energy plot of three states, S_0 , T_1 and S_1 , of ethylene along the rotation of the double bond with all other coordinates fixed. The energies correspond to CAS(2,2) calculations.	26
1.9	Energy scheme of retinal cis/trans isomerisation inside rhodopsin. The structures were adapted from Wikipedia.org ¹⁶ and the retinal moiety of the PSB is displayed.	27
1.10	Molecular structure of fulvene in the minimum potential energy point of S_0	28
1.11	Principal modes of fulvene: the totally symmetric bond alternating mode (a), the non-totally symmetric bond stretch coordinate (b), pyramidalisation (c) and rotation (d).	29
1.12	Energy plot along the totally symmetric bond alternating mode in 0° rotation angle and molecular structures of the CI between S_1 - S_0 and $(S_0)_{min}$ and the S_0 of fulvene	30
1.13	3D energy plot of the S_1 and S_0 states of fulvene along the totally symmetric bond alternating mode and CH_2 rotation coordinate with molecular structure of the CI between S_1 - S_0 at $\varphi = 0^\circ$ and $\varphi = 90^\circ$	30
1.14	Seam energy plot of fulvene along the CH_2 rotation coordinate and molecular structure of the MECI.	31
2.1	Potential Energy Surface of two states in two coordinates.	37
2.2	Schematic representation of the adiabatic and diabatic PES of two states.	40
2.3	Scheme with the orbitals in HF picture of the orbital division in a CASSCF calculation.	58
2.4	The real and the model molecular system in an ONIOM calculation in ethane. The LA, LAH and LAC are indicated.	63
2.5	The real and the model molecular system in two ONIOM calculation in propane, using the EE and ME schemes. The dots in the EE calculation represent the point charges included in the high-level Hamiltonian.	65

6.1	Course of MECI searches with DNR algorithms for azulene. Blue lines are pure DNR algorithm and red lines are the hybrid DNR-CS. In the top plot, the full lines are the energy of the GS and ES in fulvene in the optimization steps; hashed lines are the energy difference between the two states. In the second graph the χ angles between x_1 of the two consecutive steps are plotted.	120
6.2	Energies of ES and GS (full lines, left axis) and energy difference (dashed lines, right axis) in steps of the MECI optimization of acrolein (a) and benzene (b) with CG, CG-CS and DNR-CS algorithms. Energies are in hartrees	122
6.3	Course of MECI searches with CG, CG-CS and DNR-CS algorithms for tritret-butylfulvene. Full lines are the energy of the two states and hashed lines is the energy difference. Energies in hartree.	125
6.4	Course of MECI searches with CG-CS and DNR-CS algorithms for hexaphenylbutadiene. The structures are from DNR-CS and the red vectors are the forces each point. Full lines are the extrapolated and QM model energy in each step, and dashed is the energy difference. Energies in hartree.	126
6.5	Energy profile of GS and first ES of DPDBF inside its own crystal, with totally frozen crystal (a) and free first layer (b). Energies in hartree.	127
6.6	Energy profile along Q_{x1} at different non-resonant field intensities, including energy difference between the vertical excitation and the CI_{plan} . Dots are the <i>ab initio</i> energies of the <i>A</i> and <i>B</i> states. Dashed lines are the energies of the model. Q_{x1} displacements in mass-weighted atomic units, energies in eV.	132
6.7	S_1 population for the propagations with static electric field of different intensity.	133

6.8	Snapshots of the wave packet propagations on the V_2 surface along the Q_{x1} and φ coordinates, displaying the time and the population of V_2 . Propagations carried out (a) without non-resonant field and (b) with a static non-resonant field of -0.04a.u. Wave packet density is plotted in red and the seam position in black.	134
6.9	V_2 population for the propagations with dynamic non-resonant electric field of different intensity.	136

Contents

Summary of the thesis	1
Resum de la tesis	5
Resumen de la tesis	9
1 Introduction	13
1.1 Electronic Excited State	14
1.1.1 Radiationless relaxation	18
1.1.2 Conical intersections	20
1.2 Photochemical reactions	24
1.2.1 Cis/trans photoisomerisation	24
Rhodopsin	26
1.2.2 Fulvene	27
2 Theory and Methods	33
2.1 Schrödinger equation	33
2.2 Born-Oppenheimer approximation	35
2.2.1 PES	36
2.2.2 Diabatic and adiabatic picture	38
2.2.3 Geometry optimization	40
Newton-Raphson and Quasi-Newton-Raphson	41
Constrained Optimization	43
Coordinates	44

2.2.4	CI Optimization	46
	Intersection Space Hessian	51
2.3	Electronic methods	52
2.3.1	Solving TISE	53
	Hartree-Fock	55
	CASSCF	57
2.3.2	Molecular Mechanics	60
2.3.3	ONIOM	62
	Optimizations with microiterations	64
	EE and ME	65
	ONIOM in the Excited State	66
2.4	Photoexcited molecular dynamics	67
2.4.1	Solving the TDSE	68
	MCTDH	68
3	Objectives	71
4	New CI optimization algorithm: DNR	75
4.1	Conical Intersection Optimization Based on a Double Newton-Raphson Algorithm Using Composed Steps . .	75
4.2	Conical Intersection Optimization using Composed Steps inside the ONIOM scheme. QM:MM with mechanical embedding and microiterations.	87
5	Photophysics under Stark effect	99
6	Results and discussion	117
6.1	New CI optimization algorithm: DNR	117
6.1.1	MECI optimization algorithm inside ONIOM . .	123
6.2	Photophysics under Stark effect	128
6.2.1	Parametrization	130
6.2.2	Quantum dynamic simulations	132
	Propagations under static non-resonant fields .	133
	Propagations under dynamic non-resonant fields	135

7 Conclusions

137

Bibliography

139

Summary of the thesis

Photochemical processes are not unusual cases in chemistry. For example, there are several photo-processes crucial for life, such as the vision mechanism.^{18,19} However, they and ground state (GS) processes have substantial differences in their studies and applications at the theoretical level. On the one hand, apart from the typical critical points for analysing the Potential Energy Surface (PES) in GS, such as minima or Transition state (TS), the excited state (ES) PES study has Conical Intersections (CIs), structures of the system where the energy difference between two or more states is zero and, so, the PES are touching. The radiationless transition in these points has a particularly large interconversion rate between electronic states. However, CIs are not isolated points in PES, they form intersection seams that retained the the degeneration, a subspace inside the PES. Therefore, one way to analyse and study the seam is to find the minimum energy point, MECI. MECI is included in the set of critical points of ES PES studies. However, MECIs are not intuitive molecular structures. For this reason, optimization algorithms are necessary for finding them. There are several algorithms,⁴⁶⁻⁵⁰ divided in three groups according to their main ideas. The algorithms based on projected gradient have a good efficiency and are easy to implement. For this reason, the Composed Gradient (CG)⁴⁸ algorithm is the most used algorithm for finding MECI. However, CG has problems to retain the degeneracy when it is reached. For this reason, Sicilia and co-workers⁴⁹ proposed a new projected gradient algorithms, composed steps (CS), for improving the stability in the seam.

In this thesis, a new projected gradient algorithm that improves the approach to the seam has been proposed: Double Newton-Raphson (DNR). Its step is the sum of two Newton-Raphson optimizations to improve the approach to the seam and retain the degeneracy correctly. DNR and the other projected gradient algorithms, CG and CG-CS, have been implemented in the Gaussian program and tested with a set of eleven molecules. DNR obtains, in average, less optimizations steps and it reaches the seam earlier.

Clearly, finding the seam is fundamental in ES PES studies of photoprocesses. The ES PES is usually obtained with fully-quantum calculation. However, large systems, such as most of biological ones, are out of reach for *ab initio* calculations. In this large system, the ONIOM scheme⁵⁷⁻⁶² can obtain accurate results with low computational time. The ONIOM scheme combines two or more levels of calculation in the same system. The system is separated into two or more layers, where one is calculated with a high level calculation, known as the model system, and the rest with the cheaper one. Bearpark and co-workers adapted the CG algorithm in the ONIOM scheme.⁷²

In this thesis, all projected gradient algorithms have been implemented inside ME-ONIOM scheme. The implementation is done in the Gaussian program. The algorithms are tested with a systematic set of 18 molecules. However, in this case, the three algorithms obtain the same efficiency because DNR presents a problem in some ONIOM cases with bulky substituents. To show the potential of the MECI ONIOM algorithms, the MECI and minima of the ground and excited state of diphenyl dibenzofulvene (DPDBF)⁷³ inside its own crystal are calculated. DPDBF is an interesting molecule because it shows different relaxation behaviour in solution and in crystal. Calculations were done in two kind of environment: one where the crystal that surrounds the model is completely frozen, and other where a layer of eleven molecules that surround the model are free to move. The results show the expected relation between the MECI and the Frank-Condon point and, also, small differences between the models related with the sterical effects of the free layer.

Proposing new strategies is one of the main roles of the theoretic-

cal chemistry. Using previous studies of the PES, chemists can propose new strategies for new challenges, such as how to control photoprocesses. In recent years, the control was achieved using non-resonant electric fields because they shift the PES (Stark effect).^{74,75} The intense fields of electromagnetic radiation can obtain relevant effects in chemistry. Using these fields to control photoprocesses is known as non-resonant dynamic Stark effect (NRDSE) control. Photoprocesses of different diatomic molecules^{74,76-79} and polyatomic molecules^{80,81} have been controlled with NRDSE.

In this thesis, the control of fulvene ES lifetime with NRDSE has been simulated with quantum molecular dynamics with a two states and four-dimensional model. Fulvene is a cyclic hydrocarbon with an exocyclic double bond that can rotate in ES. However, the planar CI is the main deactivation pathway because the rotation modes need more time to be activated. The electric field shifts the energy of the planar CI, and it becomes non-energy-accessible with field intensities larger than 0.032 a.u.. The simulations with a static field show that the ES lifetime is increased to 40 fs with 0.04 a.u. of field intensity. The simulations with NRDSE control (where the field change with the time), with two lasers, one resonant and other non-resonant, show that the control is achieved when the field intensity is 0.08 a.u..

Resum de la tesis

Els processos fotoquímics no són casos inusuals en la química. Per exemple, hi ha diversos foto-processos crucials per la vida com el mecanisme de la visió.^{18,19} Tot i així, els foto-processos i els processos en l'estat fonamental (Ground State - GS) tenen algunes diferències en els seus estudis i aplicacions a nivell teòric. Per una banda, l'estudi de les corbes d'energia potencial (Potential Energy Surface - PES) del estat excitats (Excited State - ES) no només es centra en els típics punts crítics de les PES del GS si no que també s'estudia les interseccions còniques (Conical intersections - CI), estructures on la diferència entre les energies de dos o més estats és zero i, per tant, les PES es toquen. Les CI són casos particulars on les transicions sense radiació tenen un ràtio d'interconversió entre estats electrònics molt elevada. No obstant, les CI no són punts aïllats en les PES, grans interseccions multidimensionals on les PES es toques són formades, al llarg de les quals la degeneració de l'energia es manté. D'aquesta manera, una manera d'estudiar aquest espai és buscant el punt de mínima energia, MECI. No obstant, els MECI no són estructures intuïtives. Per aquesta raó, els algorismes d'optimització són necessaris per trobar-les. Hi ha diversos algorismes,⁴⁶⁻⁵⁰ dividits en tres grups segons la idea en el qual estan basats. Els algorismes basats en el gradient projectat tenen una bona eficiència i són fàcils d'implementar. Per aquest motiu, l'algoritme del gradient compost (CG)⁴⁸ és el més utilitzat per buscar el MECI. Tot i així, CG té problemes per mantenir la degeneració durant l'optimització. Per aquest motiu, Sicilia i col·laboradors van proposar un nou algoritme, composed steps(CS),⁴⁹ per tal de millorar

l'estabilitat.

En aquesta tesis, un nou algoritme basat en el gradient projectat ha sigut proposat per tal de millorar l'aproximació a l'intersecció: el Double Newton-Raphson (DNR). El pas del DNR és la suma de dos passos Newton-Raphson per tal de millorar l'aproximació a la degeneració i per mantenir-la correctament. DNR ha estat implementat en el programa Gaussian i ha estat testat amb un conjunt de MECI coneguts, juntament amb la resta de algoritmes basats en el gradient projectat, CG i CG-CS. DNR obté, de mitjana, menys passos d'optimització i arriba a la degeneració abans.

Clarament, trobar la intersecció es fonamental per l'estudi de la PES del ES. Les energies del estat excitat bàsicament s'obtenen amb càlculs purament quàntics. Tot i així, sistemes grans, com els biològics, estan fora del abast dels càlculs *ab initio*. Per sistemes grans, el esquema ONIOM⁵⁷⁻⁶² pot obtenir resultats prou acurats amb baixos costos computacionals. L'ONIOM combina dos o més nivells de calcul en un mateix sistema. El sistema es separat en dos o més parts, on una és calculada amb un mètode de calcul d'alt nivell, coneguda com a model, i la resta amb mètodes de calcul més barats. Bearpark i col·laboradors van adaptar el algoritme CG al esquema ONIOM.⁷²

En aquesta tesis, tots els algoritmes basats en el gradient projectat han sigut implementats en l'esquema ME-ONIOM, dins del programa Gaussian. Els algoritmes han estat provants amb un test format per 18 molècules. En aquest cas, els tres algoritmes donen mitjanes molt semblants perquè el DNR presenta un problema en alguns casos ONIOM amb substituents voluminosos. Per mostrar el potencial d'aquesta implementació dels algoritmes per buscar el MECI dins del ONIOM, els punts crítics del diphenyl dibenzoo-fulvene (DPDBF) són calculats dins del seu propi cristall. El DPDBF és un cas interessant perquè la molècula presenta un comportament diferent en forma de cristall que en solució.⁷³ Els càlculs s'han fet amb dos tipus diferents de entorn: un on el cristall esta completament congelat i un altre on una capa al voltant del model s'ha deixat lliure. Els resultats són els esperats amb relació el MECI i hi ha petites diferències entre els models d'entorn relacionades amb els efectes estèrics.

Proposar noves estratègies és un dels principals rols de la química teòrica. Utilitzant estudis previs de la PES, els químics poden proposar noves estratègies con ara controlar foto-processos. En els últims anys, s'ha aconseguit controlar sistemes utilitzant camps electrònics no ressonants, que modifiquen la PES (efecte Stark).^{74,75} La intensitat de la radiació electromagnètica pot obtenir efectes a nivell químic. Utilitzar el camp elèctric de la radiació pel control és conegut com control non-resonant dynamic Stark effect (NRDSE). Foto-processos de diferents molècules diatòmiques^{74,76-79} i poliatòmiques^{80,81} han estat controlats amb NRDSE.

En aquesta tesis, un control del temps de vida del ES del fulvè ha sigut simulat amb dinàmiques a nivell quàntic, on un model de dos estats i quatre dimensions ha estat usat. El fulvè és un hidrocarbur cíclic amb un enllaç doble exterior al cicle que pot rotar en el ES. Tot i així, el camí de desactivació principal del ES és a través de la CI plana perquè la rotació necessita un temps per ser activada. El camp elèctric pot desplaçar l'energia de CI plana i fer-la inaccessible pel sistema, en intensitats superiors a 0,032 a.u. Les simulacions amb camps estàtics mostren com el temps de vida del estat excitat augmenta dels 10 fs als 40 fs. El control amb NRDSE (camp dinàmic), produït amb dos làsers, on un és ressonant i l'altre és no ressonant, mostra que el control pot ser aconseguit amb camps d'intensitat 0,08 a.u..

Resumen de la tesis

Los procesos fotoquímicos no son casos inusuales en la química. Por ejemplo, hay diversos foto-procesos cruciales por la vida como el mecanismo de la visión. Aún así, los foto-procesos y los procesos en los estado fundamental (Ground State - GS) tienen algunas diferencias en los sus estudios y aplicaciones a nivel teórico. Por un lado, las superficies de energía potencial (Potential Energy Surface - PES) del estado excitado (Excited State - ES) no sólo tiene los típicos puntos críticos de las PES del GS si no que también tiene las intersecciones cónicas (Conical Intersections - CI), estructuras donde la diferencia energía entre dos o más estados electrónicos es cero y sus PES se tocan. Las CI son casos particulares de transiciones sin radiación: tienen un alta tasa de interconversión entre estados electrónicos. No obstante, las CI no son puntos aislados en las PES, grandes intersecciones multidimensionales donde las PES se tocan son formadas, al largo de las cuales la degeneración de la energía se mantiene. De este modo, una manera de estudiar este espacio es buscando el punto de mínima energía, MECI. No obstante, los MECI no son estructuras intuitivas. Por esta razón, algoritmos de optimización son necesarios para encontrarlas. Hay varios algoritmos, divididos en 3 grupos según la idea en la cual están basados. Los algoritmos basados en el gradiente proyectado tienen una buena eficiencia y son fáciles de implementar. Por este motivo, el algoritmo del gradiente compuesto (CG) es el más utilizado para buscar el MECI. Aún así, CG tiene problemas para mantener la degeneración durante la optimización. Por este motivo, Fabrizio y colaboradores propusieron un nuevo algoritmo, Composed Steps(CS),

por tal de mejorar la estabilidad.

En esta tesis, un nuevo algoritmo basado en el gradiente proyectado ha sido planteado para mejorar la aproximación a la intersección: el Double Newton-Raphson (DNR). El paso del DNR es la suma de dos pasos Newton-Raphson para mejorar la aproximación a la degeneración y para mantenerla correctamente. DNR ha sido implementado en el programa Gaussian y ha sido testado con un conjunto de MECI conocidos, junto con el resto de algoritmos basados en el gradiente proyectado, CG y CG-CS. DNR obtiene las mejores medias en el número de ciclos de optimización y también llega a la degeneración antes y con una mejor energía.

Claramente, encontrar la intersección es fundamental para el estudio de la PES del ES. Las energías del estado excitado básicamente se obtienen con cálculos puramente cuánticos. Aún así, sistemas grandes, como los biológicos, están fuera del alcance de los cálculos *ab initio*. Para sistemas grandes, el esquema ONIOM puede obtener resultados bastante precisos con bajos costes computacionales. El ONIOM combina dos o más niveles de calculo en un mismo sistema. El sistema es separado en dos o más partes, donde una es calculada con un método de calculo de alto nivel, conocida como modelo, y el resto con métodos de calculo más baratos. Bearpark y colaboradores adaptaron el algoritmo CG al esquema ONIOM.

En esta tesis, todos los algoritmos basados en el gradiente proyectado han sido implementados en el esquema ME-ONIOM, dentro del programa Gaussian. Los algoritmos son probados con un test formado por 18 moléculas. En este caso, los tres algoritmos dan medias muy parecidas porque el DNR presenta un problema en algunos casos ONIOM con sustituyentes voluminosos. Para mostrar el potencial de esta implementación de algoritmos para buscar el MECI dentro del esquema ONIOM, los puntos críticos del diphenyl dibenzoo-fulvene (DPDBF) son calculados dentro de su propio cristal. El DPDBF es un caso interesante porque la molécula presenta un comportamiento diferente en solido que en solución. Los cálculos se han hecho con dos tipos diferentes de sistema: uno donde el cristal esta completamente congelado y otro donde una capa alrededor del modelo se ha dejado libre.

Los resultados son los esperados con relación al MECI y hay pequeñas diferencias entre los modelos relacionadas con los efectos estèricos.

Proponer nuevas estrategias es uno de los principales roles de la química teórica. Utilizando estudios de la PES, los químicos pueden proponer nuevas estrategias como controlar foto-procesos. En los últimos años, se ha conseguido controlar sistemas utilizando campos electrónicos no resonantes, que modifican la PES (efecto Stark). La intensidad de la radiación electromagnética puede obtener efectos a nivel químico. Usar el campo eléctrico de la radiación para controlar es conocido como control non-resonant dynamic Stark effect (NRDSE). Foto-procesos de diferentes moléculas diatómicas y poliatómicas ha sido controlada con NRDSE.

En esta tesis, un control de la foto-rotación del fulveno ha sido simulado con dinámicas a nivel cuántico, donde un modelo de dos estados y cuatro dimensiones ha sido usado. El fulveno es un hidrocarburo cíclico con un enlace doble externo al ciclo que puede rotar en el ES. Aún así, el principal camino de la desactivación del ES es a traves de la CI plana porque la rotación necesita un tiempo para ser activada. El campo eléctrico puede desplazar la CI plana y hacerla inaccesible por el sistema, en intensidades de campo más grandes de 0,032 a.u.. Las simulaciones con campos estáticos muestran como el tiempo de vida del estado excitado aumenta de los 10 fs a los 40 fs. El control con NRDSE (campo dinámico), producido con dos láseres, donde uno es resonante y otro no resonante, muestra que el control puede ser conseguido con campos de intensidad 0,08 a.u..

Chapter 1

Introduction

Movement is the basis of chemistry: electrons and nuclei induce reactions. Even when molecules are in the stationary state, according to quantum mechanics, atoms and molecules move: orbitals describe electrons movements, nuclei vibrate according to their vibrational states and molecules rotate in accordance with stationary states. But the movement is emphasised outside the stationary states, and the absorption of electromagnetic radiation by resonant photons often causes disruption of the stationary states. This phenomenon is very important since it can explain, among others, the colours of the materials. Quantum mechanics describes how energy is quantised and can only constitute discrete values. In chemistry, this fact means that molecules and atoms have different states each with a discrete and unique energy. Usually, the ground state (GS), the state with least energy, is the most studied in theoretical calculations because most molecules remain in the GS. However, there are infinite excited states (ES) with more energy where the molecules have absorbed one photon. Such states are very important in chemistry and physics when the radiation is involved.

Notwithstanding, the excited state is not essential for describing all reactions. Thermal reactions and chemical equilibriums can be described by quantum calculations in ground state and stationary states. Yet many reactions and processes need a correct description of the excited

state and its dynamics, such as the case that this thesis describes: the photorotation of fulvene.

1.1 Electronic Excited State

At the end of the nineteenth century, physics had a serious problem: explaining the spectra of absorption and emission of atoms. Nowadays, however, we know that atom state energies are discrete and their spectrum are formed by the transitions between atomic electronic states. For this reason, atomic spectra are isolated lines because the energy of the photons has to be exactly equal to the energy difference between the two states involved in the emission and absorption. The emission spectra give the energy of the photons which the excited atoms emits. The absorption spectra are produced by the photons that atoms do not absorb. However, not all transitions between states are permitted. The ratio of the electronic transitions is adjusted by the oscilla-

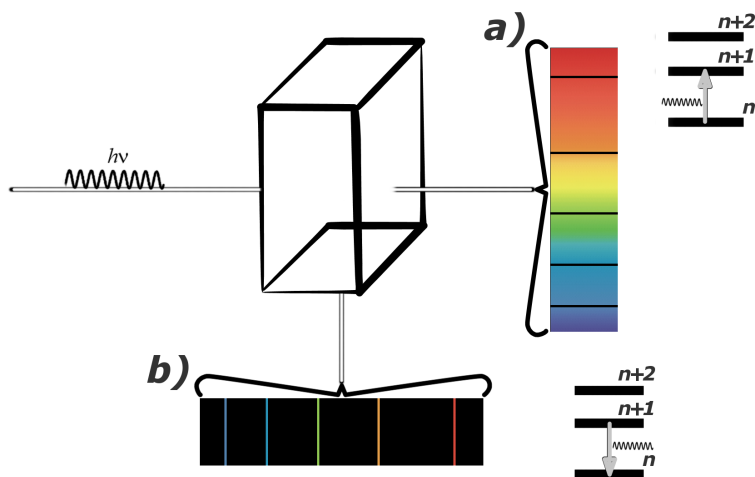


Figure 1.1: Scheme of absorption (a) and emission (b) in atoms. Each line is a transition to a low state in emission or a high state in absorption.

tor strength ($f_{i,j}$) between the two states. Usually, this dimensionless quantity is calculated with the dipole length formula:^{1,2}

$$f_{i,j} = \frac{2}{3} \Delta\varepsilon |TDM_{i,j}|^2 \quad (1.1)$$

$$TDM_{i,j} = \langle \Psi_i | \vec{\mu} | \Psi_j \rangle = \sum_{k=1}^N \langle \Psi_i | \vec{k}_i | \Psi_j \rangle \quad (1.2)$$

where $\Delta\varepsilon$ is the energy difference between the two states, $TDM_{i,j}$ is the transition dipole moment between the two states and the second equality of 1.2 is valid in atomic units (a.u.). Ψ is the wave function of each system state (see chapter 2) and \vec{r} is the operator giving the position of the electron. Oscillator strength is a dimensionless term that ranges from zero to one, where zero is a forbidden transition and one is a totally allowed one. In this approximation, states with different spin have a forbidden transition because TDM is zero (the \vec{r} operator does not have any spin term and the integral of two wave functions with different spin is zero). However, the dipole length formula for the oscillator strength (Equation 1.1) is only an approximation, where some terms are neglected.² Thus, the transition between two states is possible although TDM is zero. However, the transition ratio in these cases is close to zero because the main term should be the TDM .

On the other hand, the molecular spectra have some differences with respect to atomic ones. Molecules are formed by two or more atoms with their correspondent nuclei. Other contributions to the energy, apart from electronics, are due to the nuclei movement, such as vibrational and rotational. However, unlike electrons, nuclei can normally be distinguished and their movement is slower than that of the electrons. Therefore, one can approximate that the nuclei and the electrons move independently (Born-Oppenheimer approximation,³ section 2.2) and so the energies of the molecular states are the sum of the electronic and nuclear state energies. Thus, the molecular transitions can be read as the sum of electronic and nuclear transitions. Since nuclear transitions are less energetic than electronic ones and they differ by some order of magnitude, electronic transitions can be associated

with different nuclear ones (vibrational and rotational). Thus, generally, electronic spectra contain an accumulation of different isolated transitions, combination of the same electronic transition with a large number of nuclear ones. In fact, if the spectrum does not have enough resolution, transitions show broad instead of the typical isolated lines of quantum mechanics.

The interpretation of molecular spectra is different from that of atomic ones. Whereas atoms have complementary discrete spectra with electronic emission and absorption, as shown in figure 1.1, molecular systems have combinations of nuclear and electronic transitions. On the one hand, unlike atomic spectra, the molecular spectra are not complementary, and there is a shift between absorption and emission, the *Stokes' shift* (Figure 1.2). On the other hand, the spectral maxima almost always does not correspond to the energy difference between the minimum of the energy between the two states. In that context, quantum chemistry can provide insight to explain the phenomenon using the B-O approximation (see section 2.2). Inside the B-O approximation, the potential energy of the system is calculated in a particular position of the nuclei. Since it can be calculated for any

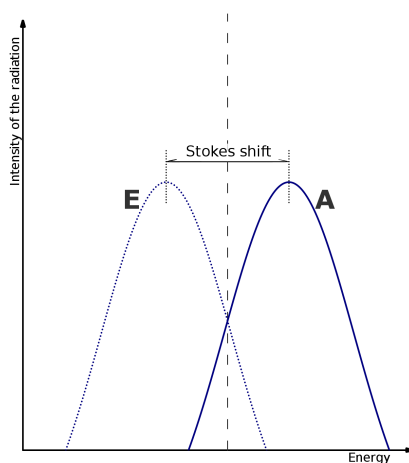


Figure 1.2: Scheme of *Stokes' shift* between molecular absorption (A) and emission (E) spectra.

nuclear geometry, the potential energy can be described as a function of the nuclear position, known as the Potential Energy Surface (PES) (see section 2.2.1). Each PES is associated to a different electronic state, and defines the nuclear motion in this state. Thus, the PES is an excellent tool for understanding the molecular phenomena, such as those previously described, along with certain rules and principles. The Frank-Condon principle^{4,5} describes the absorption and emission of the molecules as vertical transitions from the minimum of the original state: the so-called vertical approximation. Electrons move quicker than the nucleus so the nuclear coordinates are considered fixed during the electronic transition. Thus, the transition can be considered vertical between PES of two electronic states. Following equation 1.2, the simple overlap of nuclear wave function increases the oscillator strength because the electronic transition dipole moment operator only depends on the electronic wave function. Therefore, vertical transitions generally start near the minimum of the lowest state since the nuclear wave functions are normally centred there. Kasha's rule says the emissions occur in appreciable yield only from the lowest potential energy point of the lowest excited state of a given multiplicity. The emission process needs some picoseconds or more to start with significant yield but the nuclear vibrations only take a few femtoseconds. With that scale difference, the nuclear motion can find the minimum in the excited PES and the emission occurs near the minimum. The Frank-Condon principle can explain why the maxima in spectra do not correspond to the 0-0 energy (the energy difference between the minimum of the two states) and Kasha's rule explains the shift between absorption and emission. A combination of the two rules is shown in Figure 1.3.

There are different nomenclatures for excited states, but two are the most commonly used. On the one hand, there is Kasha's nomenclature. The states can be represented as Slater determinants formed with different orbitals, the excited states being named with the orbitals changed between the ground state and the excited state. Thus, in this nomenclature, the excitation and the excited state are expressed as $\pi \rightarrow n$, where π is the original orbital in the GS Slater determinant

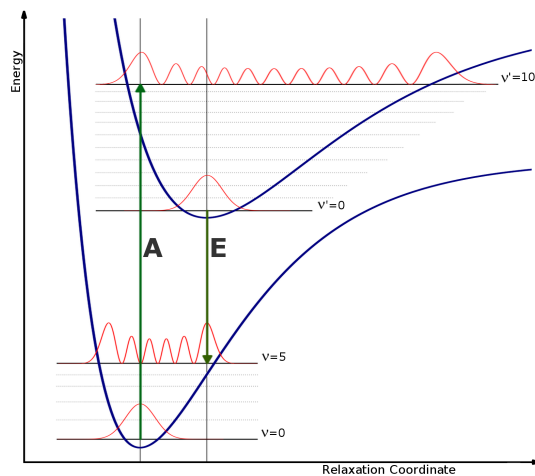


Figure 1.3: Scheme of Frank-Condon principle and Kasha's rule between two PES of two electronic states with their associated vibronic states. The arrows correspond to absorption (A) and emission (E) processes.

and n is the orbital of the ES determinant. Although the Slater determinant is a simple approximation for the systems and a pair of orbitals cannot fully describe the excited state, this nomenclature is useful for simple or organic molecules. On the other hand, the most common and general notation is the enumerative one, where the states are named according to their energetic order and their multiplicity. The adiabatic state with lowest energy is defined as zero. If the state is a singlet, it is denoted by S_0 , and the excited states S_1, S_2, S_3, \dots . The excited triplet states have a similar formula: T_1, T_2, T_3, \dots . Diabatic states are usually numbered from one.

1.1.1 Radiationless relaxation

Atoms and molecules can radiate energy through photon emission. Yet there is another relaxation process in molecules: non-radiative relaxation. This is the phenomenon whereby a molecular system changes the state without any emission or absorption. Inside the Born-Oppenheimer approximation (see section 2.2), radiationless processes

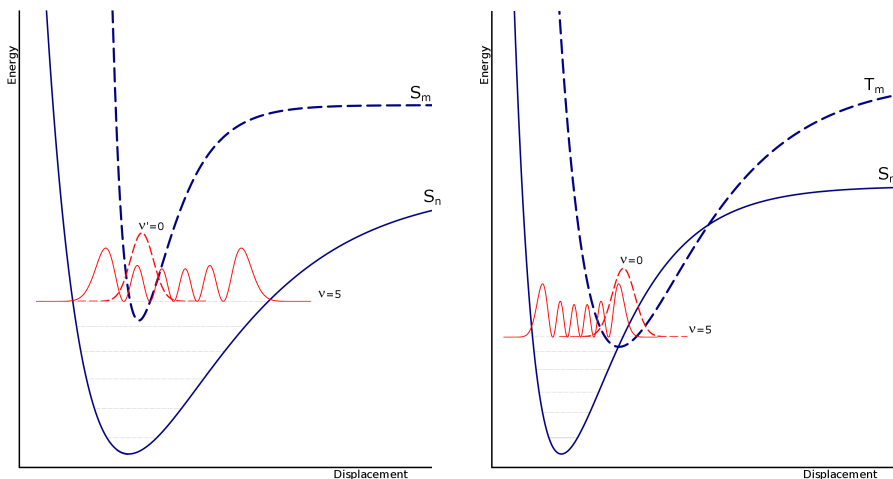


Figure 1.4: Two examples of radiationless relaxation of two singlets (a) and singlet and excited triplet state (b).

cannot be contemplated. It is necessary to go beyond the approximation and include the interaction between electronic states and nuclear motion. Using the time-dependent perturbation theory, the rate constant for interconversion between two states can be calculated and Fermi's golden rule^{6,7} is obtained:

$$k_{i \rightarrow j} = \frac{2\pi}{\hbar} \langle \Psi_i | \hat{H}' | \Psi_j \rangle^2 \delta(\varepsilon_i - \varepsilon_j) \quad (1.3)$$

where Ψ and ε are the wavefunction and the energy of i and j molecular states and \hat{H}' is the time-dependent perturbation operator. In states with equal spin, for example $S_n \rightarrow S_m$ or $T_n \rightarrow T_m$, the main contribution of the perturbation operator is the kinetic energy of the nuclei. In transition between states with different spin, such as $T_n \rightarrow S_m$, the main contribution is the spin-orbit coupling. In case of weak coupling, the expectation value of the perturbation operator follows the next relation:

$$\langle \Psi_i | \hat{H}' | \Psi_j \rangle \sim \beta^{IC} \langle \psi_i | \psi_j \rangle \quad (1.4)$$

where β^{IC} is the electronic part and $\langle \psi_i | \psi_j \rangle$ is the overlap of the nuclear part of the wave function. On the other hand, $\delta(\varepsilon_i - \varepsilon_j)$ is a Dirac delta function between the energy of the two states. This term is strictly zero in all cases except when the energy difference is zero. However, a smooth change is introduced by broadening effects in higher order perturbations theory, so the rate constant for interconversion is larger when the energies are the same and it decreases quickly for larger differences. The total rate constant is the sum of all possible transitions, so if the energy difference between the states is constant, it increases if there are more energy-accessible vibrational states.

$$k_i^{IC} = \sum_j k_{i \rightarrow j} \quad (1.5)$$

For example, when the energy difference between the electronic states increases, the density of vibrational states is increased in the low energy electronic state and the interconversion from higher energy electronic states to lower ones is more effective than in the other direction.

1.1.2 Conical intersections

The Conical Intersection (CI) is a particular geometrical structure of molecules where there is electronic energy degeneracy: two or more electronic states have the same energy. In these points, the non-radiative transition has a specially large rate. Using Fermi's golden rule (equation 1.3) to calculate the rate, it is easy to see why the rate is really high: at the CI, the delta is clearly one and the overlap of the nuclear wave function (equation 1.4) has a higher value than in other geometries because the vibrational states have the main density at the sides of the potential. However, the first order perturbation theory is not enough to correctly determine the transition rate at the CI because the other perturbation terms have significant value. Therefore, the rate is very high between the two states (or more) at the CI so the interconversion is very favourable in the CI geometry. At such high rate, the interconversion only takes some femtoseconds, whereas the radiative processes need picoseconds or more. So, based on Kasha's

rule, if the CI geometry is energy-accessible to the nuclear motion, after an absorption, the interconversion is the main way to deactivate the ES and an emission does not appear. This phenomenon is called ultrarapid decay and it is the principal experimental evidence of CI's important role in photochemistry and excited state processes. The importance of CI in photochemistry has been known for a long time.⁸ Since the late 1990s, CI have gained importance in studies of excited state. Nevertheless, for a long time it was believed that truly touching PES are very rare because in diatomic molecules crossings only occur when the two states have different symmetry. In the 1990's, however, with the increase of computational power, a lot of CI between states of the same symmetry were found in many polyatomic molecules. Nowadays, lots of photoreactions are understood with CI concept and all studies of excited state include CI analysis, where a very important point is the minimum CI, the Minimum Energy CI (MECI). The MECI is the principal point where the transition is brought about. For this reason, algorithms for finding CI and MECI (section 2.2.4) have been developed.

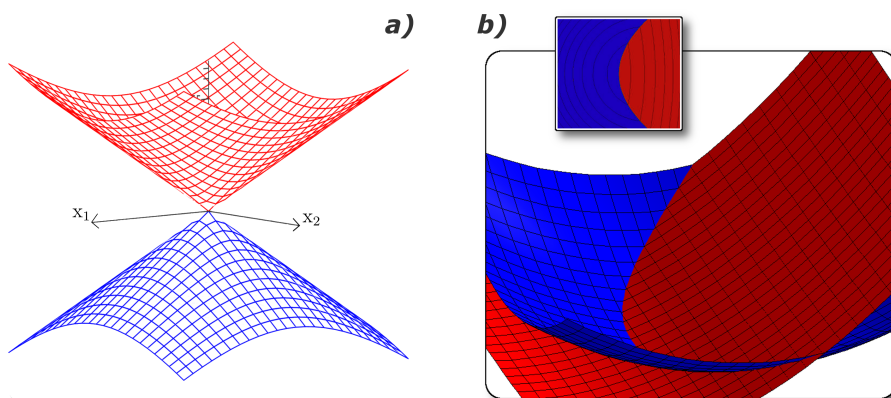


Figure 1.5: a) Typical form of a conical intersection plotted in the direction of the BS. b) Example of seam plotted in one direction of the BS and the other direction with large second order components.

One can characterize a CI point on a PES by two conditions:

$$\varepsilon(q)_I - \varepsilon(q)_J = 0 \quad \langle \varphi(r; q)_I | \hat{\mathbf{H}} | \varphi(r; q)_J \rangle = 0 \quad (1.6)$$

where I and J are the two degenerate electronic states and ε_I and φ_I are the electronic energy and electronic wavefunction of the state I , respectively, in the CI nuclear geometry (q). Every geometrical structure of the molecular system which fulfils these two conditions is a CI. Evidently, they are not isolated geometries in the PES of polyatomic molecules, there is a hypersurface where the degeneracy between two (or more) states is retained. This hypersurface, or seam, is called the intersection space, where the degeneracy remains. In polyatomic molecules and between two states, the seam is $n-2$ dimensional, where n is the number of coordinates of the molecular system. This space is defined as the orthogonal space to the branching space which is formed by the modes, or vectors in the PES, which break the degeneracy. In first order, there are two directions that break the degeneracy: gradient difference (\mathbf{x}_1) and interstate coupling (\mathbf{x}_2), the gradient of the two CI conditions.

$$\mathbf{x}_1 = \nabla (\varepsilon(q)_I - \varepsilon(q)_J) \quad \mathbf{x}_2 = \nabla \left(\langle \varphi(r; q)_I | \hat{\mathbf{H}} | \varphi(r; q)_J \rangle \right) \quad (1.7)$$

Normally, the first-order BS vectors are the most important ones in terms of breaking the degeneracy so the representations of the energy of the two states in these two directions form a cone which gives the name to CI (Figure 1.5.a). For this reason, these vectors are fundamental to find the CI and the MECI. However, if the two states have different spin and there are not any spin-orbit terms in the Hamiltonian, the \mathbf{x}_2 is zero in the same way as oscillator strength (Equation 1.2).

The second-order directions normally do not have the same importance as the first-order ones. They are defined by the second-order matrix of the CI conditions:

$$\Delta \mathbb{H} = \nabla_{\mathbf{x}_1} = \nabla^2 (\varepsilon(q)_I - \varepsilon(q)_J) \quad \mathbb{E} = \nabla_{\mathbf{x}_2} = \nabla^2 \left(\langle \varphi(r; q)_I | \hat{\mathbf{H}} | \varphi(r; q)_J \rangle \right) \quad (1.8)$$

The eigenvectors of this matrix mark the directions where the degeneracy is broken in second order and the eigenvalues mark the scale of this change. The second order degeneracy-lifting effects can appear along all molecular modes, but in practice only some of these eigenvalues have a non-zero value so just some vectors can break the degeneracy in second order. In fact, the non-zero eigenvalues are normally small too, but, they give the second-order terms of seam and its shape so they are essential for determining the form of the seam.⁹ More information about the second order terms of the CI is provided in the Section 2.2.4.

The result of the non-radiative relaxation depends on the CI shape, which has two forms: sloped and peaked (figure 1.6). In sloped CI (a), the gradients of the two PES are similar (and have the same sign) at the intersection. In contrast, the peaked CI (b) has two PES with different signs at their gradients. The relaxation processes after the interconversion process of the two kinds of CI are totally different. A sloped CI usually has relaxations whereby the molecular system returns to the minimum of the ground state, the initial condition before absorption. In a peaked CI, however, the system can move in two different ways from ES: the initial minimum or another photo product. Thus, the shape of the CI plays a very important role in the nuclear

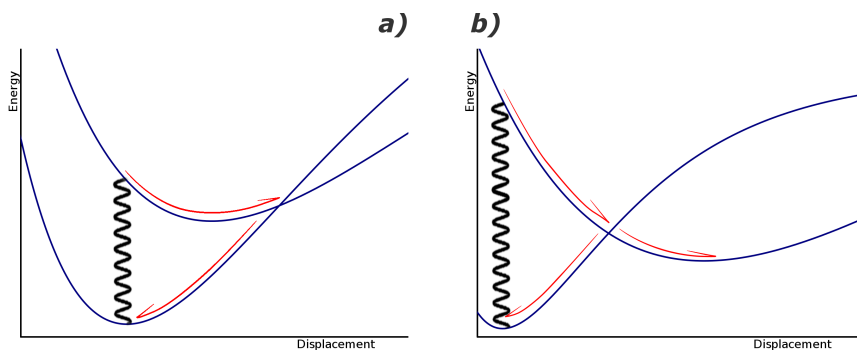


Figure 1.6: The two kinds of CI, sloped (a) and peaked (b), with the typical trajectories (shown with red arrows): in the sloped CI, the trajectories go to the GS minimum and, in the peaked CI, a photoproduct is accessible.

motion after excitation in the non-stationary process. Furthermore, the shape is not the same in all seams: the second-order terms change the gradients and the shape along the seam. Therefore, the point where the seam is reached is important in the study of the process.

1.2 Photochemical reactions

Photochemical reactions have several differences from typical ground-state reactions, which take place between different stationary points on a single PES. In photoreactions, at least two PES have a role in the process, but may be more. CI have a fundamental role in these reactions because they can mark the way of the reaction with their large rate of interconversion, as a funnels between the states. Furthermore, the photo-processes take place in a non-stationary scenario and this fact is important for the behaviour of the reaction.

There are a lot of photoreactions but there is one important and typical example in organic chemistry: cis/trans rotation.

1.2.1 Cis/trans photoisomerisation

In the ground state, the bond between two carbon (or nitrogen) atoms in sp^2 hybridization has a considerable energy barrier to rotation, so it is usually assumed it does not have free rotation as typical sp^3 bonds do. This is not necessarily true in the ES, where the double bonds are weaker than in the GS and rotation is permitted. This occurs because the excitation involves transition from a bonding to an anti-bonding π orbital. In fact, the electronic repulsion in first electronic excited states can force rotation of the bond. Thus, the electronic excitation of some organic molecules with double bonds can be used to isomerise the double bonds.

The cis/trans isomerisation can be discussed using ethylene (figure 1.7.a) as an example because it is the simplest C-C double bond molecule. Since ethylene is a very simple molecule, much has been written about its photophysics.¹⁰⁻¹⁵ Ethylene has T_1 and S_1 excited

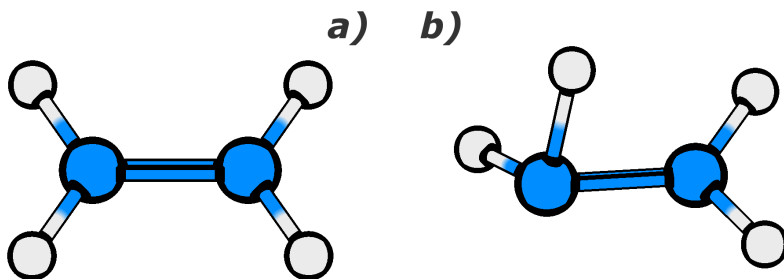


Figure 1.7: a) Molecular structure of ethylene in the minimum potential energy point of S_0 . b) Molecular structure of the MECI between the S_1 - S_0 states of the ethylene.

states close in energy that prompt the molecule to rotate. Both states can be described as $\pi \rightarrow \pi^*$ and the potential energy follows the same pattern (figure 1.8) in the rotation with a minimum at 90° in contrast to the ground state (S_0) where the minimum is 0° , facilitating the rotation in these two excited states. The energy needed to excite the molecule from S_0 to T_1 is lower than to go to S_1 but the transition to triplet from ground state is forbidden because there is a spin difference between the states. On the other hand, the $S_0 \rightarrow S_1$ transition is permitted but its energy transition is relatively high in ethylene or monoolefins. After the radiation is absorbed, ethylene enters in a nuclear non-stationary state on S_1 , with excess vibrational energy. The π^* orbital induces a strong repulsion in the system between the two carbons and, for this reason, the rotation is favourable, as figure 1.8 shows, where there is a local minimum in S_1 . Therefore, the rotation is favourable. However, ethylene deactivation is a non-radiative process and figure 1.8 does not show any CI for reaching the seam between S_1 - S_0 . Because the seams are a multidimensional space where not only one dimension is important, it is necessary to activate more modes to reach the seam. In ethylene's case, the pyramidalisation coordinate is important for describing the ES because a large change in dipole moment results along this coordinate and has a big effect on energy difference between S_1 and S_0 . Thus, the pyramidalisation coordinate is required to reach the seam. The MECI structure (figure

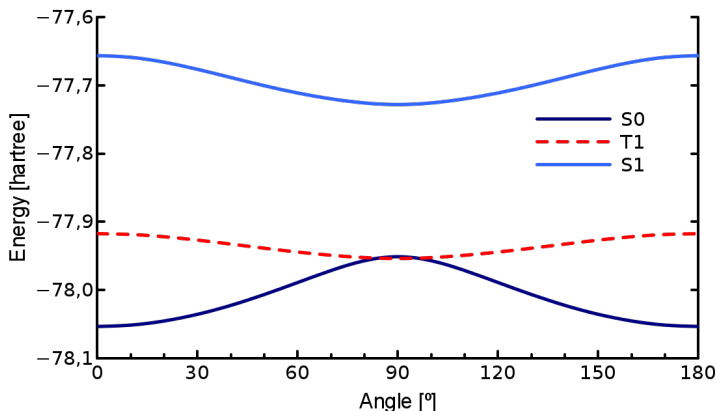


Figure 1.8: Potential energy plot of three states, S_0 , T_1 and S_1 , of ethylene along the rotation of the double bond with all other coordinates fixed. The energies correspond to CAS(2,2) calculations.

1.7.b) therefore, has extensive pyramidalisation but is also relatively near to the total orthogonal geometry (90° of rotation), so the rotation is favourable in the radiationless deactivation process.

Rhodopsin

The cis/trans photo-reaction of protonated Schiff base of retinal chromophore inside the rhodopsin protein is a typical example of that kind of reaction. It has a big relevance in life: this photorotation is the basis of the vision mechanism of a lot of animals, including humans. As shown in figure 1.9, the molecule has several double bounds and a central one is in cis conformation. After the absorption, during the decay route, the retinal rotates the cis double bond to obtain the all-trans conformation. The environment of rhodopsin protein is changed by the cis/trans photo-rotation and the protein is activated. This fact was identified as the primary photo-chemical event in vision.¹⁷ The photorotation has high efficiency: in less than 1 ps the rotation quantum yield is bigger than 50%.

There are many different studies, theoretical¹⁸ and experimental,¹⁹ in which the photoisomerisation path is studied. As with ethylene,

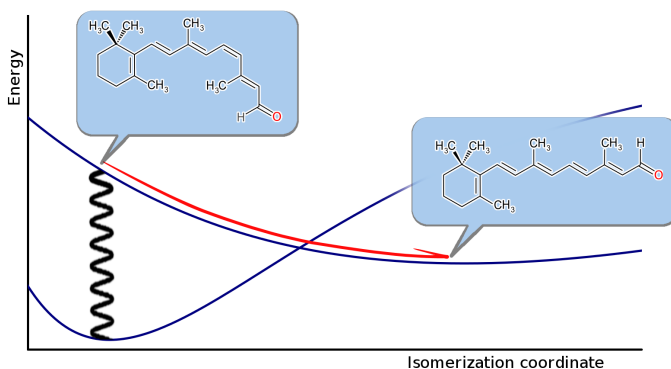


Figure 1.9: Energy scheme of retinal cis/trans isomerisation inside rhodopsin. The structures were adapted from Wikipedia.org¹⁶ and the retinal moiety of the PSB is displayed.

the photo-reaction is a non-radiative relaxation. The main relaxation modes are the rotation and a C-C stretching vibration and the relaxation minimum-energy path is barrier-less, crossing the seam at the 70° structure. The seam lies along the rotation coordinate but from 70° to 90° CIs are energy-accessible. After crossing the seam, the molecule decays to the trans minimum following the same rotation mode. The role of the CI is fundamental in this reaction because the GS is reached in just a few vibrational periods, allowing for a high efficiency.

1.2.2 Fulvene

A major part of this thesis is dedicated to theory and methodology but the last chapter of results is about the computational dynamic simulations of fulvene. Fulvene is a cyclic molecule isomer of benzene. Instead of the six-member ring of benzene, however, fulvene has a five-member ring with two double bonds and one double bond outside of the ring (figure 1.10), the only double bond which can rotate. Fulvene, like lots of non-fluorescent hydrocarbons, has a very rich photophysics. Its photophysics has been studied extensively, both experimentally^{20–22} and theoretically.^{23–27} Experimentally, fulvene presents

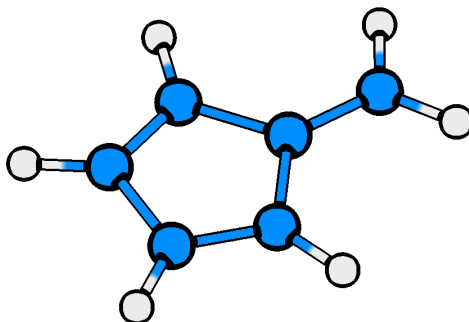


Figure 1.10: Molecular structure of fulvene in the minimum potential energy point of S_0 .

two strong bands in the absorption spectrum associated with excitation from the ground state (S_0) to the S_4 and S_3 states. At lower energies and intensities, two other dipole-allowed transition appear, corresponding to S_1 and S_2 . The $S_0 \rightarrow S_1$ transition has a weak and diffuse band, with a maximum at 3.44eV and low oscillator strength ($f = 0.008$). The absence of fluorescence suggests the presence of a seam between the two states which enables the fast decay. Theoretically, Bearpark and co-workers²⁵ confirmed the existence of the seam with *ab-initio* theoretical calculations. In the same study, the photorotation of fulvene was assessed with dynamic simulations starting from the S_1 minimum structure, showing it is possible in the excited state. Recently, other dynamic simulations²⁶ show the main decay route of fulvene and confirm the photorotation decay route depending on the conditions.

Theoretically, the PES study of the different states is the initial step to understand the photo-processes. However, since fulvene is a polyatomic molecule, obtaining its complete PES is an extremely hard challenge. Fortunately, the study of some modes is enough to understand its photophysics and its ES. Recently, the principal modes of fulvene PES were described²⁷ by means of computational calculations. Up to four modes are necessary to describe correctly the non-radiative relaxation: a totally symmetric bond alternating mode (Q_{x1}), a non-

totally symmetric bond stretch coordinate (Q_{x2}), rotation (φ) and pyramidalisation (θ). The modes can be seen in Figure 1.11. Unlike ethylene, fulvene can reach the seam along the stretch of the double bond. In fact, the main decay mode of fulvene is Q_{x1} , which includes the stretch of the double bond. In this mode, the planarity is conserved: the decay goes from the Frank-Condon point to the minimum of the S_1 and, further than $(S_1)_{min}$, to the CI_{plan} , as shown in figure 1.12.

Like in ethylene, rotation and pyramidalisation processes are important. The exocyclic CH_2 rotation follows a similar pattern as ethylene, where in S_0 the rotation has a maximum in the 90° whereas S_1 has a minimum (figure 1.13).

Following the seam along the CH_2 rotation coordinate from CI_{plan} , there is a CI with a perpendicular structure (CI_{perp}), with a lower energy than CI_{plan} . However, between CI_{plan} and CI_{perp} , at a torsion angle 63° , there is a minimum in the seam along the CH_2 rotation (figure 1.14). The global MECI is extremely close to CI_{63} : the energy

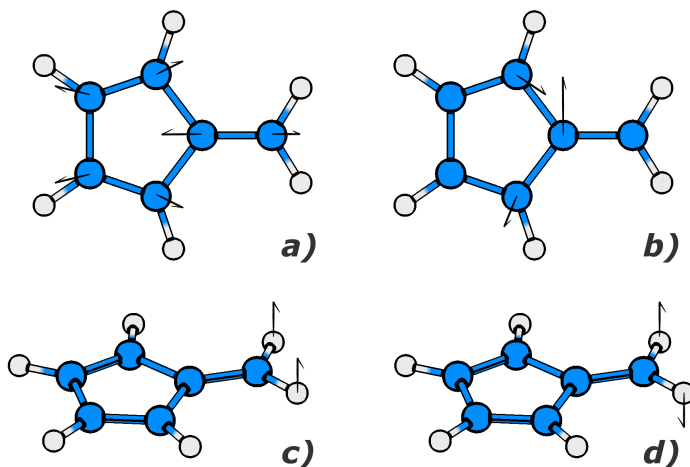


Figure 1.11: Principal modes of fulvene: the totally symmetric bond alternating mode (a), the non-totally symmetric bond stretch coordinate (b), pyramidalisation (c) and rotation (d).

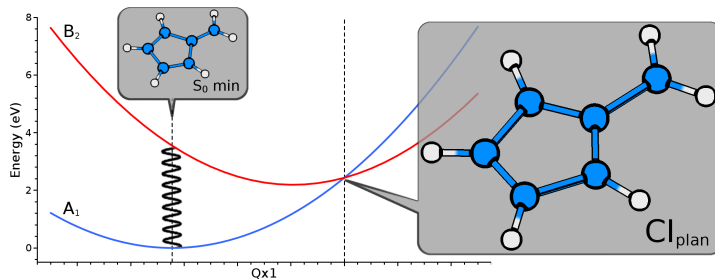


Figure 1.12: Energy plot along the totally symmetric bond alternating mode in 0° rotation angle and molecular structures of the CI between S_1 - S_0 and $(S_0)_{min}$ and the S_0 of fulvene

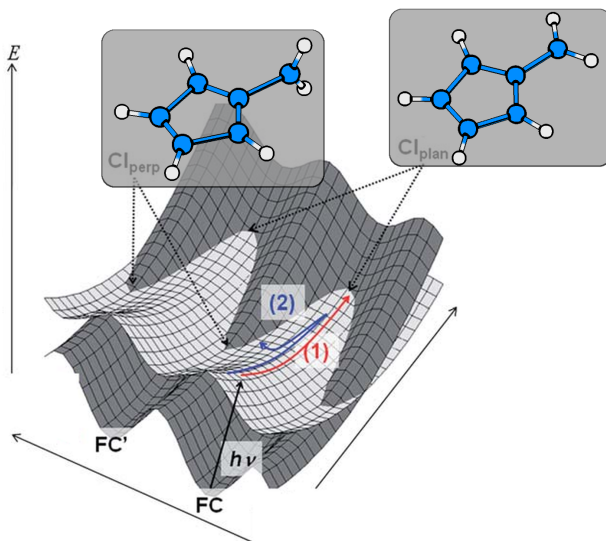


Figure 1.13: 3D energy plot of the S_1 and S_0 states of fulvene along the totally symmetric bond alternating mode and CH_2 rotation coordinate with molecular structure of the CI between S_1 - S_0 at $\varphi = 0^\circ$ and $\varphi = 90^\circ$.

difference between the two points is less than 1 meV, so it is a very good approximation to the MECI. This minimum is an important point of the relaxation path of the non-radiative rotation process. However, recent dynamics simulations²⁷ showed that CI_{plan} is the centre of the major part of the decay because the rotation coordinate needs some time to be activated. Thus, the cis/trans photoisomerisation has a

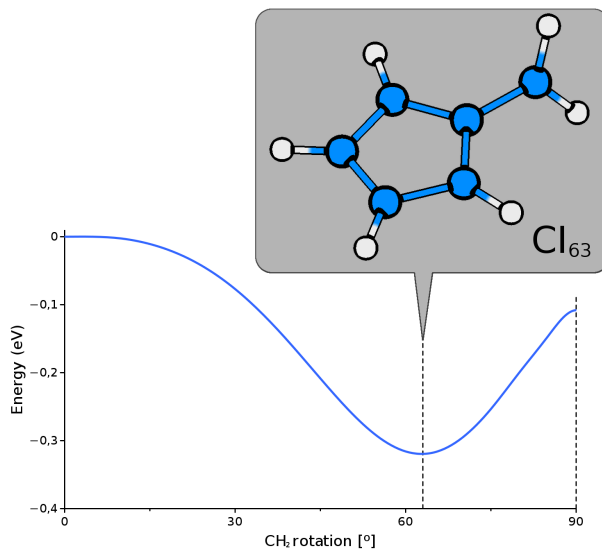


Figure 1.14: Seam energy plot of fulvene along the CH_2 rotation coordinate and molecular structure of the MECI.

very low quantum yield.

Finally, Q_{x_2} and θ show a large change in energy difference and are essential to describe the PES. Q_{x_2} with θ and φ are also needed to describe the coupling terms between the states, essential for quantifying the interconversion rate (section 1.1.1).

The electronic structure of fulvene is very rich. In the planar structure, the ground state and the first excited state have A_1 and B_2 symmetry respectively in the C_{2v} structure. Along the CH_2 rotation, the symmetry is lowered to C_2 and the states are A and B . At perpendicular structure, the fulvene recovers C_{2v} symmetry and the states obtain A_2 and B_1 symmetry respectively. In this situation, the S_2 has A symmetry and correlates with S_0 diabatically. Luckily, the states are separated by 1.9eV at CASSCF level and can be treated separately.

In chapter 5, all these theoretical data are used to simulate a control strategy in fulvene with quantum dynamics, where only some modes can be used (see section 2.4.1) and a complete study of the seam is needed.

Chapter 2

Theory and Methods

Modern quantum chemistry has different tools, approximations and methods for studying atoms and molecules. A great part of this thesis is about developing new methods, but existing methods and theory levels are also used. For this reason, a short theoretical explanation is given in this chapter. The chapter is divided principally into two parts: theory (sections 1 and 2) and methods (sections 3 and 4).

2.1 Schrödinger equation

Quantum mechanics has a main equation: the Schrödinger equation.

$$i\hbar\frac{\partial}{\partial t}\Psi(R,t) = \hat{H}\Psi(R,t) \quad (2.1)$$

where $\Psi(R,t)$ is the wave function of the system that contains all system information, R and t are the position and time and \hat{H} is the energy operator, the Hamiltonian, the operator whose eigenvalues give the possible energies of the system. The resolution of this differential equation gives maximum information about the studied system, the wave function. The total energy operator is formulated with different postulates of quantum mechanics, but, in the position picture, a system with N electrons, M nuclei and with no perturbation has the

following Hamiltonian in atomic units (a.u.):

$$\begin{aligned} \hat{H} = & \sum_{i=1}^N \hat{T}_i^e + \sum_{i=1}^M \hat{T}_i^n + \sum_{i=1}^N \sum_{j=1}^M \hat{V}_{i,j}^{e,n} + \sum_{i=1}^N \sum_{j>i}^N \hat{V}_{i,j}^{e,e} + \sum_{i=1}^M \sum_{j>i}^M \hat{V}_{i,j}^{n,n} = \\ & -\frac{1}{2} \sum_{i=1}^N \nabla_i^2 - \frac{1}{2} \sum_{i=1}^M \frac{1}{M_i} \nabla_i^2 + \sum_{i=1}^N \sum_{j=1}^M \frac{Z_j}{|r_{i,j}|} + \sum_{i=1}^N \sum_{j>i}^N \frac{1}{|r_{i,j}|} + \sum_{i=1}^M \sum_{j>i}^M \frac{Z_j Z_i}{|r_{i,j}|} \end{aligned} \quad (2.2)$$

where T and V are the kinetic and potential operators, respectively; ∇ is the Laplace operator, $|r_{i,j}|$ is the distance between two bodies and Z_i and M_i is the nuclear charge and mass of the i atom, respectively. The energy operators are separated as affecting nuclei (labeled as n), electrons (e), or both ($e - n$).

When the Hamiltonian is not time-dependent, the Schrödinger equation gives the stationary states of the system when there is no perturbation such as electromagnetic radiation. It can be solved easier because the position and the energies do not depend on time and thus, mathematically, wave functions are separable into two independent parts.

$$\Psi(R, t) = \Psi(R)\Psi_t(t) \quad (2.3)$$

Since the wave function is separable, the first step of the resolutions is simple and it can be found in a lot of books on quantum mechanics and quantum chemistry. The time-dependent part has the following function:

$$\Psi_t(t) = e^{\frac{-i\varepsilon t}{\hbar}} \quad (2.4)$$

and the position wave function is obtained with the following equation:

$$\hat{H}\Psi(R) = \varepsilon\Psi(R) \quad (2.5)$$

where ε is the energy of the state. It is very common practice to call the last equation (2.5) Time-Independent Schrödinger Equation (TISE) and first equation (2.1) Time-Dependent Schrödinger Equation (TDSE), although the TDSE is the basis of the TISE equation. Unfortunately, the Schrödinger equation only has an analytical solution for the hydrogen atom. Larger systems need different approximation methods to obtain the energy and wave function.

2.2 Born-Oppenheimer approximation

The Born-Oppenheimer approximation³ is probably the central approximation in current quantum chemistry. It is based on the mass difference between the nuclei and electrons. There are different ways to explain the approximation, but, in this thesis, the most theoretical one is used because it can help to explain when the approximation is broken. The mass of electrons is about 1/1836 that of the proton. Therefore, the momentum and kinetic energy of the nuclei are lower than that of the electrons. So, one can separate the wave function into two parts, nuclear and electronic:

$$\Psi(R) = \Psi(q, r) = \psi(q)\varphi(q, r) = \psi\varphi \quad (2.6)$$

where q and r are the coordinates of nuclei and electrons respectively. Taking into account how the kinetic energy operator of the nuclei is applied on this wave function:

$$\hat{T}^n\psi\varphi = \psi\hat{T}^n\varphi + \varphi\hat{T}^n\psi - \sum_{i=1}^M \frac{\nabla_i\psi\nabla_i\varphi}{M_i} \quad (2.7)$$

the TISE (equation 2.5) reaches the following form (all terms are divided by Ψ):

$$\begin{aligned} & \frac{1}{\varphi}\hat{T}^e\varphi + \frac{1}{\psi}\hat{T}^n\psi \\ & + \frac{1}{\varphi}\hat{T}^n\varphi - \frac{1}{\psi\varphi} \sum_{I=1}^M \frac{\nabla_i\psi\nabla_i\varphi}{M_i} \\ & + \frac{1}{\varphi}\hat{V}^{e,n}\frac{1}{\varphi} + \frac{1}{\varphi}\hat{V}^{e,e}\frac{1}{\varphi} + \hat{V}^{n,n} = \varepsilon \end{aligned} \quad (2.8)$$

This is the point when the B-O approximation is applied. If electrons are faster than nuclei, the electrons can adapt instantaneously to nuclear change and, in practice, they always follow the nuclei and are at equilibrium. Therefore, the changes are extremely smooth and one can approximate the $\nabla_i\varphi$ term to zero. With this approximation, the third and fourth terms of equation 2.8 are null and the eigenvalue equation is simplified:

$$\frac{1}{\varphi} \left(\hat{T}^e + \hat{V}^{e,n} + \hat{V}^{e,e} \right) \varphi + \hat{V}^{n,n} = \varepsilon - \frac{1}{\psi}\hat{T}^n\psi = \varepsilon^e \quad (2.9)$$

In this form, the TISE can be separated into nuclear and electronic eigenvalue equations, involving the first and the second term of the equation, respectively. The first term is the electronic equation and, normally, it is called electronic TISE or simply TISE.

$$\left(\hat{T}^e + \hat{V}^{e,n} + \hat{V}^{e,e}\right)\varphi = (\varepsilon^e - \hat{V}^{n,n})\varphi \quad (2.10)$$

The electronic TISE can be solved for fixed nuclei, where the φ only depends on q parametrically, shown as $\varphi(r; q)$. The ε^e is defined as the potential energy that affects the nuclei at particular coordinates. Since this equation depends on q , this can be repeated at any set of nuclear positions and the potential energy can be described as a function of the nuclear geometry. This function is normally called Potential Energy Surface (PES) or Potential Energy Hyper-surface (PEH). On the other hand, more qualitative descriptions²⁸ of the B-O approximation can deduce this equation quickly with the simple approximation $\hat{T}^n = 0$, where the nuclei are practically immobile with respect to the electrons. Finally, the second and third terms of equation 2.9 are the eigenvalue equation of nuclei.

$$\left(\hat{T}^n + \varepsilon^e\right)\psi = \varepsilon\psi \quad (2.11)$$

where ε^e is the potential energy operation of the nuclei. ε^e is often written as $\hat{W}(q)$ in matrix multistate equation or simply as $\varepsilon(q)$ in this case. It is needed as an operator, not a simple value. For this reason, the complete PES is needed, used as an operator, if the nuclear equation has to be solved.

2.2.1 Potential Energy Surface

The B-O approximation works really well in many cases, where the states of interest is well separated from the others ones. Therefore, the molecular structure can be studied with the potential energy of different nuclear positions. The PES, or PEH, of a molecular system can be defined as the potential energy function of the system with respect to the geometry of the nuclei. Usually, it is called PES but strictly it should be called PEH for systems bigger than two atoms because the

representation needs $3N-6+1$ dimensions (N is the number of atoms and the '+1' is the extra dimension for the energy). However, in this thesis the term PES is used.

The usual way to obtain the PES of any molecular system is to solve the electronic TISE for some geometries of the system. Since a correct resolution of the TISE obtains different solutions that are the different states of the electrons of the system, different PES can be obtained for every electronic state of the system.

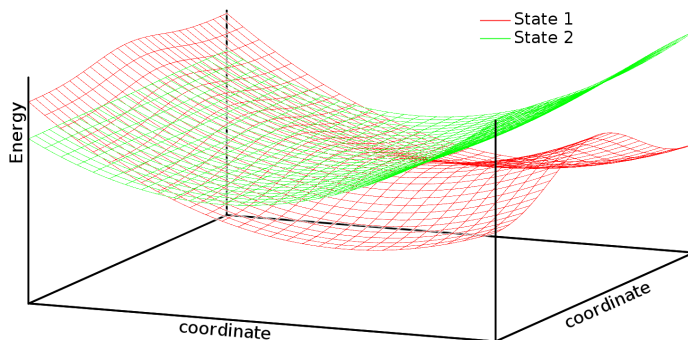


Figure 2.1: Potential Energy Surface of two states in two coordinates.

The PES is an excellent way to study the physics and reactions of systems because a PES, such as figure 2.1, can be represented as a landscape with valleys, peaks and saddle points. The valleys of PES represent stationary structures like reactants, intermediates or products of a reaction. The minimum position of these valleys is the equilibrium structure, and the energy difference between equilibrium structure of reactants and products is the energy of the reactions. On the other hand, the highest point on the lowest energy path between products and reactants is the TS of the reactions. In GS chemistry, the study of the ground state PES is sufficient to obtain the parameters of the reactions. However, in photochemistry, two or more states need to be considered to study the excited state reactions. Furthermore, the PES of different states have different topology so minima are different for each state and independent studies for all states involved are required. Moreover, thanks to the different topology of the

PES, the CI and seams are possible and they play an important role in photochemistry.

The study of the PES can give data about the equilibrium points, such as minima, TS or MECI for photoreactions. Therefore, the usual practice is to study the PES, finding minima, TS and MECI. Reaction paths, which connect the critical points, can complete the mechanistic picture to understand the reactions.

2.2.2 Diabatic and adiabatic picture

The PES, as a solution of the electronic TISE within the B-O approximation, is adiabatic by definition because the electrons adapt instantaneously at changes of nucleus. This is normally known as the adiabatic picture. The adiabatic picture, with B-O approximation and adiabatic PES, works correctly in most molecular systems. However, the radiationless processes, as we saw in chapter 1.1.1, defy the adiabatic representation. In the particular case of the CI, it is easy to see the reason why the B-O approximation is broken. The B-O is based on $\nabla_i\varphi$ being extremely small, at the CI this is not the case, the electronic wave function changes with a very small change in the nuclei position. Thus, $\nabla_i\varphi$ is not zero and the adiabatic PES is not the correct solution.

The diabatic picture appears if the nuclear TISE is solved without the B-O approximation. Another way to express the full TISE (equation 2.5) of a molecular system, with electrons and nuclei, is:

$$\left[\hat{T}^e + \hat{V}^e(r) + \hat{T}^n + \hat{V}^{e-n}(q, r) + \hat{V}^n(q)\right] \Psi(q, r) = \varepsilon\Psi(q, r) \quad (2.12)$$

The total wave function can be expanded as a set of $\psi(q)\varphi(r; q)$, solutions of the B-O approximation.

$$\Psi(q, r) = \sum_k \psi_k(q)\varphi_k(r; q) \quad (2.13)$$

Inserting this expansion in atomic units into TISE (equation 2.5), joining some terms and solving the electronic problem, the equation

reaches the following form:

$$[\hat{T}^n + \hat{W}_i^n(q) - \varepsilon] \psi_i = \frac{\hbar}{2} \sum_j \left(\sum_k \langle \varphi_i | \nabla_k^2 | \varphi_j \rangle + 2 \langle \varphi_i | \nabla_k | \varphi_j \rangle \nabla_k \right) \psi_j \quad (2.14)$$

where i is the state of the problem and \hat{W}_i^n is the i term of the adiabatic potential energy matrix. This formula is the i nuclear diabatic TISE of the system of connected equations. The right-hand side contains the non-adiabatic coupling terms. These terms are simplified in the B-O approximation because $\nabla_i \varphi = 0$. Thus, these terms indicate the magnitude of how good B-O is.

It is usual to transform the non-adiabatic term into a new matrix operator,

$$\Lambda_{i,j} = \frac{\hbar}{2} (G_{i,j} + 2F_{i,j} \nabla) \quad (2.15)$$

where the non-adiabatic coupling terms are joined in two operators.

$$G_{i,j} = \sum_k \langle \varphi_i | \nabla_k^2 | \varphi_j \rangle \quad F_{i,j} = \sum_k \langle \varphi_i | \nabla_k | \varphi_j \rangle \quad (2.16)$$

The full nuclear TISE, with the non-adiabatic operator, can be written as:

$$(\hat{T}_i^n + \hat{W}^n) \psi_i - \sum_j \Lambda_{i,j} \psi_j = \varepsilon_i \psi_i \quad (2.17)$$

However, the electronic functions can be chosen so that the non-adiabatic operator matrix (Λ) vanishes. In this case, a new non-diagonal potential matrix is obtained, called diabatic, and it is the principal representation of the diabatic picture. The nuclear TISE is written

$$\hat{T}_i^n \psi_i - \sum_j W_{i,j}^d \psi_j = \varepsilon_i \psi_i \quad (2.18)$$

where $W_{i,j}$ describes the diabatic surfaces in the diagonal and the coupling between the electronic states in the non-diagonal terms. In this form, the eigenvalues of the diabatic potential matrix are adiabatic surfaces. Some differences exist between the two surfaces. The main difference is that ideally nature of the diabatic states does not depend

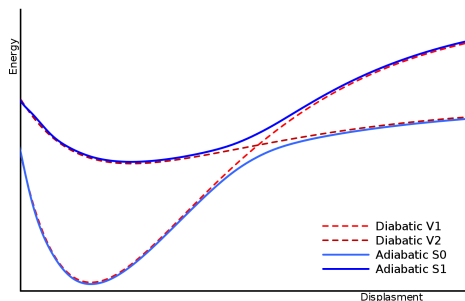


Figure 2.2: Schematic representation of the adiabatic and diabatic PES of two states.

on nuclear coordinates. Note that strictly speaking diabatic states cannot be defined²⁹ and in practice one works with quasi-diabatic states. Diabatic and adiabatic surfaces are related by a unitary transformation. A schematic representation is shown figure 2.2, where some couplings have been added to the diabatic surfaces to obtain the adiabatic ones.

The diabatic picture is more appropriate for quantum dynamics calculations because the kinetic operator is diagonal and the diabatic picture avoids the singularities associated with the CI. However, the diabatic states are difficult to obtain because the electronic calculation only gives adiabatic energies. For this reason, the diabatic representation is only used in some cases such as non-radiative process studies. In perturbation theory language, the adiabatic representation is a good zero-order approximation for ground-state reactions whereas the diabatic representation is the zero-order approximation for crossing points and excited state dynamic simulations.

More information about diabatic and adiabatic pictures, the operators and equations can be found in ref.^{30,31}

2.2.3 Geometry optimization

The exploration of the PES is very important in computational chemistry.^{32,33} Since the PES is a function of the molecular system geom-

etry, it can be optimised with the typical algorithms for optimising functions. The analytic expression of the PES is usually unknown, for this reason one can construct a local quadratic approximation with a truncated Taylor series:

$$\varepsilon(q) = \varepsilon(q_0) + g_0^T \Delta q + \frac{1}{2} \Delta q^T \mathbb{H}_0 \Delta q \quad (2.19)$$

where g_0 is the gradient $(\frac{\partial \varepsilon}{\partial q})$ in the position q_0 , \mathbb{H}_0 is the Hessian in the position q_0 and $\Delta q = q - q_0$. The negative of the gradient is the force vector acting on the system in that position. The zero gradient determines the stationary points in the PES. The Hessian at stationary points determines if the points are minima, maxima, TS or higher-order saddle points.

Newton-Raphson and Quasi-Newton-Raphson

Based on the local quadratic approximation of the PES, equation 2.19, Newton-Raphson is the most efficient and commonly used algorithm for optimising equilibrium geometries or TS. From the local approximation, the gradient is given by:

$$g(q) = g_0 + \mathbb{H}_0 \Delta q \quad (2.20)$$

At stationary points, the gradient is zero, $g(q) = 0$, so, in this approximation, the displacement which must go to the stationary point is:

$$\Delta q = -\mathbb{H}_0^{-1} \Delta g_0 \quad (2.21)$$

This is known as the Newton-Raphson step or, sometimes, the Newton step. Because the PES are rarely quadratic, several steps are required to obtain stationary points. For each step of N-R, the Hessian is calculated and inverted. The use of the Hessian also helps to characterize the stationary point at the end of the optimisation. The Hessian must have all positive eigenvalues for a structure to be a minimum. One negative, and only one, negative eigenvalue is required for a TS. Two or more gives a higher-order saddle point.

N-R needs the explicit calculation of the Hessian in every step, which can be rather costly. Quasi N-R uses an approximated Hessian that is updated at each step. Quasi N-R methods start with an inexpensive approximation of the Hessian or an exact Hessian and later recalculate the Hessian with an update:

$$\mathbb{H}_{new} = \mathbb{H}_{old} + \Delta\mathbb{H} \quad (2.22)$$

For a quadratic surface, the updated Hessian must fulfil the Newton condition.

$$\Delta g = \mathbb{H}_{new} \Delta q \quad (2.23)$$

where $\Delta g = g_{new} - g_{old}$ and $\Delta q = q_{new} - q_{old}$. An infinite number of update formulas can fulfil that condition, but only some of them are efficient: e.g. Symmetric Rank 1 (SR1).³⁴ However, the Broyden-Fletcher-Goldfarb-Shanno (BFGS) update³⁵⁻³⁸ is the most successful and widely used one.

$$\Delta\mathbb{H}^{BFGS} = \frac{\Delta g \Delta g^T}{\Delta g^T \Delta q} - \frac{\mathbb{H}^{old} \Delta q \Delta q^T \mathbb{H}^{old}}{\Delta q^T \mathbb{H}^{old} \Delta q} \quad (2.24)$$

Quasi N-R requires an initial Hessian to update. A scaled identity matrix may be sufficient in some cases, but an initial Hessian based on the initial structure is better, with simple empirical stretching, bending and torsion parameters. However, harder cases need a full exact Hessian to not fail the optimization process.

A standard quasi N-R approach needs to store and invert the Hessian in each step. For large optimizations, the inversion step can be a bottleneck, thus the updating process can be changed to update the inverse Hessian instead of the Hessian.

For TS optimization, it is important to keep the single negative eigenvalue, thus there are some Hessian updates which do not force the negative eigenvalue to be positive, such as the Powell-symmetric-Broyden update³⁹ or the Bofill update.⁴⁰

Constrained Optimization

In some cases, it may be necessary to apply some constraints to the geometry optimization. There are several methods which do this: penalty functions, projection methods and Lagrangian multipliers.

The most robust method is Lagrange multipliers, where a new function is used: the Lagrangian $L(q, \lambda)$.

$$L(q, \lambda) = \varepsilon(q) + \sum_i \lambda_i C_i(q) \quad (2.25)$$

where λ_i are the Lagrange multipliers, without any meaning, and $C_i(q)$ are the constraint conditions. There are as many multipliers as constraints. Optimizing the new function with all the new variables establishes the constrained optimization in the PES. In the local quadratic approximation of the PES, the equations are similar to N-R.

$$\begin{aligned} \frac{\partial L(q)}{\partial q} &= g_0 + \mathbb{H}_0 + \sum_i \lambda_i \frac{\partial C_i(q)}{\partial q} = 0 \\ \frac{\partial L(q)}{\partial \lambda_i} &= C_i(q) = 0 \end{aligned} \quad (2.26)$$

Generally, the convergence of Lagrange constrained optimization is faster than the others.

On the other hand, an easy way of applying linear constraints is the projection method. A projector \mathbf{P} can be used to remove the displacement in the constrained directions from the steps. The projector has a matrix form:

$$\mathbf{P} = \mathbb{I} - \sum_i \frac{c_i c_i^T}{|c_i|^2} \quad (2.27)$$

where c_i is a set of orthogonal constraint vectors. This constraint method is very easy to use in the quadratic approximation, because the projector can be applied to the gradients and Hessians.

$$\mathbf{P} g_0 + \mathbf{P} \mathbb{H}_0 \mathbf{P} + \alpha (\mathbb{I} - \mathbf{P}) = 0 \quad (2.28)$$

Since the Hessian is inverted in N-R, an extra term is added to avoid problems with the inversion, because the projector makes the eigenvalues along the constraint directions zero. In this case, α is a large

number which is very small when inverted.

Finally, a very simple way of applying constraints is the penalty function. In this method, the conditions, $C_i(q) = 0$, are imposed by adding an extra term, $\alpha(C_i(q))^2$, to the potential energy. Later, the optimization is performed with the new potential energy. These extra terms may make the convergence much slower than for the other methods.

Coordinates

The coordinates of molecular systems are always an interesting topic in quantum chemistry. In the particular case of PES optimization, certain coordinate sets are commonly used. In principle, any complete set of coordinates can be used to represent a molecular system. However, a good set of coordinates can improve the number of steps in the optimization. The Hessian, an important part of the local quadratic approximation, can show some favourable aspects with a good coordinate system. For example, the combination of rigid coordinates with very flexible ones gives a mixture of small and big eigenvalues in the Hessian that does not help with the optimization. Strong coupling between coordinates is another way to slow down optimization algorithms because the non-diagonal matrix elements of the Hessian are comparable with the diagonal ones. If the minima are characterized by strong anharmonicity or the valleys are strongly curved, the local second-order approximation fails because the Hessian changes rapidly with geometry.

The simplest and most universal system coordinates are Cartesian. Most potential energy and gradient calculations are carried out in Cartesian coordinates. However, Cartesian coordinates do not reflect the chemical structure and sometimes strong couplings between the coordinates make the optimization difficult. Moreover, Cartesian coordinates optimization need a simple constraint because the coordinates have variables that describe the rotation and translation.

Internal coordinates are composed of bond lengths and angles of the molecules forming a set of $3N-6$ variables ($3N-5$ in linear molecules; N is the number of atoms). They are more descriptive of the molecular

structure and the couplings between stretches, bends and torsions are usually small. An example of internal coordinates is the z-matrix.⁴¹ Finally, redundant internal coordinates⁴² are composed by the set of all bonds, valence angles and torsions, representing the intrinsic connectivity and flexibility of the molecule and introducing some redundancy. Redundant coordinates were demonstrated^{43,44} to be the best choice for minimizing the energy of polyatomic molecules. For this reason, all geometry optimizations in this thesis were calculated with them. In fact, they are commonly used in most computational quantum chemistry programs, e.g. Gaussian.⁴⁵ However, the variables normally surpass 3N-6 variables for the redundancy. This fact makes non-trivial several operation such as transformation between redundant and other coordinates or inversions of Hessians. The transformation between redundant and Cartesian coordinates is essential because the gradient and Hessian of most quantum methods are calculated in Cartesian. Therefore, one can define a non-square matrix \mathbb{B} that transforms the Cartesian displacements to internal redundant ones with the infinitesimal displacement:

$$\delta q = \mathbb{B}\delta x \quad (2.29)$$

where δq is a redundant internal displacement, δx is a Cartesian displacement and \mathbb{B} is a matrix where the components are defined as $\frac{\partial q_i}{\partial x_i}$. Then, the gradient transformation is given by:

$$\mathbb{B}g_q = g_x \quad (2.30)$$

where g_x and g_q are the gradients in Cartesian and in internal redundant coordinates respectively. Since \mathbb{B} is rectangular, the inverse transformation is not trivial:

$$g_q = \mathbb{G}^- \mathbb{B}g_x \quad (2.31)$$

where \mathbb{G} is $\mathbb{B}\mathbb{B}^T$ and \mathbb{G}^- is the generalized inverse, where only the non-zero eigenvalues are inverted. The Cartesian Hessian can be transformed with the help of $\mathbb{B}'_{ijk} = \frac{\partial^2 q_i}{\partial x_j \partial x_k}$ to:

$$\mathbb{B}^T \mathbb{H}_q \mathbb{B} + \mathbb{B}'^T g_q = \mathbb{H}_x \quad (2.32)$$

where \mathbb{H}_q and \mathbb{H}_x are the Hessian in Cartesian and redundant coordinates respectively. The inverse transformation is:

$$\mathbb{H}_q = \mathbb{G}^{-1} \mathbb{B} (\mathbb{H}_x - \mathbb{B}^T g_q) \mathbb{B}^T \mathbb{G}^{-1} \quad (2.33)$$

However, the Hessian transformation is not usually performed because the Hessian usually is updated, as shown in N-R section.

The redundancy in the coordinates gives zero eigenvalues in \mathbb{G} because the rank of the matrix is equal to the number of internal non-redundant coordinates. This happens in the Hessian, too. Thus some constraints are needed during the N-R optimization in redundant coordinates. Commonly, a projector is used to constrain the optimization and avoid the problem of the excess information of the redundant coordinates.

$$\mathbb{H}_q = \mathbb{P} \mathbb{H}_0 \mathbb{P} + \alpha (\mathbb{I} - \mathbb{P}) \quad (2.34)$$

where \mathbb{P} is:

$$\mathbb{P} = \mathbb{G}^{-1} \mathbb{G} = \mathbb{G} \mathbb{G}^{-1} \quad (2.35)$$

On the other hand, if the N-R is done in redundant coordinates, conversion of the step to Cartesian coordinates is needed. Since the transformation is curvilinear, the conversion has to be done in an iterative process, where the first estimation of new Cartesian coordinates is given by:

$$x_1 = x_0 + \mathbb{B}^T \mathbb{G}^{-1} \Delta q \quad (2.36)$$

where Δq is the step calculated with N-R. The obtained coordinates (x_1) are transformed to redundant (q_1) and compared with the previous ones ($q_1 - q_0$). The difference between the step and the comparison, $\Delta \Delta q = \Delta q - (q_1 - q_0)$, is used in equation 2.36 instead of the N-R step. This operation is done as an iterative process until $\Delta \Delta q$ become zero.

2.2.4 Conical Intersection Optimization

CI have a very important role in the photochemical reactions (section 1.1.2). The exploration of the CI inside the PES is fundamental for

understanding how photochemical reactions work. The seam can be studied in a similar way to the PES because it can be described as a hyperline or hypersurface of $n-2$ dimensions, where n is the number of coordinates of the molecular system. A very important point in the seam is the minimum energy point or MECI. There are a lot of algorithms for finding MECI and different strategies. They can be divided, principally, into three groups: Lagrangian, projected gradient and penalty term algorithms. Their similarity to constrained optimization is not a coincidence: CI optimizations are constrained optimizations in the PES where the constraint is that the energy difference between the states is zero. Local second-order approximation is usually used for the PES and first-order approximation for the constraint conditions, because first order is the most important term to break the degeneracy (section 1.1.2).

On the one hand, the Lagrange algorithms are the most efficient methods for constrained optimization. The most common Lagrange algorithms for finding MECI, proposed by Manaa and Yarkony,⁴⁶ is a Lagrange-Newton method. It is based on local second order approximation, where the conditions for the Lagrange multiplier (equation 2.25) are the conditions for the CI (equation 1.6). With this multiplier, the Lagrange function is trivial:

$$L(q, \lambda) = \varepsilon_I + \lambda_1 \Delta \varepsilon_{I,J} + \lambda_2 \langle \varphi_I | \hat{\mathbf{H}} | \varphi_J \rangle \quad (2.37)$$

where the initial function is the energy of one of the states, and the conditions are those of the CI. The energy function is usually changed by the energy average ($\frac{\varepsilon_I + \varepsilon_J}{2}$) to avoid abrupt variation near the CI. Applying the Newton-Raphson method to the Lagrange function, the Lagrange step is obtained:

$$\begin{bmatrix} \nabla \nabla L & x_1 & x_2 \\ x_1^T & 0 & 0 \\ x_2^T & 0 & 0 \end{bmatrix} \begin{bmatrix} \Delta q \\ \Delta \lambda_1 \\ \Delta \lambda_2 \end{bmatrix} = \begin{bmatrix} \nabla L \\ \Delta \varepsilon_{I,J} \\ 0 \end{bmatrix} \quad (2.38)$$

where the gradient with the average energy function is:

$$\nabla L = \left(\frac{g_I + g_J}{2} \right) + \lambda_1 x_1 + \lambda_2 x_2 \quad (2.39)$$

where g_I and g_J are the gradient of each state and x_1 and x_2 are the first-order BS vectors.

Quasi Newton-Raphson equations for updating the Hessian can be used too, so the complete form of the Lagrange Hessian is not necessary.

On the other hand, the most inefficient method for constrained optimization is penalty function. Ciminelli and coworkers⁴⁷ created a simple algorithm for optimizing MECI where the only constraint was the energy difference. For this reason, no knowledge of interstate coupling is needed and the algorithm is useful when x_2 is inaccessible for the electronic method. The algorithm defines the following function of the energy:

$$f(q) = \frac{\varepsilon_1 + \varepsilon_2}{2} + c_1 c_2^2 \ln \left[1 + \left(\frac{\varepsilon_1 - \varepsilon_2}{c_2} \right)^2 \right] \quad (2.40)$$

where c_1 and c_2 are constants which adjust the penalty function. The functions are separated in two parts, the average energy, which is the optimized function; and the penalty term, the term for reaching the degeneracy. c_1 determines the weight of the penalty term and c_2 controls how quickly the conical seam is approached. A correct optimization is done when c_1 tends to ∞ , but high values for c_1 make the optimization difficult. In the original paper, Ciminelli and coworkers⁴⁷ recommend some values for the constants.

Finally, there are the projected gradient algorithms, a compromise between efficiency and simplicity. They have a special relevance in this thesis. The projected gradient constrained optimization, that is explained in the last section (2.2.3), describes a projector matrix based on first-order conditions. In a MECI optimization, the conditions are given by the equation 1.6 and their first-order conditions by 1.7, so the projector matrix is formed from equation 2.27:

$$\mathbf{P} = \mathbb{I} - \frac{1}{|x_1|^2} x_1 x_1^T - \frac{1}{|x_2|^2} x_2 x_2^T \quad (2.41)$$

where x_1 and x_2 need to be orthogonal. This projector can be used in gradients and in Hessian and, when it is used, the optimization

process avoids changing the energy difference in first order. However, this method does not lead to a degeneracy: the constrained optimization only keeps the energy difference constant. For this reason, some extra terms are needed to complete the MECI algorithms. The most used algorithm to find MECI is that of Bearpark and co-workers,⁴⁸ the composed gradient algorithm. In this algorithm, the gradient is composed of two parts: the projected gradient and a penalty term to reach the degeneracy:

$$g_{CG} = g_P + f = \mathbf{P}g + f \quad (2.42)$$

where f is the penalty term, that is the "normalized" gradient of the function $(\Delta\varepsilon)^2$:

$$f = 2\Delta\varepsilon x_1 \frac{1}{|x_1|} \quad (2.43)$$

where x_1 is normalized because its length is not important. The composed gradient is used with quasi Newton-Raphson optimization equations, where the Hessian is updated with the gradient and the step. Because of that, the Hessian is not well defined in CG algorithm. This algorithm was included in the Gaussian program⁴⁵ more than 15 years ago. When it was tested, it was good enough to find MECI in different molecules.⁴⁸ But it has many problems of convergence in some molecules (Chapter 4). The basic problem is the extremely bad description of the Hessian, which loses the degeneracy easily. For this reason, different algorithms have been suggested in recent years.

The Composed Step (CS) algorithm, proposed by Sicilia and co-workers⁴⁹ and Anglada and co-workers,⁵⁰ tries to avoid the problems of the composed gradient with a better description of the Hessian inside the IS. In fact, Anglada and co-workers use the Lagrange multipliers formulation for obtaining a composed step algorithm based on a projection gradient.

A local quadratic approximation can be written for the IS:

$$\varepsilon_{IS}(q) = \varepsilon(q_0) + (g_{IS}^0)^T \Delta q + \frac{1}{2} \Delta q^T \mathbb{H}_{IS}^0 \Delta q \quad (2.44)$$

where g_{IS} is the projected gradient (described previously) and \mathbb{H}_{IS} is the Hessian inside the intersection space, a Hessian that does not change the energy difference (described in the following subsection). Thus, a Newton-Raphson optimization can be carried out:

$$\Delta q_{IS} = \mathbb{H}_{IS}^{-1} g_{IS} \quad (2.45)$$

This step is really stable and can find the minimum inside the IS and maintain perfectly the energy difference but, in the same way as the projected gradient algorithm, it does not lead to degeneracy. For this reason, the composed step algorithm is composed of two different steps: BS step and IS step, for reaching the degeneracy and for optimizing the IS space respectively.

$$\Delta q = \Delta q_{BS} + \Delta q_{IS} \quad (2.46)$$

The BS step uses a local first-order approximation of the energy difference:

$$\Delta \varepsilon(q) = \Delta \varepsilon(q_0) + \mathbf{x}_1^T \Delta q \quad (2.47)$$

If the step is forced to go in the \mathbf{x}_1 direction, the BS step is described by the following equation:

$$\Delta q_{BS} = \Delta \varepsilon \frac{1}{|\mathbf{x}_1|^2} \mathbf{x}_1 \quad (2.48)$$

Unfortunately, this BS step reaches the degeneracy very slowly. For this reason, the Composed Gradient is used to obtain a structure near the degeneracy and later the composed step is used to search for the minimum with the stability of the best Hessian description. Chapter 4 shows results of these algorithms compared with the other projected gradient algorithms.

Finally, Double N-R (DNR) was described, implemented and tested in the thesis. This algorithm has a very good performance, as described in Chapter 4.

Intersection Space Hessian

The IS Hessian is important for CS algorithms and also for the study of the second-order properties of CI, MECI and IS. We first introduce the potential energy diabatic matrix for two states (\mathbb{W}).

$$\mathbb{W}(q) = f(\mathbf{x})\mathbb{I} + \begin{bmatrix} \frac{1}{2}(\alpha\mathbf{x}_1 + \frac{1}{2} \sum_{i,j}^n \Delta\mathbb{H}_{i,j}\mathbf{x}_i\mathbf{x}_j) & \beta\mathbf{x}_2 + \frac{1}{2} \sum_{i,j}^n \mathbb{E}_{i,j}\mathbf{x}_i\mathbf{x}_j \\ \beta\mathbf{x}_2 + \frac{1}{2} \sum_{i,j}^n \mathbb{E}_{i,j}\mathbf{x}_i\mathbf{x}_j & \frac{-1}{2}(\alpha\mathbf{x}_1 + \frac{1}{2} \sum_{i,j}^n \Delta\mathbb{H}_{i,j}\mathbf{x}_i\mathbf{x}_j) \end{bmatrix} \quad (2.49)$$

where the molecular system is separated in n modes, used as a coordinate system ($q = \mathbf{x}_1, \mathbf{x}_2, \mathbf{x}_3, \dots, \mathbf{x}_n$). The modes are divided into the first order BS (\mathbf{x}_1 and \mathbf{x}_2) and the others modes (\mathbf{x}_i , where $i > 2$), orthogonal to first-order BS. The matrices $\Delta\mathbb{H}$ and \mathbb{E} , introduced previously (equation 1.8), are the Hessian matrices of the CI conditions. $f(q)$ is a quadratic function which describes the average of the energies of the two states and depends on all n modes with a typical quadratic approximation:

$$f(q) = \sum_i^n \lambda_i \mathbf{x}_i + \sum_{i,j}^n \bar{\mathbb{H}}_{i,j} \mathbf{x}_i \mathbf{x}_j \quad (2.50)$$

where $\bar{\mathbb{H}}$ is the Hessian of the average energy of the two states. With this potential matrix, the energy of each state is the following:

$$\varepsilon_{1,2}(q) = f(q) \pm \frac{1}{2} \sqrt{(\alpha\mathbf{x}_1 + \frac{1}{2} \sum_{i,j}^n \Delta\mathbb{H}_{i,j}\mathbf{x}_i\mathbf{x}_j)^2 + 4(\beta\mathbf{x}_2 + \frac{1}{2} \sum_{i,j}^n \mathbb{E}_{i,j}\mathbf{x}_i\mathbf{x}_j)^2} \quad (2.51)$$

It is easy to see that the degeneracy is preserved if the root square term is zero. Thus, the coordinates need to fulfill the following conditions.

$$\alpha\mathbf{x}_1 + \frac{1}{2} \sum_{i,j}^n \Delta\mathbb{H}_{i,j}\mathbf{x}_i\mathbf{x}_j = 0 \quad (2.52)$$

$$\beta\mathbf{x}_2 + \frac{1}{2} \sum_{i,j}^n \mathbb{E}_{i,j}\mathbf{x}_i\mathbf{x}_j = 0 \quad (2.53)$$

Thus, it is possible to obtain a set of values of the first-order BS modes which keeps the energy degenerate.

$$\mathbf{x}_1 = \frac{\sum_{i,j}^n \Delta \mathbb{H}_{i,j} \mathbf{x}_i \mathbf{x}_j}{2\alpha} \quad (2.54)$$

$$\mathbf{x}_2 = \frac{\sum_{i,j}^n \mathbb{E}_{i,j} \mathbf{x}_i \mathbf{x}_j}{2\beta} \quad (2.55)$$

This expression can be substituted in the potential energy formula to obtain the energy inside the IS, where the two states are always degenerate.

$$\varepsilon_{IS}(q) = \frac{\lambda_1}{2\alpha} \sum_{i,j}^n \Delta \mathbb{H}_{i,j} \mathbf{x}_i \mathbf{x}_j + \frac{\lambda_2}{2\beta} \sum_{i,j}^n \mathbb{E}_{i,j} \mathbf{x}_i \mathbf{x}_j + \sum_{i,j}^n \bar{\mathbb{H}}_{i,j} \mathbf{x}_i \mathbf{x}_j \quad (2.56)$$

For simplicity, the first order terms outside the BS have been extracted in the following formula. The simplification makes obtaining the Hessian of the IS space trivial:

$$\mathbb{H}_{ISi,j} = \left(\frac{\partial \varepsilon_{IS}}{\partial \mathbf{x}_i \partial \mathbf{x}_j} \right) = \frac{1}{2} \left(\bar{\mathbb{H}}_{i,j} - \frac{\lambda_1}{\alpha} \Delta \mathbb{H}_{i,j} - \frac{\lambda_2}{\beta} \mathbb{E}_{i,j} \right) \quad (2.57)$$

This is the form of the Hessian of the IS energy and it can be used in the local quadratic approximation. It is used in the MECI algorithms CS and DNR (chapter 4), but it can also be used to analyse MECI or the IS and obtain a good description of the IS of the molecular system.⁹

2.3 Electronic methods

Obtaining the electronic energy of the molecular systems is fundamental to find the critical point in the PES or for obtaining the potential energy operator in the nuclear Schrödinger Equation. Unfortunately, the electronic TISE does not have analytical solutions for systems bigger than hydrogen atoms. Thus, different methods are required to find that energy.

2.3.1 Solving the Time Independent Schrödinger Equation

The electronic TISE using the B-O approximation has the following form:

$$\hat{H}(r; q)\varphi_n(r; q) = \varepsilon_n\varphi_n(r; q) \quad (2.58)$$

where $\varphi_n(r; q)$ is the electronic wavefunction in the state n at frozen nuclei, ε_n is the energy of that state and $\hat{H}(r; q)$ is the electronic Hamiltonian with the following form:

$$\hat{H}(r; q) = \sum_{i=1}^N \hat{T}_i^e(r) + \sum_{i=1}^N \sum_{j>i}^N \hat{V}_{i,j}^{e,e}(r) + \sum_{i=1}^N \sum_{j=1}^M \hat{V}_{i,j}^{e,n}(r; q) + \sum_{i=1}^M \sum_{j>i}^M \hat{V}_{i,j}^{n,n}(q) \quad (2.59)$$

where T^e is the kinetic energy operator and $\hat{V}^{e,e}, \hat{V}^{e,n}$ and $\hat{V}^{n,n}$ is the potential energy operator between the electrons and nuclei. The potential operators $\hat{V}^{e,n}$ and $\hat{V}^{n,n}$ are dependent on the coordinates of the frozen nuclei, q . The solution of this equation for any nuclear position gives the PES and the electronic wavefunction for the complete wavefunction solution. The wavefunction solution of the electronic problem can be written as a sum of different products of mono-electronic wavefunctions.

$$\varphi(r; q) = \varphi(r_1, \dots, r_n) = \sum_{j=1}^K \prod_{i=1}^N \chi_{i,j}(r_i) \quad (2.60)$$

where r_i are the coordinates of i electron, χ are different mono-electronic wave functions, N is the number of electrons of the system and K is a sufficiently large number to obtain the exact wavefunction. The coordinates of the electrons are commonly formed by four components, the three spatial dimensions (x, y, z) and a spin component (σ). The spin coordinate can only be α or β . A spin function is therefore added to mono-electronic wavefunctions.

$$\chi(r_i) = \phi(x_i, y_i, z_i)\omega(\sigma_i) \quad (2.61)$$

where the function of the spin has unknown form, but there are only two function which obey the next equality.

$$\langle \alpha^* | \alpha \rangle = \langle \beta^* | \beta \rangle = 1 \quad (2.62)$$

$$\langle \alpha^* | \beta \rangle = \langle \beta^* | \alpha \rangle = 0 \quad (2.63)$$

The use of the spin function simplifies the electronic TISE. However, since electrons are indistinguishable fermions, the electronic wavefunctions need to follow an additional requirement to respect the electronic nature. Pauli's principle says that the electronic wavefunctions are antisymmetric with respect to the change of two particles: they change the sign when the two particles exchange the their coordinates.

$$\varphi(r_1, \dots, r_i, \dots, r_j, \dots, r_n) = -\varphi(r_1, \dots, r_j, \dots, r_i, \dots, r_n) \quad (2.64)$$

Thus the electronic wavefunction not only has to satisfy the TISE, but should also be antisymmetric. Therefore, any combination of mono-electronic functions, as in equation 2.60, is not a correct solution. The simplest way to follow Pauli's principle is by using a Slater determinant as electronic wavefunction, a particular case of equation 2.60. A general Slater determinant for the N-electron formula is:

$$\varphi(r_1, \dots, r_n) = \hat{N} \begin{vmatrix} \chi_1(r_1) & \chi_2(r_1) & \dots & \chi_N(r_1) \\ \chi_1(r_2) & \chi_2(r_2) & \dots & \chi_N(r_2) \\ \vdots & \vdots & \ddots & \vdots \\ \chi_1(r_N) & \chi_2(r_N) & \dots & \chi_N(r_N) \end{vmatrix} \quad (2.65)$$

where χ are the mono-electronic wavefunctions and \hat{N} is the normalization term. The normalization term is $\frac{1}{\sqrt{N!}}$ if all mono-electronic functions are normalized. The rows of the Slater determinant correspond to coordinates of the same electron (Equation 2.61) and the columns correspond to the same mono-electronic spin function, often called orbital or spinorbital. The Slater determinant has N electrons occupying N orbitals without specifying which electron is in which orbital, so electrons remain indistinguishable. Moreover, the Slater

determinant is antisymmetric because when two rows are exchanged, the sign of the total determinant also changes.

The common notation for the determinants is the *brac-ket* notation.

$$\varphi(r_1, \dots, r_n) = |\chi_a(r_1)\chi_b(r_2) \dots \chi_k(r_N)\rangle = |\chi_a\chi_b \dots \chi_k\rangle \quad (2.66)$$

where in the second notation the electron coordinates are in order.

The Slater determinant follows Pauli's principle. For this reason, the so-called Fermi's hole is well described: two electrons with the same spin cannot be found in the same place. In this case, two columns would be the same and the total determinant would be zero.

Hartree-Fock

Finding the approximate solution of the TISE is not an easy task. One way to obtain it is to apply the variation principle. The variation principle says that if a wavefunction is a correct solution of the TISE, the expected value of the energy is always higher than the correct one.

$$\varepsilon_0^{\text{Exact}} < \varepsilon_0 = \langle \varphi_I^{\text{appr}} | \hat{H} | \varphi_I^{\text{appr}} \rangle \quad (2.67)$$

Therefore, the variation principle can be used to optimize the solution using some parameters or variation flexibility in the wavefunction and minimizing the energy with respect to the flexibility.

In the previous section, the Slater determinant has been described as the simplest antisymmetric wavefunction (equation 2.65). It can be used to describe the electronic states of the N-electron system as a correct solution. Thus, the variation principle can be used to obtain the best Slater determinant, the one with the minimum expected energy. The Hartree-Fock(HF)²⁸ approximation is the method which obtains the optimal spinorbitals to form a Slater determinant with the minimum total energy.

The principal HF equation is the following one-electron equation.

$$\hat{f}(i)\chi_i = \varepsilon_i\chi_i \quad (2.68)$$

where ε is the energy of the electron inside the i spinorbital (χ). $f(i)$ is the effective one-electron operator, called Fock operator:

$$\hat{f}(i) = -\frac{1}{2}\nabla_i^2 - \sum_{A=1}^M \frac{Z_A}{r_{iA}} + \nu^{HF}(i) \quad (2.69)$$

where the first two terms are kinetic energy and electron-nuclei interaction and $\nu^{HF}(i)$ is the average electronic potential that the i th electron experiences due to the presence of the other electrons. $\nu^{HF}(i)$ is equivalent to the "field" seen by the electrons and it depends on the spin orbitals of the other electrons. Therefore, a set of spinorbitals is needed to solve the equation and for obtaining a new one. Thus, the equation is non-linear and must be solved iteratively. For this reason, the procedure for solving HF is known as a self-consistent-field.

The solution of the HF equation gives a set of spinorbitals which are the optimal ones for forming a Slater determinant with minimum energy. The N first spinorbitals are called occupied and form the lowest-energy determinant. This determinant is the ground state. If some occupied spin orbitals are exchanged for another solution, called virtual, the formed determinant is an excited state.

The SCF is usually solved with a finite spatial basis set where the spinorbitals are expanded with a linear combination.

$$\chi_i(r_i) = \phi_i(x_i)\omega_i(\sigma_i) = \left(\sum_{\mu=1}^K a_{i,\mu}\phi_\mu(x_i) \right) \omega_i(\sigma_i) \quad (2.70)$$

where ϕ_μ are the basis set functions, K is the number of functions and $a_{i,\mu}$ is the coefficient of the linear combination. The larger basis set gives more flexibility in the expansion and better results can be obtained, lowering the expected value of the energy.

If the α and β electrons share the same spatial part, a matrix equation is set up with the basis set, normally known as the Roothaan equations.⁵¹

Unfortunately, HF has some limitations. For example, some systems cannot be described by a unique Slater determinant. The most common cases are some spin states that are linear combinations of determinants. On the other hand, HF describes *Fermi's* hole quite well,

because mathematically the Slater Determinant excludes the possibility of two electrons with the same spin in the same position, but it does not exclude the possibility of two electrons with different spin in the same position, the *Coulomb* hole. More determinants are needed to describe it correctly. Finally, the excited state is not well described with HF. In the SCF process, occupied orbitals are used to obtain the new ones, thus they are optimized in the process whereas virtual orbitals are not. Therefore, using virtual orbitals to form excited state determinants is not the best option for describing the ES.

Complete Active Space Self Consistent Field

As we saw in the last subsection, HF is not the ideal approximated method for solving the TISE in some systems. In the special case of the ES, the main topic of the thesis, HF does not provide an accurate solution. For this reason, some multideterminant (also known as multiconfigurational) methods have been developed, such as configuration interaction methods or Multi-Configurational Self-Consistent Field (MCSCF) methods.⁵² Among the MCSCF methods, there is the Complete Active Space Self Consistent Field, CAS or CASSCF.⁵³ In CASSCF, the electronic wavefunction is written as a linear combination of different determinants,

$$\varphi(r; q) = \sum_{i=1}^I c_i |\varphi_i\rangle \quad (2.71)$$

where each determinant is formed by N spinorbitals,

$$|\varphi_i\rangle = |\chi_a, \chi_b, \dots, \chi_k, \chi_{r_i}, \chi_{s_i}, \dots, \chi_{u_i}\rangle \quad (2.72)$$

and each spinorbital is another linear combination of the spatial basis set.

$$\chi_i = \left(\sum_{\mu=1}^K a_{i,\mu} \phi_{\mu} \right) \omega_i \quad (2.73)$$

The determinants are formed by different combinations of spinorbitals. These spinorbitals are divided into two spaces, active and inactive.

The inactive ones are also divided into two, occupied and virtual. These two are similar to HF: the occupied are the spinorbitals which are always occupied in the determinants, usually core orbitals, and the virtuals are the never occupied ones. The active space is used to perform the different combinations of spinorbitals used in the determinants. The active space usually includes the chemically relevant orbitals, such as the π system in excited state studies of organic molecules. In the HF picture, the inactive occupied orbitals are usually the most stable spinorbitals, such as core orbitals, the virtual orbitals are the most unstable spinorbitals and the active space is normally in between, using the last occupied and the first virtual orbitals to do the combinations. Figure 2.3 shows a scheme for the space division of the spinorbitals.

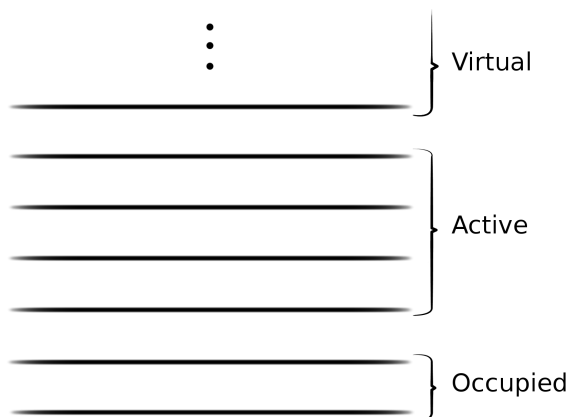


Figure 2.3: Scheme with the orbitals in HF picture of the orbital division in a CASSCF calculation.

As equation 2.72 shows, the different determinants are formed by occupied spinorbitals $(\chi_i, \chi_j, \dots, \chi_k)$ and a different combination of active space spinorbitals $(\chi_{\mu_i}, \chi_{\nu_i}, \dots, \chi_{\lambda_i})$. The combinations depend on the number of spinorbitals in the active space and the number of occupied spinorbitals or electrons inside the active space. For example, in a system with eight electrons, it is possible to use three inactive occupied spatial orbitals and four active spinorbitals, for six and two electrons

respectively. In this case, the calculation is known as a two electrons and two orbitals CASSCF or simply CAS(2,2). The electronic wave function of this example is written as:

$$\begin{aligned}
 \varphi(r; q) &= c_1 |\varphi_1\rangle + c_2 |\varphi_2\rangle + c_3 |\varphi_3\rangle + c_4 |\varphi_4\rangle + c_5 |\varphi_5\rangle + c_6 |\varphi_6\rangle \\
 |\varphi_1\rangle &= |\chi_{1,\alpha}, \chi_{1,\beta}, \chi_{2,\alpha}, \chi_{2,\beta}, \chi_{3,\alpha}, \chi_{3,\beta}, \chi_{4,\alpha}, \chi_{4,\beta}\rangle \\
 |\varphi_2\rangle &= |\chi_{1,\alpha}, \chi_{1,\beta}, \chi_{2,\alpha}, \chi_{2,\beta}, \chi_{3,\alpha}, \chi_{3,\beta}, \chi_{4,\alpha}, \chi_{5,\alpha}\rangle \\
 |\varphi_3\rangle &= |\chi_{1,\alpha}, \chi_{1,\beta}, \chi_{2,\alpha}, \chi_{2,\beta}, \chi_{3,\alpha}, \chi_{3,\beta}, \chi_{4,\alpha}, \chi_{5,\beta}\rangle \\
 |\varphi_4\rangle &= |\chi_{1,\alpha}, \chi_{1,\beta}, \chi_{2,\alpha}, \chi_{2,\beta}, \chi_{3,\alpha}, \chi_{3,\beta}, \chi_{5,\alpha}, \chi_{5,\beta}\rangle \\
 |\varphi_5\rangle &= |\chi_{1,\alpha}, \chi_{1,\beta}, \chi_{2,\alpha}, \chi_{2,\beta}, \chi_{3,\alpha}, \chi_{3,\beta}, \chi_{4,\beta}, \chi_{5,\alpha}\rangle \\
 |\varphi_6\rangle &= |\chi_{1,\alpha}, \chi_{1,\beta}, \chi_{2,\alpha}, \chi_{2,\beta}, \chi_{3,\alpha}, \chi_{3,\beta}, \chi_{5,\beta}, \chi_{5,\beta}\rangle
 \end{aligned}
 \tag{2.74}$$

This is a very simple case of CAS. However, the number of combinations readily increases, following the next formula:

$$I = \binom{A}{N_\alpha} \binom{A}{N_\beta}
 \tag{2.75}$$

where A is the number of active spatial spinorbitals, N_α and N_β are the number of electrons with alpha and beta spin respectively and I the number of determinants. For example in CAS(14,14) the number of Slater determinants stretches to 11,778,624. For this reason, the principal limitation of this method is the size of the active space, because the computational cost of CAS(16,16) is enormous.

In the CASSCF procedure, the set of coefficients a_i and c_i , from the linear combination of the spinorbitals (equation 2.73) and the wavefunction (equation 2.71) respectively, are optimized at the same time, providing more flexibility in the same basis set. Unfortunately, this process is totally non-linear and CASSCF is an iterative procedure, where the two sets are converged in alternative cycles. Thus, the CAS active space is not the only limitation: systems with a lot of electrons can be out of reach computationally.

CAS is a highly complex method. The result of the method clearly depends on the active space: when the active space is more related with the system, more specific for the chemical problem, the best results are obtained. And the energies are better with a large active

space. Given the size limitation, the choice of active space is a hard task. There is not any formula for finding either the best orbitals or the ideal size. Each system requires a previous study to obtain the best results with CAS. However, there are some strategies for finding it, such as using all π system to study the excited state in molecules with double bonds.

On the other hand, the CAS solution is not the best solution as it is not the exact one. CAS is the full solution inside the active space with the basis set that is used. But outside the active space, the quality of the solution is similar to HF. For this reason, it is often said that CAS has static electronic correlation but not dynamic correlation. However, this fact is not completely true, because if the active space is big enough, dynamic correlation is included too, but principally, CASSCF includes static correlations. Other methods can include dynamic correlation such as Configuration-interaction Single and Doubles or second-order perturbation theory applied to CAS, known as CASPT2.^{54,55}

2.3.2 Molecular Mechanics

Evidently, the most precise way to obtain the potential energy is solving the TISE. However, computing the complete total quantum PES is a serious undertaking. In fact, obtaining the fully quantum potential energy of one geometry of a large bulky system is technically impossible: the approximate methods for solving the TISE previously presented require extensive computational effort and large systems are impossible. In this case, the potential energy can be obtained in another way: molecular mechanics (MM), where electrons are ignored completely, in contrast to the quantum mechanics (QM) electronic method of the previous section (2.3).

It is possible to consider the PES as an abstract function of the nuclear coordinates ($U(q)$), without any connection with the electronic TISE. This function is analytical, and it should be continuously differentiable. In the case of the bond distance of two atoms of the system,

A and B, the potential energy can be written as a Taylor series:

$$\varepsilon(r^{A-B}) = \varepsilon(r_0^{A-B}) + \left(\frac{d\varepsilon}{dr}\right)_0 (r^{A-B} - r_0^{A-B}) + \frac{1}{2} \left(\frac{d^2\varepsilon}{dr^2}\right)_0 (r^{A-B} - r_0^{A-B})^2 + \dots \quad (2.76)$$

where r^{A-B} is the bond distance. If a local quadratic approximation is done in the equilibrium point, where $\left(\frac{dU}{dr}\right)_0$ is zero, it is possible to write a function for the potential energy between these two atoms:

$$\varepsilon(r^{A-B}) = \frac{1}{2}k_{A-B} (r^{A-B} - r_{eq}^{A-B})^2 \quad (2.77)$$

where the second derivative of the energy is the force constant (k_{A-B}). Usually, the equilibrium distance between two atoms remains constant although the system is changed. Furthermore, the spectroscopic data show that the bonds between the same pair of atoms are extraordinarily similar, and usually they can be distinguished from the others in IR spectra. Thus, empirically, it is evident that the force constant is practically the same in different molecules. This phenomenon is called "transferability". Therefore, a list of different equilibrium constants and equilibrium distances can be produced for each pair of atoms. Assuming these concepts, the total bond potential energy can be obtained as the sum of the potential energy of all bonds. Following the same procedure, it is possible to obtain the total potential energy of the molecular system as a sum of different contributions.

$$\varepsilon(q) = \varepsilon_{bonds} + \varepsilon_{angle} + \varepsilon_{dihedral} + \varepsilon_{electrostatic} + \varepsilon_{vanderWaals} \quad (2.78)$$

where the potential energy is divided into five terms, depending on the nature of the potential energy. Each term has its own parameters and depends on two, three or four atoms.

There are different list of parameters and formulations known as Force Fields. Most of them are based on the same formula (equation 2.78). The principal difference lies in the parameters and how the atoms are considered. For example, different Force Fields are optimized to obtain the best results in proteins or in DNA, fitting the parameters

to experimental and theoretical data and considering the atoms that make up the system. All atoms can have different types in the parameters list, depending on the hybridization and the bonds which they form.

In the present work only the Universal force field (UFF)⁵⁶ is used. UFF is an all-atom potential containing parameters for every atom. The force field parameters are estimated by means of general rules based only on the element and its hybridization, in the attempt to include all atoms and all cases.

2.3.3 ONIOM

Different methods require different computational effort and different precision in the results of the potential energy. The Own N-layer Integrated molecular Orbital molecular Mechanics (ONIOM)⁵⁷⁻⁶² is a scheme to separate the molecular system into different layers and calculate them with different methods. Thus, it is possible to calculate some parts of the molecule accurately and the rest with a cheaper method. Often, ONIOM is confused with the QM/MM method, but it isn't. QM/MM is a scheme or method to combine QM methods and MM methods in the same calculations. But, technically, ONIOM can do QM:QM⁶³ or MM:MM. Also, ONIOM is a multilayer scheme, where the system can be divided into more than two⁵⁹ layers and a QM:QM:MM scheme is possible. ONIOM uses a very easy extrapolative scheme that avoids common errors of under- or over-counting interactions in typical QM/MM approaches, which use additive schemes. For this reason, commonly, ONIOM is used in QM:MM scheme.

With two layers, ONIOM gives the following formula for the potential energy:

$$\varepsilon_{\text{ONIOM}} = \varepsilon_{\text{Model}}^{\text{High Level}} + \varepsilon_{\text{Real}}^{\text{Low Level}} - \varepsilon_{\text{Model}}^{\text{Low Level}} \quad (2.79)$$

where the complete molecular system is named *Real* and the part where the high level method is applied is called *Model*; thus the system is divided into two layers, model and the rest. Following the equation, the real system is calculated with the low level method, the

cheapest one. The model is calculated with the high level method. The model is calculated with the low level too, to extrapolate the ONIOM energy. Therefore, the rest outside the model is only calculated with the low level method. For this reason, choosing the correct model is a prerequisite in an ONIOM calculation to obtain relevant results.

Sometimes, the division between the model and the low-level moiety implies cutting a boundary through covalent bonds. In this case, an additional treatment is required. ONIOM employs the common Link Atom (LA) approach, whereby the atoms of the rest are replaced by the LA, normally hydrogen. Thus, the Link Atom Connection (LAC) exchanges the covalent bond with the Link Atom Host (LAH) for LA. This division in ethane is shown in figure 2.4. In ONIOM, the position of the LA depends on the coordinates of the LAH in the real system, as follows,

$$q_{LA} = q_{LAC} + g(q_{LAH} - q_{LAC}) \quad (2.80)$$

where q_{LA}, q_{LAC} and q_{LAH} are the position of the LA, LAC and LAH atoms respectively and g is the scale factor, which depends on the three atoms. The LA approach eliminates degrees of freedom with respect to other approaches because scale factor is constrained to a fix

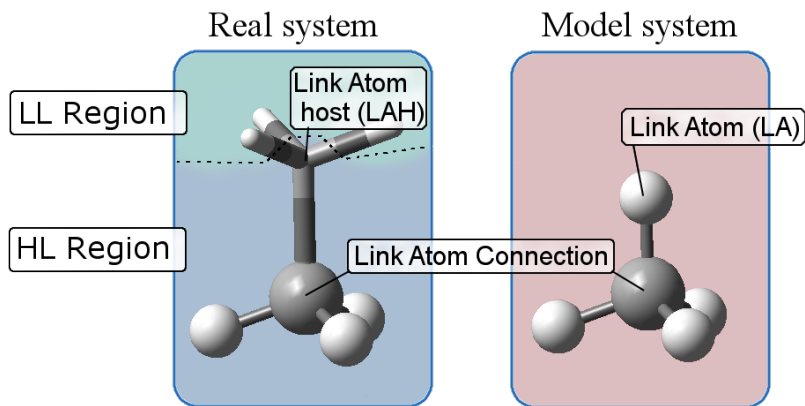


Figure 2.4: The real and the model molecular system in an ONIOM calculation in ethane. The LA, LAH and LAC are indicated.

value. Furthermore, the bond length has non-strange values in model and real system, and the stretching along the model is transferred to the real system and vice versa.

Similarly to the potential energy function, the gradient in ONIOM is simply evaluated with the gradient of three calculations. However, in this case, if a bond is cut in the division in different layers, a transformation is needed because the position of the LA in the model is not the same as in the complete molecular system. Using a Jacobian matrix transformation in the gradient of the model system, the total ONIOM gradient is a trivial sum of gradients.

$$g_{\text{ONIOM}} = g_{\text{Model}}^{\text{High Level}} J + g_{\text{Real}}^{\text{Low Level}} - g_{\text{Model}}^{\text{Low Level}} J \quad (2.81)$$

Optimizations with microiterations

In QM:MM ONIOM optimizations, since the computational cost of the MM methods is much lower than QM, it is more efficient to do a complete optimization of the MM part for each model step without optimizing the total ONIOM potential energy at the same time. The complete ONIOM gradient vector can be separated in two layers like the molecular system.

$$g_{\text{ONIOM}} = \begin{pmatrix} g_{\text{model}} \\ 0 \end{pmatrix} + \begin{pmatrix} 0 \\ g_{\text{rest}} \end{pmatrix} \quad (2.82)$$

The complete optimization in the MM part is done with g_{Rest} for calculating the steps, called microiterations.⁶⁰ g_{Rest} includes only MM parts, so it avoids any movement in the model layer in the microiterations. Moreover, the calculation of g_{Rest} is done with MM, making the microiterations very cheap. Later, g_{Model} is used to calculate the step in the model, normally called macroiteration. This gradient freezes the movement in the MM part. This gradient includes QM and MM components. The complete set of microiterations and the macroiteration perform the complete ONIOM step in QM:MM ONIOM calculations.

$$\Delta q = \begin{pmatrix} \Delta q_{\text{model}} \\ 0 \end{pmatrix} + \begin{pmatrix} 0 \\ \sum \Delta q_{\text{rest}} \end{pmatrix} \quad (2.83)$$

Mechanical Embedding and Electronic Embedding

There are two ways to deal with the electrostatic interaction between layers in QM:MM calculations: *classical* or *mechanical embedding* and *electronic embedding*. In the first one, ME, the different layers do not interact. The absence of the environment is especially important in the model high level calculation, where the model only receives sterical information from the ONIOM extrapolation formula. The electronic structure does not interact with the environment, which is a less accurate approximation to the real problem. On the other hand, the EE scheme incorporates cross-region electrostatic interactions in the model. In this scheme, the model system includes charges from the real system. These charges are included in all model calculations. In the case of QM calculations, the charges enter inside the Hamiltonian operator. Evidently, the wavefunction of the model system in the EE scheme is more accurate in the electrostatic description. However, the MM charges are usually used and they are relatively large at close distance. Thus, the EE scheme has an unavoidable problem: overpolarisation of the model wavefunction. The problem can be reduced,

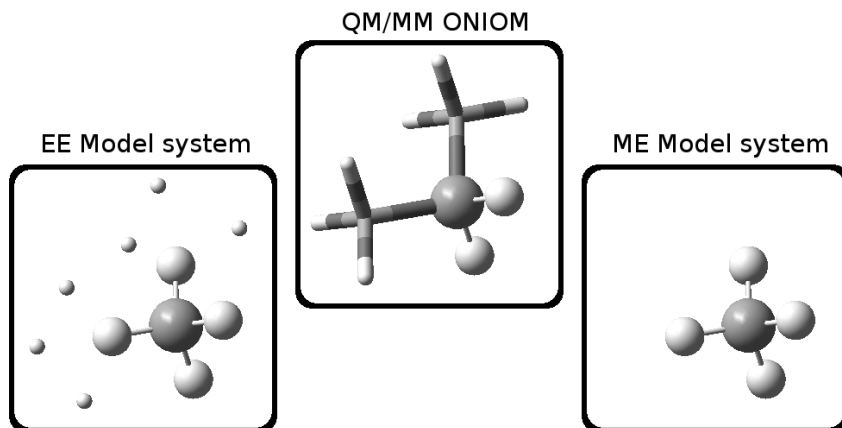


Figure 2.5: The real and the model molecular system in two ONIOM calculations in propane, using the EE and ME schemes. The dots in the EE calculation represent the point charges included in the high-level Hamiltonian.

however, by certain techniques.

Optimization with microiterations is another problem with EE. In this case, the separation of the gradient is possible, but the gradient of the rest depends on the QM calculation too, because the changes in the MM part change the wavefunction. For this reason, Friesner and co-workers⁶⁴ proposed a scheme where electrostatic potential (ESP) charges of the QM region are used for describing the perturbation to the exact gradient during the microiterations. After these microiterations, the ESP charges are re-calculated and the process is repeated as an iterative process, until the wavefunction converges.

ONIOM in the Excited State

Obtaining the potential energy of the excited state is much more computationally expensive than for the ground state and requires high-consuming methods like CASSCF. If a large system is calculated with ONIOM, the size of the model must be decreased radically to make it possible to calculate. However, the cheapest methods such as HF do not describe the ES correctly and, in fact, most MM force field do not have an ES potential energy function. For this reason, an approximation is required. Bearpark and coworkers proposed⁶⁵ using the ground state for the low level calculation, independently of whether the ONIOM calculation was for the ground or excited state. In this case, the excited state is calculated in the model system and the rest has no influence. Therefore, all excited state properties, like energy difference or first order BS are related to the model system.

$$\Delta\varepsilon_{\text{ONIOM}} = \Delta\varepsilon_{\text{Model}}^{\text{High Level}} \quad (2.84)$$

With that approximation, a QM:MM ONIOM calculation can be done in ES potential energy calculations. However, in such cases, the selection of the model is particularly important, because if some part which is important for the ES does not enter in the model, the error is enormous. For example, charge-transfer between the model and the rest of the system does not appear in that calculation.

2.4 Photoexcited molecular dynamics

The absorption process is a time-dependent perturbation that brings the system to a non-stationary state. In the cases of our study, this fact is important.

The major part of the Introduction is centred on understanding the electronic excited state as a stationary one, where the geometric structures on the potential surface of the molecular system have remarkable importance, such as CI or FC. Knowledge of these ES system structures helps to obtain a mechanistic picture and to predict the photoreactions. However, these points are reached because the systems are in non-stationary states after the radiation. This fact is equally as important as specific geometries, because it defines when and how these structures are reached. The main importance of the CI is that the system can reach them before the emission process starts. Thus, molecular dynamics are an essential tool for simulating non-stationary processes.

Interest in molecular dynamics has risen in the last three decades, where many femto-chemistry experiments needed to be explained. The recent advances in laser science have increased the interest in it. The molecular dynamics can be simulated theoretically with different forms to reveal the experimental facts. Theoretical simulations can show the movement on the atomic scale of the proteins or the change in the electronic density when they are excited by femto-lasers.

There are different kinds of theoretical dynamic simulations, depending on the description of the system. Principally, the system can be understood as quantum or classical, or a mix of them. For example, it is possible to use the quantum PES as the potential energy of the nuclei to run dynamic simulations using the classic Newton formulation or use a Force Field of MM to do classical molecular dynamics. The last case is common in the study of proteins or DNA. However, using the classical formulation loses the quantum effects such as tunnelling or radiationless relaxation. The only way to describe these effects in simulations correctly is to solve the TDSE.

2.4.1 Solving the Time-Dependent Schrödinger Equation

The most exact way to simulate the changes in molecular systems with time is to solve the TDSE. Solving the TDE can also be necessary for time-independent systems where the Hamiltonian is too complicated to compute all states. However, here we are more interested in the first case. As we saw in the first section of this chapter (2.1), when the Hamiltonian is time-dependent, TDSE has the form of the equation 2.1. The wavefunction cannot be separated into two parts, time and position, so the equation needs to be solved completely. Nonetheless, it is possible to separate the coordinates of electrons and nuclei as in TISE solutions. As we showed in the B-O approximation section (section 2.2), the principal difference between the two pictures is the form of the potential energy operator in the nuclear Schrödinger equation. Thus, TDSE can be solved in both pictures provided the correct PES is obtained previously.

The solutions of the TDSE are more complex than the TISE ones: there is one more variable, time. However, it is possible to obtain the density of the system at each time, as a snapshot, known as a wavepacket. The propagation of the wavepackets can describe the change of total density with time, the molecular "movement".

Like TISE, TDSE cannot be solved exactly for systems bigger than a hydrogen atom. Therefore, some approximated methods are used to solve it.

MCTDH

Multi-Configuration Time-Dependent Hartree (MCTDH)⁶⁶⁻⁶⁹ is the approximated method for solving any TDSE and was developed and implemented by Prof. H.-D. Meyer and coworkers.

The solution of the nuclear TDSE can be written as a Hartree product of M monodimensional functions (ϕ), known as *single-particle func-*

tions (SPFs).

$$\psi(q, t) = a(t) \prod_{i=1}^M \phi_i(q_i, t) \quad (2.85)$$

where M is the number of dimensions of the problem and $a(t)$ is the phase of the system. A finite primitive spatial basis set (χ) can be used to obtain the SPFs.

$$\phi(q, t) = \sum_{j=1}^K c_j(t) \chi_j(q_i) \quad (2.86)$$

The Hartree products can be used to solve the TDSE, in Time-Dependent Hartree methods, but they have some limitations.⁶⁶ As its name suggests, MCTDH gives flexibility: a linear combination of different Hartree products which is known as the *ansatz* wavefunction.

$$\psi(q, t) = \sum_{j_1}^{n_1} \dots \sum_{j_M}^{n_M} A_{j_1, \dots, j_M}(t) \prod_{i=1}^M \phi_i(q_i) \quad (2.87)$$

For simplicity, the expansion can be expressed by combinations of different Hartree products of all single-particle functions,

$$\psi(q, t) = \sum_{j=1}^J A_j(t) \Phi_j(q) \quad (2.88)$$

where J are the total number of combinations and $\Phi_j(q) = \prod_{i=1}^M \phi_{i,j}(q_i)$. There is a variational principle that can be applied to the TDSE, the Dirac-Frenkel variational principle.

$$\langle \delta\psi | \hat{H} - i\partial_t | \psi \rangle = 0 \quad (2.89)$$

With this variation principle, the TDSE can be solved using the form of equation 2.88 as a matrix equation.

MCTDH is a method for propagating the wavepacket on the PES. For this reason, the complete PES must be known globally. This is

the principal problem with MCTDH. The huge effort needed to generate the correct PES requires an extremely large grid of electronic calculations. Furthermore, the computational effort of the quantum dynamics grows quickly with the dimensions of the problem. Six or seven dimensions can be a great challenge, with enormous computational cost. For this reason, multi-layer⁷⁰ MCTDH was proposed a few years ago to save computational cost of large dimensional problems, making it possible to solve problems of twelve dimensions or more.

In spite of the computational cost and the effort required to obtain the PES, quantum dynamics are the only method which correctly describes the electromagnetic perturbations, such as the excitation process, because they are totally quantum phenomena. Moreover, quantum dynamics can describe the non-radiative transitions that occur at a CI correctly, which is essential to study of the ES. To summarize, the MCTDH method has been the method of choice in the dynamics calculations presented in Chapter 5 because it gives the best balance between computational efficiency and an accurate treatment of quantum effects.

Chapter 3

Objectives

In this thesis the theoretical modelling of excited states is approached from a double perspective, based on the main potential of theoretical and computational chemistry: the ability to rationalize mechanisms for existing reactions, and the application of this knowledge to design new reactions and new experimental approaches. In this context, the two main goals of this thesis are: (1) To develop new tools for the study of the ES PES and the rationalization of ES reactivity, namely CI optimization algorithms, and (2) to derive new strategies for one of the most important current experimental challenges, the control of reactivity with light.

The first objective is studying the topology of the PES of the excited state. As we saw in the Introduction, the behaviour of the excited state is based on the energy of the seam. If any CI of the seam is accessible in energy, a radiationless process has a high rate and deactivation can occur before radiation. Thus, obtaining the MECI is fundamental to study the topology of the ES. There are several algorithms for optimizing MECI with different performance. Starting from the existing projected gradient algorithms, CG and CG-CS, the goals of this part are:

- Device a new CI algorithm optimization to improve the approach to the seam and thus reducing the total steps in MECI optimizations.

- Compare the performance in fully quantum calculations, in number of steps, of the new algorithm in front of CG and CG-CS on the optimization of a test set of 11 compounds.
- Implement the three projected gradient algorithms inside the ME-ONIOM scheme with microiterations.
- Study the performance of the algorithms inside ONIOM scheme in a systematic test with bulky molecules.
- Study the viability of the new implementation for finding MECI inside crystal structures with the example of diphenyl dibenzofulvene (DPDBF), studying the complete topology of the molecule.

The second objective is proposing new strategies for the control of photo-processes. The target system is the well-known fulvene molecule, which has a barrierless rotation in ES but where the main deactivation route is a planar structure CI. The main idea is to use the existing knowledge of the decay mechanism to develop the control scheme. Since the excited system is in a non-stationary state, quantum dynamics are mandatory for a realistic simulation of the control, and the available 4-dimensional model is used as a starting point. The proposed approach is based on the non-resonant Stark effect, where the potential energy surfaces are shifted with a non-resonant field, and the idea is to shift the energy and position of the seam with the field. Starting from these ideas, the main goals of the second part are:

- Study of the effects of the non-resonant electric field on the topology of the fulvene PES.
- Include the non-resonant electric field in the available four-dimensional model.
- Re-parametrize the model with the new field parameters based on *ab initio* calculations.

- Study the viability of the photorotation of the exocyclic double bond of fulvene (section 1.2.2) control strategy with the non-resonant Stark effect at the quantum dynamics level, using the new model and a pair of external fields to simulate the pump and control laser pulses.

Chapter 4

New Conical Intersection Optimization algorithm: Double Newton-Raphson

4.1 Conical Intersection Optimization Based on a Double Newton-Raphson Algo- rithm Using Composed Steps

S. Ruiz-Barragán, M. Robb, Ll. Blancafort

J. Chem. Theory Comput., 9, 2013, 1433-1442

Conical Intersection Optimization Based on a Double Newton–Raphson Algorithm Using Composed Steps

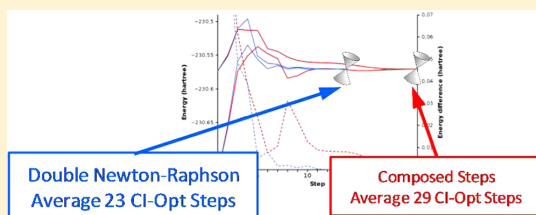
Sergi Ruiz-Barragan,[†] Michael A. Robb,[‡] and Lluís Blancafort^{*,†}

[†]Institut de Química Computacional and Department de Química, University of Girona, 17071 Girona, Spain

[‡]Department of Chemistry, Imperial College, London SW7 2AZ, United Kingdom

S Supporting Information

ABSTRACT: An algorithm for conical intersection optimization based on a double Newton–Raphson step (DNR) has been implemented and tested in 11 cases using CASSCF as the electronic structure method. The optimization is carried out in redundant coordinates, and the steps are the sum of two independent Newton–Raphson steps. The first step is carried out to reach the energy degeneracy and uses the gradient of the energy difference between the crossing states and the so-called branching space Hessian. The second step minimizes the energy in the intersection space and uses the projected excited state gradient and the intersection space Hessian. The branching and intersection space Hessians are obtained with a Broyden–Fletcher–Goldfarb–Shanno update from the gradient difference and projected excited state gradients, respectively. In some cases, mixing of the quasi-degenerate states near the seam causes changes in the direction of the gradient difference vector and induces a loss of the degeneracy. This behavior is avoided switching to a composed step (CS) algorithm [Sicilia et al. *J. Chem. Theory Comput.* **2008**, *4*, 27], i.e., a hybrid DNR-CS implementation. Compared to the composed gradient (CG) [Bearpark et al. *Chem. Phys. Lett.* **1994**, *223*, 269] and hybrid CG-CS algorithms, the DNR-CS algorithm reaches the MECI in 30% and 15% less steps, respectively. The improvement occurs mostly because the approach to the seam is more efficient, and a degeneracy threshold of 0.001 hartree is reached at lower energies than in the CG and CG-CS cases.



INTRODUCTION

Conical intersections (CIs) are very important in molecular photochemistry and photophysics.¹ They provide efficient funnels for the decay from the excited state to the ground state, or for transitions between different excited states, and therefore they play a key role in ultrafast excited state processes. They account for excited state processes of molecules in the gas phase and in solution and also of chromophores embedded in biological systems such as DNA, rhodopsin, the photoactive yellow protein, or others (see refs 2 and 3, and references therein).

In computational photochemistry, the first approach to study a photochemical process is usually the computation of critical points on the surface.⁴ In this approach, the calculation of minimum energy conical intersection (MECI) structures is particularly relevant. However, locating these points can be difficult because they often have counterintuitive structures that are difficult to predict *a priori*. Therefore, efficient algorithms to optimize these points are important. Such algorithms are also necessary for their further use in different contexts, such as the implementation in QM/MM formalisms. Although the first CI optimization algorithms were developed about two decades ago,⁵ efforts to develop new algorithms are ongoing and are directed along several directions. The first one is the search for more efficient optimization algorithms, which is the main aim of this paper.⁶ Another line is the development of approaches that do not require the interstate coupling vector (one of the two directions

that breaks the degeneracy at the intersection, see details below), which is difficult to calculate with many electronic structure methods.⁷ Finally, several methods have been developed that include environmental effects, mostly based on hybrid schemes.⁸

CIs are crossings of potential energy surfaces of the same multiplicity that form an $(N - 2)$ -dimensional subspace, usually called intersection space or seam of intersection. Here, N is the number of degrees of freedom of the surface, which is equal to $3n - 6$, where n is the number of atoms. The degeneracy is lifted in first order along the remaining two directions of the surface, which form the so-called branching space. Computationally, the problem of locating the MECI is an energy minimization subject to the constraint of energy degeneracy between the states. This is equivalent to an optimization in the $(N - 2)$ dimensional subspace. This problem can be tackled with three general methods: penalty function methods, projected gradient methods, and Lagrange–Newton ones. These methods have been compared previously.¹⁰ In this paper, we focus on projected gradient methods, and we present an improved optimization scheme of this type.

The CI minimization conditions can be described as

$$\Delta E = 0 \quad (1)$$

Received: December 3, 2012

Published: January 15, 2013

$$\mathbf{g}_{\text{IS}} = 0 \quad (2)$$

where ΔE is the energy difference between the two states and \mathbf{g}_{IS} is the so-called intersection space gradient, i.e., the projection of the gradient in the intersection space. The main idea of the projected gradient methods is to carry out a Newton–Raphson optimization driven by \mathbf{g}_{IS} . This gradient is obtained by projecting out the branching space vectors, which are given by eqs 3 and 4:

$$\mathbf{x}_1 = \frac{\partial(E_2 - E_1)}{\partial \mathbf{q}} \quad (3)$$

$$\mathbf{x}_2 = \frac{\partial \langle C_1 | \hat{H} | C_2 \rangle}{\partial \mathbf{q}} \quad (4)$$

\mathbf{x}_1 is the gradient difference vector, and \mathbf{x}_2 is the interstate coupling vector. Both vectors can be obtained routinely at the complete active space self-consistent field (CASSCF) level of theory.¹¹ E_i is the adiabatic energy of state i , H is the electronic part of the Hamiltonian, and C_1 and C_2 are the CI eigenvectors of the MC-SCF problem. The resulting projector is

$$\mathbf{P} = \mathbf{I} - \hat{\mathbf{x}}_1 \hat{\mathbf{x}}_1^T - \hat{\mathbf{x}}_2 \hat{\mathbf{x}}_2^T \quad (5)$$

We follow the usual notation, where $\hat{\mathbf{x}}$ stands for the normalized vector \mathbf{x} . \mathbf{x}_1 and \mathbf{x}_2 are orthogonalized for the projection. The intersection space gradient \mathbf{g}_{IS} is obtained applying the projector to the gradient of either of the degenerate states (both projections give the same result):

$$\mathbf{g}_{\text{IS}} = \mathbf{P} \frac{\partial E_2}{\partial \mathbf{q}} = \mathbf{P} \frac{\partial E_1}{\partial \mathbf{q}} \quad (6)$$

The main idea behind projection methods is that once the energy degeneracy condition is fulfilled, optimization steps along \mathbf{x}_1 and \mathbf{x}_2 should be avoided because they may cause a loss of the energy degeneracy. This is taken care of (to first order) by construction, since the intersection space gradient of eq 6 is orthogonal to \mathbf{x}_1 and \mathbf{x}_2 .

Projected gradient methods are more efficient than penalty function ones because the projected gradient helps to maintain the energy degeneracy during the optimization. Their practical advantage with respect to Lagrange–Newton methods is that they can be easily implemented into available optimization routines. Here, we focus on the combination of projected gradient algorithms with a Newton–Raphson optimization in redundant coordinates¹² and Broyden–Fletcher–Goldfarb–Shanno (BFGS) update of the Hessian.¹³ One important issue is how the energy degeneracy condition is implemented, and this is the main point of our paper. The first possibility is to work with a composed gradient (CG) \mathbf{g}_{c} of the form^{3b}

$$\mathbf{g}_{\text{c}} = \mathbf{g}_{\text{IS}} + \mathbf{f} \quad (7)$$

where

$$\mathbf{f} = 2\Delta E \hat{\mathbf{x}}_1 \quad (8)$$

In eq 7, \mathbf{g}_{IS} and \mathbf{f} are orthogonal, and \mathbf{g}_{c} only becomes zero when both components are zero, i.e., when the two minimization conditions of eqs 1 and 2 are fulfilled. When the degeneracy is reached, the \mathbf{f} component is zero, and steps along the branching space, which might lift the degeneracy, should be avoided. However, the CG algorithm has the drawback that the gradient is not well suited for the Hessian update, since it is made of components in the branching space and the inter-

section space. The branching space components act on the updated Hessian. In the Newton–Raphson step, this can lead to displacements in the branching space even when \mathbf{f} is zero, lifting the degeneracy.

To circumvent this problem, we have recently introduced a method which uses a composed step (CS) instead of a CG.^{6c} To understand the performance of the different algorithms, it is useful to think of the optimization as a process made of two main phases: in the first phase the energy gap is large, and the approach to the energy degeneracy dominates the optimization. The optimization in the intersection space is carried out in the second phase, once the degeneracy is reached. As we explain more in detail below, in the CS algorithm the Newton–Raphson step is only carried out in the intersection space, and the energy degeneracy condition is approached with a linear step along the gradient difference vector \mathbf{x}_1 . This improves the optimization in the intersection space, but the approach to the intersection space is more efficient in the CG case. For that reason, we proposed a hybrid CG-CS algorithm which starts with the CG method and switches to the CS one when the energy degeneracy is reached.^{6c}

In the present paper, we introduce a new projection based algorithm with a CS where the approach to the seam is improved. The so-called double Newton–Raphson (DNR) algorithm does two Newton–Raphson steps in every optimization cycle. Thus, compared to the CS algorithm the linear step along \mathbf{x}_1 is replaced with a quadratic step. The three methods (CG, hybrid CG-CS, and DNR) are compared for several cases, and the results show that the optimization is improved with a hybrid DNR-CS algorithm.

Theoretical Basis. The CS Algorithm and Its Implementation. The main idea of the CS algorithm is to carry out displacements composed of two independent steps, each one following the conditions of eqs 1 and 2. We follow the derivation of ref 6c, which is related to the derivations presented in refs 5c and 6b. To reach the energy degeneracy from a starting point \mathbf{q}_0 , the energy difference is expanded in a Taylor series to first order:

$$\Delta E(\mathbf{q}_0 + \Delta \mathbf{q}^{\text{BS}}) = \Delta E^0 + \Delta \mathbf{q}^{\text{T}}_{\text{BS}} \mathbf{x}_1 \quad (9)$$

where ΔE^0 is the energy gap at \mathbf{q}_0 . The displacement that leads to energy degeneracy is parallel to \mathbf{x}_1 and is called the branching space displacement:

$$\Delta \mathbf{q}_{\text{BS}} = -\frac{\Delta E^0}{\delta \kappa^0} \hat{\mathbf{x}}_1 \quad (10)$$

$\delta \kappa^0$ is the length of \mathbf{x}_1 at \mathbf{q}_0 . The energy minimization in the intersection space is achieved with a Newton–Raphson procedure using the intersection space gradient:

$$\Delta \mathbf{q}_{\text{IS}} = -(\tilde{\mathbf{H}}_{\text{IS}})^{-1} \mathbf{g}_{\text{IS}} \quad (11)$$

In eq 11, $\tilde{\mathbf{H}}_{\text{IS}}$ is derived from the so-called intersection space Hessian, \mathbf{H}_{IS} . The intersection space Hessian is the second derivative matrix of the seam energy.¹⁴ Here, it is obtained from \mathbf{g}_{IS} with the BFGS update (see details in the Implementation section). The optimization step is the sum of the intersection and branching space steps:

$$\Delta \mathbf{q} = \Delta \mathbf{q}_{\text{BS}} + \Delta \mathbf{q}_{\text{IS}} \quad (12)$$

Once the degeneracy is reached, the convergence with the CS algorithm is improved with respect to the CG one. However the CS has a poor performance when the seam is approached because the steps are forced to go along the \mathbf{x}_1 direction. As a result, the initial part of the optimization, which is dominated

by the approach to the seam, reaches the degeneracy in more steps and leads to regions of the seam with higher energy. To solve this problem, in our previous work we implemented a hybrid algorithm that combines the best of the two algorithms: The optimization starts with the CG algorithm until the energy degeneracy is reached, i.e., when the energy gap between the two states falls below a threshold of 0.005 hartree. After the threshold, the optimization switches to the CS procedure to optimize the energy in the intersection space. We refer to this implementation as the hybrid CG-CS one.

The DNR Algorithm. The main motivation of the DNR algorithm is to improve the approach to the seam. The idea to do this is borrowed from the CG algorithm, where the energy degeneracy condition (eq 1) is reached *via* the gradient component f (eq 8). In its turn, f is derived from the condition of minimizing $(\Delta E)^2$. Thus, we can express the DNR algorithm as the minimization of two functions, E_{IS} and $(\Delta E)^2$. Each function is optimized with a Newton–Raphson step, and the optimization step is the sum of the two. Therefore, the working equations for the intersection space step and the total optimization step are the same ones as in the CS case (eqs 11 and 12). The branching space step is given by

$$\Delta \mathbf{q}_{\text{BS}} = (\mathbf{H}_{\text{BS}})^{-1} \mathbf{g}_{\text{BS}} \quad (13)$$

and \mathbf{g}_{BS} is equal to f in eq 8:

$$\mathbf{g}_{\text{BS}} = \frac{1}{\delta \kappa^0} \frac{\partial (\Delta E^2)}{\partial \mathbf{q}} = 2\Delta E \hat{\mathbf{x}}_1 \quad (14)$$

Similar to the intersection space Hessian, the branching space Hessian \mathbf{H}_{BS} is obtained from \mathbf{g}_{BS} with the BGFS update. Strictly speaking, the gradient for minimization of $(\Delta E)^2$ is $2\Delta E \hat{\mathbf{x}}_1$. However, in eq 14 we follow the original derivation of the CG algorithm, and we divide the gradient by the length of $\hat{\mathbf{x}}_1$, which greatly improves the convergence.

Implementation. The DNR algorithm has been implemented in the Gaussian Development Version program.¹⁵ Several practical issues deserve comment. The first one is related with the use of redundant coordinates for optimization, which requires a transformation of the gradient from Cartesian to redundant coordinates. If the transformation to redundant coordinates is done on \mathbf{g}_{IS} , after the projection step (eq 6), the orthogonality between the gradient vectors \mathbf{g}_{IS} and \mathbf{x}_1 is lost during the transformation. Thus, the transformation of a gradient from Cartesian to redundant coordinates (\mathbf{x}^{cart} to \mathbf{x}^{red}) is given by eq 15:^{12,16}

$$\mathbf{x}^{\text{red}} = \mathbf{G}^{-1} \mathbf{B} \mathbf{x}^{\text{cart}} \quad (15)$$

where \mathbf{B} is the Wilson matrix¹⁷ and \mathbf{G}^{-1} is the generalized inverse of $\mathbf{G} = \mathbf{B} \mathbf{B}^T$. Before the transformation, $\mathbf{g}_{\text{IS}}^{\text{cart}}$ and $\mathbf{x}_1^{\text{cart}}$ (both in Cartesian) are orthogonal. After the transformation to redundant coordinates, the scalar product is

$$(\mathbf{g}_{\text{IS}}^{\text{red}})^T \mathbf{x}_1^{\text{red}} = (\mathbf{g}_{\text{IS}}^{\text{cart}})^T \mathbf{B}^T (\mathbf{G}^{-1})^T \mathbf{G}^{-1} \mathbf{B} \mathbf{x}_1^{\text{cart}} \quad (16)$$

For the orthogonality to be retained in redundant coordinates, the product $\mathbf{B}^T (\mathbf{G}^{-1})^T \mathbf{G}^{-1} \mathbf{B}$ should be the unity matrix, which is not the case. The loss of orthogonality of \mathbf{g}_{IS} with respect to the branching space vectors is similar to what happens when geometry constraints are applied to the optimization gradient in the CG case.¹⁸ Similar to this case, it is better to transform \mathbf{g}_{IS} , \mathbf{x}_1 , and \mathbf{x}_2 to redundant coordinates before the projection and do the projection in redundant coordinates. This procedure, which is different from the current implementation of the CG

algorithm in Gaussian,¹⁹ has been adopted here for the three investigated algorithms. The back transformation from redundant to Cartesian coordinates does not suffer from this problem because there one wants to maintain orthogonality between the $\Delta \mathbf{q}_{\text{IS}}$ displacement and the \mathbf{x}_1 and \mathbf{x}_2 gradient vectors. In this case, the back transformation for the gradient vectors is

$$\mathbf{x}^{\text{cart}} = \mathbf{B}^T \mathbf{x}^{\text{red}} \quad (17)$$

In its turn, the back transformation for the intersection space displacement can be approximated as^{12,16}

$$\Delta \mathbf{q}^{\text{cart}} = \mathbf{B}^T \mathbf{G}^{-1} \Delta \mathbf{q}^{\text{red}} \quad (18)$$

Thus, the scalar products between $\Delta \mathbf{q}_{\text{IS}}$ and \mathbf{x}_1 and \mathbf{x}_2 , respectively, are not affected by the transformation, and the orthogonality is retained.

The second issue is related with the construction of $\tilde{\mathbf{H}}_{\text{IS}}$ (eq 11) from \mathbf{H}_{IS} . Thus, \mathbf{H}_{IS} can be defined as the derivative of the intersection space gradient:

$$\mathbf{H}_{\text{IS}} = \frac{\partial}{\partial \mathbf{q}} \mathbf{g}_{\text{IS}} \quad (19)$$

\mathbf{H}_{IS} is obtained from \mathbf{g}_{IS} following the BFGS update.^{6c} To avoid $\Delta \mathbf{q}_{\text{IS}}$ components along \mathbf{x}_1 and \mathbf{x}_2 , the intersection space Hessian should have zero eigenvalues along these directions. However, this is not necessarily the case because the directions of these vectors change during the optimization, and \mathbf{H}_{IS} is obtained from an update. This can be corrected multiplying \mathbf{H}_{IS} from the left and right by \mathbf{P} . The resulting matrix has two zero eigenvalues corresponding to the directions of \mathbf{x}_1 and \mathbf{x}_2 . To avoid problems with the inversion in the Newton–Raphson step (eq 11), these eigenvalues are increased artificially to a high value, following the idea of ref 12. Thus, the final matrix used for the Newton–Raphson step is

$$\tilde{\mathbf{H}}_{\text{IS}} = \mathbf{P} \mathbf{H}_{\text{IS}} \mathbf{P} + (\mathbf{I} - \mathbf{P}) \mathbf{A} (\mathbf{I} - \mathbf{P}) \quad (20)$$

\mathbf{A} is a diagonal matrix whose elements are set to a large constant (5000 hartree·bohr⁻² in the present case). Note that before the step in redundant coordinates is calculated (eq 11), $\tilde{\mathbf{H}}_{\text{IS}}$ from eq 20 is further modified by the optimization routine implemented in Gaussian; i.e., displacements in the redundant part of the coordinate space are avoided as indicated in ref 12. The construction of the intersection space step (eq 11) is similar to what is proposed in eq 13 of ref 5c, although the Hessian is different. In ref 5c, the Newton–Raphson procedure is carried out with the so-called reduced Hessian matrix, which has dimension $N - 2$; here, we use redundant coordinates, and instead of reducing the dimension of the matrix, we find it more convenient to use $\tilde{\mathbf{H}}_{\text{IS}}$ and treat the zero eigenvalues along \mathbf{x}_1 and \mathbf{x}_2 analogously to those along the redundant part of the coordinate space.

The branching space Hessian has also some characteristics that have to be treated with care. First, in any molecule there are many coordinates that do not affect the energy difference. This results in a large number of near zero eigenvalues in \mathbf{H}_{BS} , which in turn can cause problematic $\Delta \mathbf{q}_{\text{BS}}$ steps, namely displacements along coordinates that do not affect the energy gap. To avoid this problem, we have followed the idea of eq 20 and increased artificially all eigenvalues of \mathbf{H}_{BS} smaller than a threshold of 2×10^{-4} hartree·bohr⁻². Another problem is caused by the tendency of the electronic states to mix near the degeneracy. The mixture of the states interchanges the GD and IC vectors \mathbf{x}_1 and \mathbf{x}_2 , causing arbitrary changes in the direction

of \mathbf{x}_1 . These changes affect \mathbf{g}_{BS} (see eq 14), and more importantly, they affect \mathbf{H}_{BS} through the update formula. In turn, this results in poor $\Delta\mathbf{q}_{BS}$ steps and a loss of the degeneracy near the seam. Moreover, this effect extends to further optimization steps because it affects \mathbf{H}_{BS} . A way to mitigate this problem is to switch from the DNR to the CS procedure, which is equivalent to changing from a quadratic to a linear branching space optimization step. We have followed a practical approach, based on energy criteria, to detect this problem and carry out the switch. Thus, the change comes into effect when there is a sudden rise in the energy gap near the seam during the optimization, i.e., when the energy gap lies below a threshold of 0.005 hartree, and it increases by 0.010 hartree or more from one step to the next one. We refer to this as the hybrid DNR-CS implementation.

The algorithms have been combined with the usual optimization features in Gaussian.¹⁹ The initial Hessian for \mathbf{H}_{BS} and \mathbf{H}_{IS} is the parametrized, diagonal Hessian in redundant coordinates used for default optimizations, which gives satisfactory results. The convergence is checked against the forces in \mathbf{g}_{IS} and the total displacement $\Delta\mathbf{q}$.

COMPUTATIONAL DETAILS

The three algorithms have been tested on a test set of 11 cases. The structures are shown in Figure 1, and the Cartesian coordinates

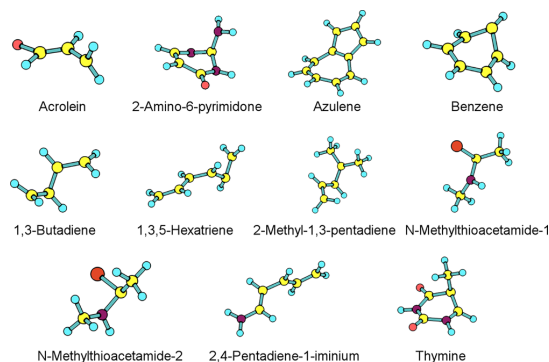


Figure 1. MECI test set used in this work.

are given in the Supporting Information. Four molecules (azulene, benzene, butadiene, and the penta-2,4-dien-1-iminium cation) were previously used in a test set for the comparison of penalty function, projection-based, and Lagrange–Newton MECI optimization algorithms;¹⁰ our test set also includes acrolein and hexatriene, a nucleobase (thymine), and the guanine analogue 2-amino-6-pyrimidone. We also have included three more challenging cases, a floppy butadiene derivative with two additional methyl groups (4-methyl-1,3-pentadiene) and two local MECI minima of *N*-methylthioacetamide which could not be fully optimized in a preceding study with the CG algorithm.²⁰ Most optimizations are started near the excited state minimum, releasing any symmetry constraints. In the cases where several local MECI minima are known on the seam, the molecule has been distorted to drive the optimization toward the global minimum. The coordinates of the starting points are also included in the Supporting Information.

The calculations have been carried out at the state-averaged CASSCF/6-31G** level of theory, and the active spaces are detailed in the Supporting Information. In all optimizations, except for azulene, the gradients include the coupled-perturbed

multiconfiguration self-consistent correction,^{11b} which is only available for active spaces up to eight orbitals. The active space for azulene has 10 active orbitals, and in this case we have used the approximate gradients without the correction.

RESULTS AND DISCUSSION

The results of the MECI searches with the three algorithms are presented in Table 1. We start discussing two representative

Table 1. Results of MECI Searches with the CG, CG-CS, and DNR Algorithms, Including the Distance from the Starting Point to the MECI, the Number of Optimization Cycles, and the Energy Gap at the Optimized Point

test molecule	distance [Å] ^a	method	cycles	ΔE [au] ^b
acrolein	1.70	CG	100 ^c	
		CG-CS	49	0.0000154
		DNR-CS	31	0.0000002
2-amino-6-pyrimidone	1.50	CG	15	0.0000963
		CG-CS	15	0.0000102
		DNR-CS	18	0.0000029
azulene	1.41	CG	15	0.0001397
		CG-CS	16	0.0000465
		DNR-CS	21 (48) ^d	0.0000532
benzene	1.51	CG	21	0.0000331
		CG-CS	21	0.0000002
		DNR-CS	14	0.0000106
1,3-butadiene	2.27 (2.56) ^d	CG	35	0.0001370
		CG-CS	35	0.0000002
		DNR-CS	33 (35) ^e	0.0000001
1,3,5-hexatriene	2.64 (4.21) ^f	CG	33	0.0001113
		CG-CS	29	0.0000003
		DNR-CS	29 (46) ^e	0.0000026
4-methyl-1,3-pentadiene	2.49	CG	40	0.0000705
		CG-CS	37	0.0000002
		DNR-CS	26	0.0000014
<i>N</i> -methylthioacetamide-1 ^g	2.23	CG	100 ^c	
		CG-CS	20	0.0000794
		DNR-CS	20	0.0000175
<i>N</i> -methylthioacetamide-2 ^h	2.36	CG	24	0.0001237
		CG-CS	15	0.0000004
		DNR-CS	17	0.0000078
2,4-pentadiene-1-iminium	2.97	CG	49	0.0000218
		CG-CS	66	0.0000025
		DNR-CS	28	0.0000027
thymine	2.03	CG	15	0.0000886
		CG-CS	15	0.0000006
		DNR-CS	15	0.0000097
average	2.10	CG	41	0.0000913
		CG-CS	29	0.0000142
		DNR-CS	23	0.0000099

^aDistance in Å from the starting point to the converged MECI geometry, calculated in Cartesian coordinates. ^bEnergy difference between the ground and excited states at the end of the optimization. ^cNo convergence reached after the maximum number of 100 optimization steps. ^dIn parentheses, distance to the local MECI obtained in the CG and CG-CS optimizations, see text. ^eIn parentheses, number of steps with the pure DNR algorithm. ^fIn parentheses, distance to the local MECI obtained in the CG optimizations, see text. ^gCI-A1 in ref 20. ^hCI-A2 in ref 20.

cases, for which the energy profiles during the optimizations are shown in Figures 2 and 3. In these plots, the energies of S_1

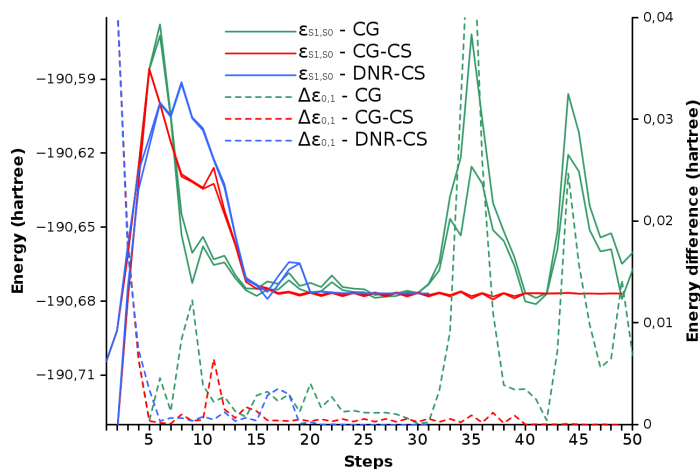


Figure 2. Course of MECI searches with the CG, CG-CS, and DNR-CS algorithms for acrolein (green, red, and blue lines, respectively). Full lines, S_1 and S_0 energies (left y axis); hashed lines, S_1-S_0 energy difference (right y axis). Energies in hartree.

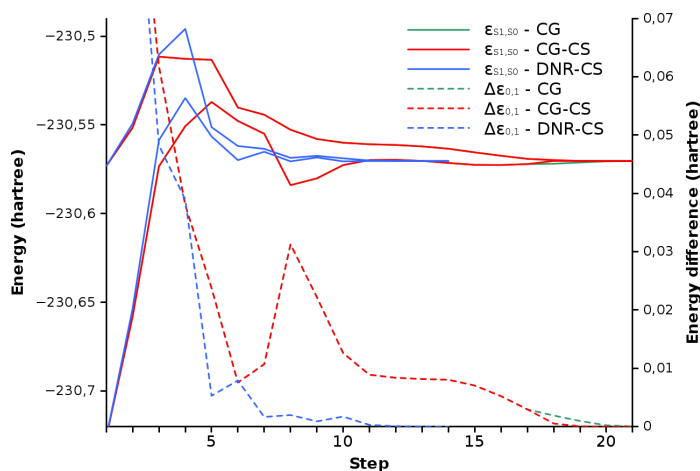


Figure 3. Course of MECI searches with the CG, CG-CS, and DNR-CS algorithms for benzene (green, red, and blue lines, respectively). Full lines, S_1 and S_0 energies (left y axis); hashed lines, S_1-S_0 energy difference (right y axis). Energies in hartree.

and S_0 are presented with full lines, and the energy gap during the optimization with hashed lines (scales on the right and left y axes, respectively). Note that the first phase of the optimization is always identical for the CG and CG-CS algorithms by construction.

The first example (Figure 2) is the optimization of the conical intersection of acrolein. This case exemplifies the loss of degeneracy with the CG algorithm because of the incorrect Hessian update (green curves). In Figure 2, we plot the first 50 steps of the optimization. In the CG case, the degeneracy is reached but lost again in steps 32 and 43 of the run (see the hashed green line, representing the S_1-S_0 energy difference). The rest of the optimization follows a similar course (not shown in Figure 2), and convergence is not reached after the maximum number of 100 optimization steps. In contrast, the CG-CS and DNR algorithms (red and blue curves, respectively) converge after 49 and 31 steps, respectively (see also Table 1). The second example is benzene (Figure 3), where the CG and CG-CS algorithms have a very similar course and

converge in 21 steps (green and red curves, respectively; the two curves are superimposed during most of the run, and the green curve is barely visible). In its turn, the DNR-CS algorithm converges in only 16 steps. In this case, the approach to the seam is more efficient. Thus, the three algorithms approach the seam in a similar number of steps, and the optimizations reach an energy gap of less than 0.01 hartree after 6 steps. However, the DNR-CS algorithm reaches the seam with a smaller absolute energy, and the MECI is reached in a smaller number of total steps.

In Figure 4a and b, we illustrate the effect of state mixing near the seam on optimizations with the DNR algorithm (azulene MECI optimization). In Figure 4a, we compare the optimizations with the pure DNR algorithm and the hybrid DNR-CS implementation (blue and red curves, respectively). In the DNR case, the seam is reached after nine steps, but the degeneracy is lost and recovered repeatedly, as shown by the oscillations of the energy difference (blue hashed line). The oscillations toward and away from the seam are due to repeated changes in the direction of \mathbf{x}_1 ,

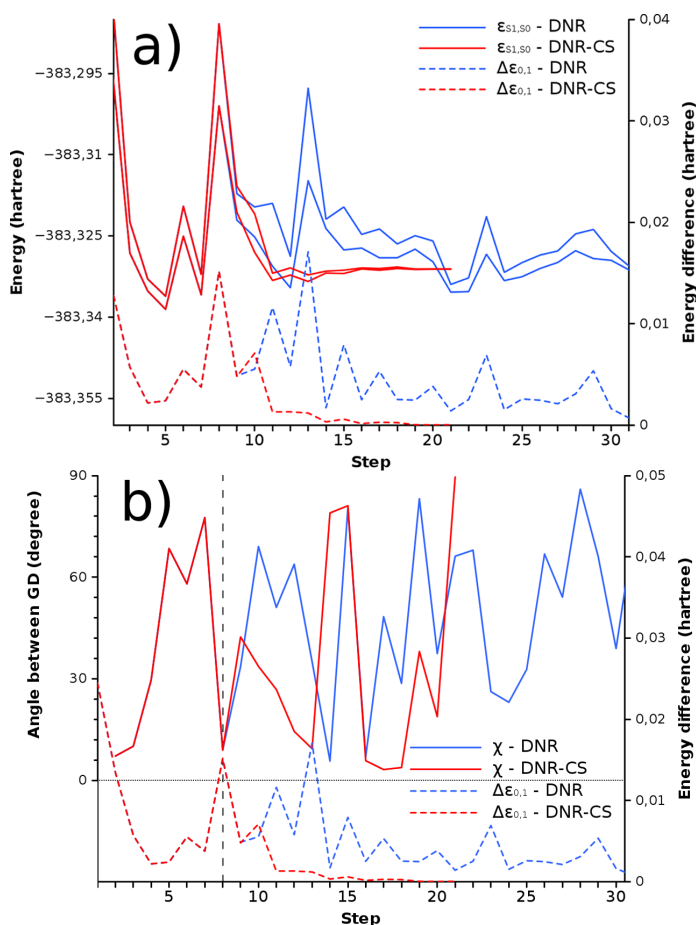


Figure 4. Course of MECI searches with the DNR algorithms for azulene. Blue lines, pure DNR algorithm; red lines, hybrid DNR-CS implementation. (a) Energies and energy difference. Full lines, S_1 and S_0 energies (left y axis); hashed lines, S_1 – S_0 energy difference (right y axis). (b) Angle χ between \mathbf{x}_1 in two consecutive steps (left y axis) and S_1 – S_0 energy difference (right y axis). Energies in hartree.

due to the mixing of the states near the seam (see the discussion of the previous section). This is shown in Figure 4b, where we show the evolution of the angle χ , formed by \mathbf{x}_1 in two consecutive steps. Large values of this angle correspond to large changes in the direction of \mathbf{x}_1 . This occurs, for example, in step 7 of the DNR optimization and leads to a sudden increase of the energy difference in the following step 8. The oscillations are avoided in the DNR-CS implementation, switching to the CS algorithm when the first increase in the energy gap near the seam is detected (step 9 in this case). This reduces the number of optimization steps from 48 to 21. Note that the changes in the direction of \mathbf{x}_1 become irrelevant when the energy gap is very small, because the branching space steps are multiplied by the energy difference (eqs 13 and 14). The case of hexatriene is similar to that of azulene, since the pure DNR algorithm requires 46 steps to reach the MECI and the hybrid DNR-CS implementation needs only 29 steps. The switch to the CS algorithm has also entered into function in the butadiene case, but here the improvement in the number of steps (33 instead of 35 with the pure DNR algorithm; the change from the DNR to the CS step takes place after step 12) is less significant.

Next, we turn our attention to two cases where the three algorithms lead to different local minima on the seam. This is the case for the floppy molecules butadiene (Figure 5) and hexatriene (Figure 6). In both cases, the DNR-CS algorithm finds the global MECI minimum. First, we consider butadiene. Butadiene has several local MECI minima.^{14,21} The global minimum of the intersection space has a *s-transoid* geometry where the C_1 – C_2 – C_3 – C_4 dihedral angle φ_1 is 118.5° , and one of the methyl groups is rotated by 106° (value of the H_5 – C_1 – C_2 – C_3 angle φ_2 ; Figure 5). The MECI searches start at a *transoid* structure ($\varphi_1 = 180^\circ$) where the two double bonds are twisted from planarity by 90° ($\varphi_2 = 90^\circ$). The hybrid DNR-CS algorithm finds the global minimum in 33 steps, whereas the CG-CS and CG algorithms find a different local minimum, which also has a *transoid* conformation ($\varphi_1 = 113.9^\circ$) but a methylene twist angle $\varphi_2 = 53^\circ$. The local minimum is 0.27 eV higher in energy and has not been described previously. In Figure 5, we plot the changes in φ_2 and the S_1 – S_0 energy difference during the optimizations to illustrate how the DNR-CS and CG-CS algorithms approach the seam. In the DNR-CS case (blue curves), the algorithm finds the seam after seven

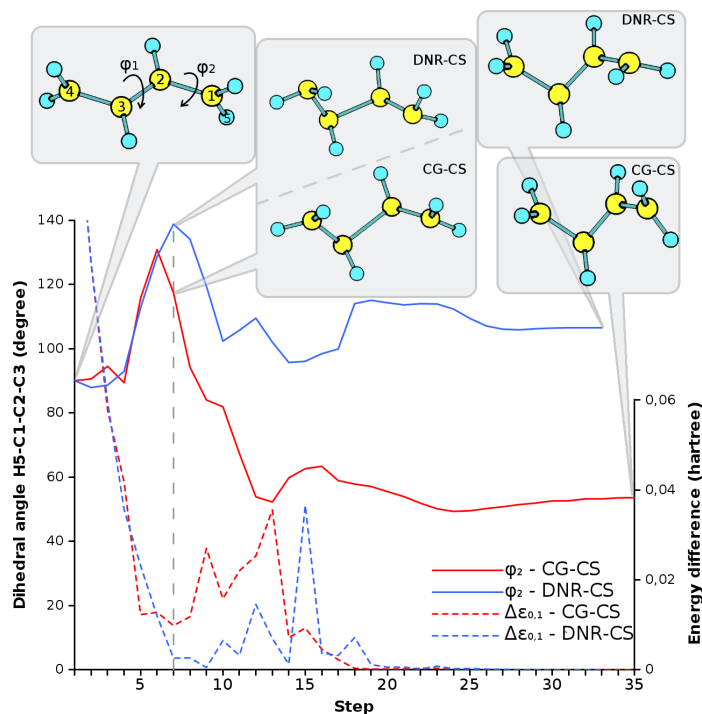


Figure 5. Course of MECI searches with the CG-CS and DNR-CS algorithms for butadiene, leading to different local MECI minima (blue and red lines, respectively). Full lines: H₅-C₁-C₂-C₃ dihedral angle φ_2 . Dashed lines: S₁-S₀ energy difference.

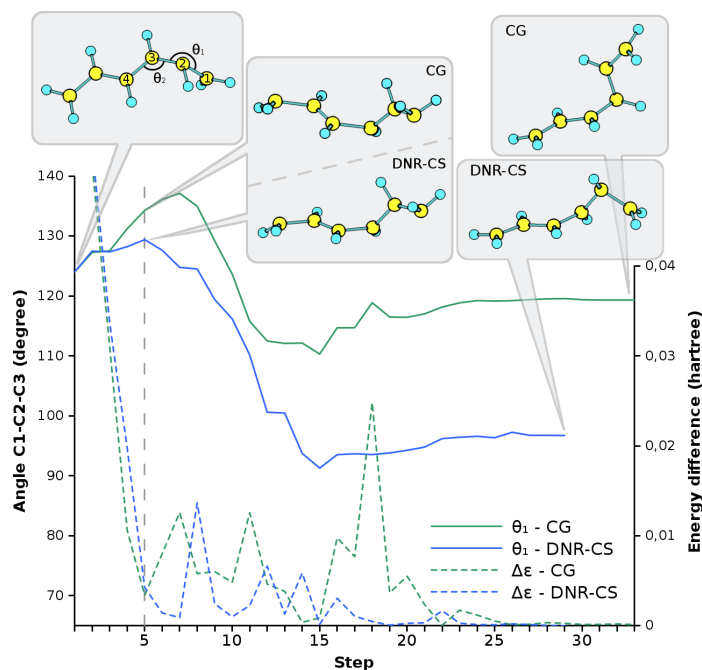


Figure 6. Course of MECI searches with the CG and DNR-CS algorithms for hexadiene, leading to different local MECI minima (green and blue lines, respectively). Full lines: C₁-C₂-C₃ bending angle θ_2 . Dashed lines: S₁-S₀ energy difference.

steps, at an angle φ_2 of approximately 130° , and the value of φ_2 decreases in a few more steps until it finds its approximate final value. In contrast to this, the CG and CG-CS (red curves) need more steps to reach the seam and do it at a structure where φ_2 is approximately 60° (step 18).

For hexatriene (Figure 6), the global MECI is characterized by a “kink” at C_2 (C_1 – C_2 – C_3 bending angle $\theta_1 = 96.7^\circ$), and there is a local MECI with a “kink” at C_3 (C_2 – C_3 – C_4 bending angle $\theta_2 = 98.6^\circ$) that lies 0.03 eV higher.²² The MECI search starts at a structure with a twisted C_1 – C_2 – C_3 moiety (see Figure 6), and the structure found by the DNR-CS and CG-CS algorithms is the global MECI. In contrast to this, the CG algorithm leads to the local minimum on the seam. In this case, the CG and CG-CS algorithms find the seam at a structure with long C–C bonds (see the structures at step 5 in Figure 6). However, the energy optimization with the CG algorithm leads to the local MECI with the kink localized on C_3 (green curves), while that with the CG-CS one finds the global minimum. In comparison, the structure where the DNR-CS algorithm hits the seam has shorter bonds and lower energy, and the energy optimization leads to the global minimum (blue curves).

Overall, the hybrid DNR-CS is the most efficient of the tested algorithms. It reaches the MECI in approximately 15% less steps than the hybrid CG-CS one and 30% less steps than the CG algorithm. The CG-CS and DNR-CS algorithms also give a better convergence with respect to the energy degeneracy. In the CG case, the gradient \mathbf{g} , near the MECI is dominated by \mathbf{g}_{IS} (eq 7), and the convergence with respect to the energy degeneracy is not strict. However in the CG-CS and DNR-CS algorithms, the energy degeneracy convergence is controlled through the convergence of the displacement size, and this results in smaller energy gaps. More insight into the performance of the different algorithms can be obtained by examining the number of steps required to reach the degeneracy and the energy at the point where the seam is reached. Thus, Table 2 presents the number of steps required to reach a degeneracy threshold of 0.005 and 0.001 hartree, together with the energy of S_1 relative to the MECI at those points. This gives an idea of how close the optimization is to the MECI when it reaches the seam. On average, the DNR-CS algorithm needs a few less steps than the CG and CG-CS algorithms to reach an energy difference smaller than 0.005 hartree (seven steps against 10, respectively). The smaller energy gap of 0.001 hartree is reached in the same number of steps with the DNR-CS and CG-CS algorithms (10 in both cases), but the DNR-CS algorithm reaches the degeneracy closer to the MECI: on average the point of 0.001 hartree degeneracy is reached 0.019 hartree above the MECI with the DNR algorithm, while the CG-CS algorithm reaches such a degeneracy 0.030 hartree above the MECI. Overall, these data illustrate the better efficiency of the hybrid DNR-CS implementation. At the same time, the optimization details show that the course of the optimization can differ widely from case to case: thus, in several cases the 0.001 degeneracy threshold is reached very close to the MECI (for example, for benzene, azulene, or 2-amino-6-pyrimidone), whereas in other cases the seam is reached well above the MECI, such as in the acrolein, hexatriene, and butadiene cases. Moreover, the course of the optimizations also depends on the starting point. Here, most optimizations have been started near the excited state minimum, which usually lies far away from the intersection, to reproduce applications of the algorithms where the MECI structure is not known. In this case, the projected intersection space gradient \mathbf{g}_{IS} at the S_1 minimum is zero, and the first optimization step is defined

Table 2. Number of Steps Required to Reach Degeneracy Thresholds of 0.005 au and 0.001 au and Energy of S_1 at Those Points, Relative to the MECI, for the 11 Test Cases with the CG, CG-CS, and DNR-CS Algorithms

test molecule	method	threshold 0.005 au		threshold 0.001 au	
		steps ^a	E_{rel}^b [au]	steps ^a	E_{rel}^b [au]
acrolein	CG	5	0.0911	5	0.0911
	CG-CS	5	0.0911	5	0.0911
	DNR-CS	5	0.0631	6	0.0773
2-amino-6-pyrimidone	CG	5	−0.0064	6	−0.0038
	CG-CS	5	−0.0064	7	−0.0026
	DNR-CS	9	−0.0071	11	−0.0005
azulene	CG	7	0.0012	11	−0.0008
	CG-CS	7	0.0011	8	0.0005
	DNR-CS	4	0.0019	14	0.0004
benzene	CG	17	−0.0012	19	−0.0001
	CG-CS	17	0.0012	18	0.0006
	DNR-CS	7	0.0069	9	0.0029
1,3-butadiene	CG	16	−0.0047	18	−0.0007
	CG-CS	16	−0.0048	18	−0.0008
	DNR-CS	7	−0.1165	9	−0.0584
1,3,5-hexatriene	CG	5	−0.0994	14	−0.0131
	CG-CS	5	−0.1044	6	−0.0751
	DNR-CS	5	−0.0684	7	−0.0501
4-methyl-1,3-pentadiene	CG	12	−0.0203	24	−0.0005
	CG-CS	12	−0.0204	14	−0.0075
	DNR-CS	8	−0.0518	14	−0.0136
N-methylthioacetamide-1 ^f	CG	4	−0.0067	31	−0.0011
	CG-CS	4	−0.0067	6	−0.003
	DNR-CS	5	−0.0243	13	−0.0001
N-methylthioacetamide-2 ^d	CG	5	−0.0143	5	−0.0143
	CG-CS	5	−0.0144	5	−0.0144
	DNR-CS	5	−0.0162	5	−0.0005
2,4-pentadiene-1-iminium	CG	15	−0.1698	45	−0.0003
	CG-CS	15	−0.1699	19	−0.1354
	DNR-CS	13	−0.0631	17	−0.0094
thymine	CG	7	−0.0056	12	−0.0002
	CG-CS	7	−0.0056	8	−0.0014
	DNR-CS	7	−0.0006	8	−0.0002
average	CG	9	0.0383	17	0.0115
	CG-CS	9	0.0387	10	0.0302
	DNR-CS	7	0.0381	10	0.0194

^aOptimization steps required to reach energy degeneracy within the given threshold. ^b S_1 energy at those points, relative to the MECI. ^cCI-A1 in ref 20. ^dCI-A2 in ref 20.

solely by the gradient difference component (eqs 8 and 14). However the optimization leaves the S_1 minimum region quickly, and \mathbf{g}_{IS} increases. Therefore, overall our starting point choice should not bias the optimization course in favor of any of the three algorithms.

CONCLUSIONS

Our comparison of the CG, CG-CS, and DNR-CS algorithms shows that the newly implemented DNR-CS algorithm reduces the number of steps in MECI optimizations substantially. In this algorithm, the optimization step is the sum of an intersection space step that minimizes the energy, and a branching space step that leads to the degeneracy. A separate Hessian is updated for every step, with negligible additional computational cost compared to the energy and gradient calculations. Similar to

the CG-CS case, the use of the intersection space Hessian in the DNR algorithm avoids losing the degeneracy during the optimization, which is the main drawback of the CG algorithm. On the other hand, the branching space Hessian improves the approach to the seam compared to the CG and CG-CS cases, by taking second order degeneracy lifting effects into account. Such effects change the direction of the gradient difference vector \mathbf{x}_1 along the surface, since a second order degeneracy lifting component at one point of the surface can contribute at a different point to lift the degeneracy at first order.²³ The branching space Hessian captures these effects.

Finally, the DNR-CS algorithm can be adapted to the transition state and minimum energy path optimizations in the seam described in ref 14. It can be also adapted to a hybrid QM/MM formalism to optimize MECI structures in extended or biological systems and in the condensed phase. This will be the subject of future work.

■ ASSOCIATED CONTENT

Supporting Information

Active spaces of the CASSCF calculations and Cartesian coordinates of the MECI. This material is available free of charge via the Internet at <http://pubs.acs.org>.

■ AUTHOR INFORMATION

Corresponding Author

*E-mail: lluis.blancafort@udg.edu.

Notes

The authors declare no competing financial interests.

■ ACKNOWLEDGMENTS

This work has been supported by grants CTQ2008-06696 and CTQ2011-26573 from the Spanish Ministerio de Ciencia e Innovación (MICINN) and Ministerio de Economía y Competitividad (MINECO), respectively, SGR0528 from the Catalan Agència de Gestió d'Ajuts Universitaris i de Recerca (AGAUR), UNGI08-4E-003 from MICINN and the European Fund for Regional Development, and the Xarxa de Referència en Química Teòrica i Computacional de Catalunya from AGAUR. S.R.-B. thanks the MICINN for grant BES-2009-029177.

■ REFERENCES

- (1) Klessinger, M.; Michl, J. *Excited States and Photochemistry of Organic Molecules*; VCH Publishers, Inc.: New York, 1995.
- (2) Bernardi, F.; Olivucci, M.; Robb, M. A. *Chem. Soc. Rev.* **1996**, *25*, 321.
- (3) Yarkony, D. R. *Rev. Mod. Phys.* **1996**, *68*, 985.
- (4) Domcke, W.; Yarkony, D. R.; Köppel, H. *Conical Intersections: Electronic Structure, Dynamics & Spectroscopy*; World Scientific: Singapore, 2004.
- (5) Domcke, W.; Yarkony, D. R.; Köppel, H. *Conical Intersections: Theory, Computation and Experiment*; World Scientific: Singapore, 2011.
- (6) Boggio-Pasqua, M.; Burmeister, C. F.; Robb, M. A.; Groenhof, G. *Phys. Chem. Chem. Phys.* **2012**, *14*, 7912.
- (7) González, L.; Escudero, D.; Serrano-Andrés, L. *ChemPhysChem* **2012**, *13*, 28.
- (8) Blancafort, L.; Ogliaro, F.; Olivucci, M.; Robb, M. A.; Bearpark, M. J.; Sinicropi, A. Computational investigation of photochemical reaction mechanisms. In *Computational Methods in Photochemistry*; Kutateladze, A. G., Ed.; Taylor & Francis: Boca Raton, FL, 2005; Vol. 13, p 31.
- (9) (a) Manaa, M. R.; Yarkony, D. R. *J. Chem. Phys.* **1993**, *99*, 5251. (b) Bearpark, M. J.; Robb, M. A.; Schlegel, H. B. *Chem. Phys. Lett.* **1994**, *223*, 269. (c) Anglada, J. M.; Bofill, J. M. *J. Comput. Chem.* **1997**, *18*, 992.
- (6) (a) Yarkony, D. R. *J. Phys. Chem. A* **2004**, *108*, 3200. (b) De Vico, L.; Olivucci, M.; Lindh, R. *J. Chem. Theory Comput.* **2005**, *1*, 1029. (c) Sicilia, F.; Blancafort, L.; Bearpark, M. J.; Robb, M. A. *J. Chem. Theory Comput.* **2008**, *4*, 257.
- (7) (a) Toniolo, A.; Ben-Nun, M.; Martinez, T. J. *J. Phys. Chem. A* **2002**, *106*, 4679. (b) Maeda, S.; Ohno, K.; Morokuma, K. *J. Chem. Theory Comput.* **2010**, *6*, 1538. (c) Quapp, W.; Bofill, J. M.; Caballero, M. *Chem. Phys. Lett.* **2012**, *541*, 122.
- (8) (a) Muñoz Losa, A.; Ben-Nun, M. E.; Galván, I. F.; Aguilar, M. A. *Chem. Phys. Lett.* **2007**, *443*, 76. (b) Bearpark, M. J.; Larkin, S. M.; Vreven, T. *J. Phys. Chem. A* **2008**, *112*, 7286. (c) Mori, T.; Nakano, K.; Kato, S. *J. Chem. Phys.* **2010**, *133*, 064107. (d) Cui, G.; Yang, W. *J. Chem. Phys.* **2011**, *134*, 204115.
- (9) Fletcher, R. *Practical Methods of Optimization*; Wiley & Sons: New York, 1981; Vol. 2.
- (10) Keal, T. W.; Koslowski, A.; Thiel, W. *Theor. Chem. Acc.* **2007**, *118*, 837.
- (11) (a) Yarkony, D. R. *J. Chem. Phys.* **1990**, *92*, 2457. (b) Yamamoto, N.; Vreven, T.; Robb, M. A.; Frisch, M. J.; Schlegel, H. B. *Chem. Phys. Lett.* **1996**, *250*, 373.
- (12) Peng, C. Y.; Ayala, P. Y.; Schlegel, H. B.; Frisch, M. J. *J. Comput. Chem.* **1996**, *17*, 49.
- (13) Schlegel, H. B. Geometry Optimization: 1. In *Encyclopedia of Computational Chemistry*; Schleyer, P. v. R., Ed.; John Wiley & Sons: Chichester, U.K., 1998; Vol. 2, p 1136.
- (14) Sicilia, F.; Blancafort, L.; Bearpark, M. J.; Robb, M. A. *J. Phys. Chem. A* **2007**, *111*, 2182.
- (15) Frisch, M. J.; Trucks, G. W.; Schlegel, H. B.; Scuseria, G. E.; Robb, M. A.; Cheeseman, J. R.; Scalmani, G.; Barone, V.; Mennucci, B.; Petersson, G. A.; Nakatsuji, H.; Caricato, M.; Li, X.; Hratchian, H. P.; Izmaylov, A. F.; Bloino, J.; Zheng, G.; Sonnenberg, J. L.; Hada, M.; Ehara, M.; Toyota, K.; Fukuda, R.; Hasegawa, J.; Ishida, M.; Nakajima, T.; Honda, Y.; Kitao, O.; Nakai, H.; Vreven, T.; Montgomery, J. A., Jr.; Peralta, J. E.; Ogliaro, F.; Bearpark, M. J.; Heyd, J. J.; Brothers, E.; Kudin, K. N.; Staroverov, V. N.; Keith, T.; Kobayashi, R.; Normand, J.; Raghavachari, K.; Rendell, A.; Burant, J. C.; Iyengar, S. S.; Tomasi, J.; Cossi, M.; Rega, N.; Millam, J. M.; Klene, M.; Knox, J. E.; Cross, J. B.; Bakken, V.; Adamo, C.; Jaramillo, J.; Gomperts, R.; Stratmann, R. E.; Yazyev, O.; Austin, A. J.; Cammi, R.; Pomelli, C.; Ochterski, J. W.; Martin, R. L.; Morokuma, K.; Zakrzewski, G.; Voth, G. A.; Salvador, P.; Dannenberg, J. J.; Dapprich, S.; Parandekar, P. V.; Mayhall, N. J.; Daniels, A. D.; Farkas, O.; Foresman, J. B.; Ortiz, J. V.; Cioslowski, J.; Fox, D. J. *Gaussian Development Version*, revision H.13; Gaussian, Inc.: Wallingford, CT, 2010.
- (16) Pulay, P.; Fogarasi, G. *J. Chem. Phys.* **1992**, *96*, 2856.
- (17) Wilson, E. B., Jr.; Decius, J. C.; Cross, P. C. *Molecular Vibrations*; McGraw-Hill: New York, 1955.
- (18) Bearpark, M. J.; Blancafort, L.; Paterson, M. J. *Mol. Phys.* **2006**, *104*, 1033.
- (19) Frisch, M. J.; Trucks, G. W.; Schlegel, H. B.; Scuseria, G. E.; Robb, M. A.; Cheeseman, J. R.; Scalmani, G.; Barone, V.; Mennucci, B.; Petersson, G. A.; Nakatsuji, H.; Caricato, M.; Li, X.; Hratchian, H. P.; Izmaylov, A. F.; Bloino, J.; Zheng, G.; Sonnenberg, J. L.; Hada, M.; Ehara, M.; Toyota, K.; Fukuda, R.; Hasegawa, J.; Ishida, M.; Nakajima, T.; Honda, Y.; Kitao, O.; Nakai, H.; Vreven, T.; Montgomery, J. A., Jr.; Peralta, J. E.; Ogliaro, F.; Bearpark, M. J.; Heyd, J. J.; Brothers, E.; Kudin, K. N.; Staroverov, V. N.; Keith, T.; Kobayashi, R.; Normand, J.; Raghavachari, K.; Rendell, A.; Burant, J. C.; Iyengar, S. S.; Tomasi, J.; Cossi, M.; Rega, N.; Millam, J. M.; Klene, M.; Knox, J. E.; Cross, J. B.; Bakken, V.; Adamo, C.; Jaramillo, J.; Gomperts, R.; Stratmann, R. E.; Yazyev, O.; Austin, A. J.; Cammi, R.; Pomelli, C.; Ochterski, J. W.; Martin, R. L.; Morokuma, K.; Zakrzewski, G.; Voth, G. A.; Salvador, P.; Dannenberg, J. J.; Dapprich, S.; Daniels, A. D.; Farkas, O.; Foresman, J. B.; Ortiz, J. V.; Cioslowski, J.; Fox, D. J. *Gaussian 09*, Revision C.01; Gaussian, Inc.: Wallingford, CT, 2010.
- (20) Helbing, J.; Bregy, H.; Bredenbeck, J.; Pfister, R.; Hamm, P.; Huber, R.; Wachtveitl, J.; De Vico, L.; Olivucci, M. *J. Am. Chem. Soc.* **2004**, *126*, 8823.

- (21) Olivucci, M.; Ragazos, I. N.; Bernardi, F.; Robb, M. A. *J. Am. Chem. Soc.* **1993**, *115*, 3710.
- (22) Garavelli, M.; Celani, P.; Bernardi, F.; Robb, M. A.; Olivucci, M. *J. Am. Chem. Soc.* **1997**, *119*, 11487.
- (23) Paterson, M. J.; Bearpark, M. J.; Robb, M. A.; Blancafort, L. *J. Chem. Phys.* **2004**, *121*, 11562.

4.2 Conical Intersection Optimization using Composed Steps inside the ONIOM scheme. QM:MM with mechanical embedding and microiterations.

S. Ruiz-Barragán, K. Morokuma, Ll. Blancafort

In preparation

Embargoed until publication

S. Ruiz-Barragán, K. Morokuma, Ll. Blancafort. “Conical Intersection Optimization using Composed Steps inside the ONIOM scheme. QM:MM with mechanical embedding and microiterations”.
Submitted

Conical Intersections (CIs) are fundamental structures for photochemistry and photophysics, where the energy difference between two or more electronic states is zero. These structures can provide rapid ways to decay from excited states to lower states when they are accessible in energy. Therefore, CIs are the principal reason for the ultrafast deactivation of excited states. For this reason, CIs play an important role in photo-processes, and are fundamental to understand them. Several molecules have CIs accessible in energy. Among them, there are many biological systems such as, for example, the DNA nucleobases.

(...)

Chapter 5

Photophysics of fulvene under the non-resonant Stark effect. Shaping the conical intersection seam

S. Ruiz-Barragán, Ll. Blancafort

Faraday Discuss., 163, **2013**, 497-512

PAPER

Photophysics of fulvene under the non-resonant stark effect. Shaping the conical intersection seam

Sergi Ruiz-Barragan and Lluís Blancafort*

Received 20th December 2012, Accepted 17th January 2013

DOI: 10.1039/c3fd20155d

We introduce a mechanistic strategy to control the excited state lifetime of fulvene based on shaping the topography of an extended seam of intersection with the non-resonant dynamic Stark effect. Fulvene has a very short excited state lifetime due to an energetically accessible seam of intersection which lies along the methylene torsion coordinate, and the initial decay occurs at the seam segment around the planar conical intersection structure. We have followed a three-step approach to simulate the control. First, we have calculated the effect of a non-resonant electric field on the potential energy surface at the *ab initio* level, including the field in a self-consistent way. The relative energy of the planar segment of the seam is increased by the non-resonant field. In the second step we simulate the control carrying out MCTDH quantum dynamics propagations under a static non-resonant field to derive the main control mechanisms. At moderately intense fields ($\epsilon \leq 0.03$ a.u.) the decay is faster as compared to the field free case because the vibrational overlap between the excited and ground state vibrational functions is increased. However, at more intense fields ($\epsilon = 0.04$ a.u.) the planar conical intersection is energetically inaccessible and the decay occurs at a slower time scale, at the segment of the seam with more twisted geometries. In the third step, the control over the dynamics is exerted with a non-resonant dynamic field. The acceleration of the decay due to the improved vibrational overlap does not occur, but the decay can be made slower with a dynamic field of 0.08 a.u. The results show the viability of our approach to control the photophysics shaping the topology of the conical intersection seam, and they prove that the extended nature of the seam is crucial for simulating and understanding the control.

1 Introduction

The control of chemical processes with light is a long pursued goal of chemists.¹⁻³ Thanks to the development of laser technology, in recent years it has become a realistic goal, which can be applied at many different levels. Control

Institut de Química Computacional and Departament de Química, Universitat de Girona, Campus de Montilivi, 17071 Girona, Spain

has been achieved, for example, over the translational and rotational degrees of freedom of molecules, orienting them with the help of external electric fields.⁴ It has also become possible to control chemical processes with properly shaped resonant pulses that guide the wave packet on the potential energy surface.⁵⁻⁷ Usually these pulses have complicated shapes or consist of so-called 'trains of pulses' which are developed using optimal and local control theories.⁸⁻¹¹ While these approaches have been successful in a number of cases, one of their drawbacks is that they remain notoriously difficult to interpret.

In recent years, an alternative approach has been developed where the control is achieved by means of a non-resonant field. The field shifts the potential energy surfaces through the Stark effect.^{12,13} Intense fields are required to achieve a chemically relevant effect, and in turn this requires the use of dynamic fields. In this case one speaks of the non-resonant dynamic Stark effect (NRDSE). Control by means of the NRDSE is a very appealing approach because the picture of shifting potential energy surfaces is more accessible to interpretation and even prediction than the optimal and local control schemes.

Experimentally, the most successful example of control with the NRDSE is the photodissociation of IBr, where the reaction channel probabilities have been modified by tuning the potential energy barriers with infrared laser pulses.¹² From the point of view of theory, several studies have addressed the control of the photochemistry of this and other diatomic molecules with the NRDSE.¹⁴⁻¹⁷ In most of these cases, nonadiabatic crossings play a key role in the control, and the control of the dynamics can be understood by changes in the position of the crossings and the couplings between the surfaces. More recently, the NRDSE has been used to simulate optical control in polyatomic molecules.¹⁸⁻²⁰ Here the crossings have the form of conical intersections, which appear as the ideal target to exert control. In fact, during the last decades theoreticians have developed a very detailed picture of conical intersections and their role in photochemistry and photophysics.²¹⁻²⁵ In this context, the challenge is to achieve control by combining this mechanistic knowledge with the ability to tune the potential energy surfaces, and develop what one can call *mechanistic control* schemes.

One important feature of conical intersections that has not been considered in previous NRDSE studies is the fact that they are not isolated points on the potential energy surface, but form part of multidimensional seams of intersection.²⁶⁻²⁹ The multidimensional nature is important in photophysics and photochemistry and has to be included in the control simulations of polyatomic molecules. Thus, the multi-dimensionality facilitates the traversal of the intersection and has a strong influence on the excited state lifetimes. For photochemical problems, we have also introduced the notion of the extended seam of intersection, where the seam space is composed of different segments associated to different reaction paths on the surface, leading to different products.³⁰⁻³⁴ The traversal of the wave packet through the different seam segments determines the chemical outcome of the excitation. Based on this idea, the possibility of control at the seam has been explored guiding semiclassical dynamics trajectories to the different seam segments by adding momentum in different directions.^{31,35-37} Here we propose to follow a similar idea in the context of the NRDSE. Thus, the extended seam should be the ideal playground for the NRDSE, since by shifting the potential energy surface

one may favour one or the other associated path. Therefore, our central aim is to use the NRDE to develop mechanistic control strategies centred on the traversal of the wave packet through the extended seam.

As a first attempt to develop such a strategy, we consider the photophysics of fulvene, a non-fluorescent hydrocarbon.^{38–40} We aim to simulate the control of its excited state lifetime by combining resonant and non-resonant laser pulses, as shown in the inset of Fig. 1. The photophysics of fulvene have been studied extensively, and the non-emitting nature is due to an energetically accessible conical intersection seam between the ground and excited state, where the excited state decays after the excitation.⁴¹ The relevant segment of the seam of intersection lies along two nuclear coordinates, one corresponding to a bond-alternation mode, and the other to the torsion of the methylene group (Fig. 1).³⁴ Every point on the seam is a conical intersection when plotted along the proper coordinates (the branching space vectors, see below). We have recently simulated the excited state dynamics of fulvene with quantum dynamics calculations using the multiconfigurational time-dependent Hartree approach (MCTDH)^{42–45} and a four-dimensional model surface that includes the extended seam and its connection with the Franck–Condon structure.⁴⁶ In the calculations, the wave packet decays initially along the bond-alternation coordinate and reaches the seam at a segment with a planar geometry, centred around structure CI_{plan} . This corresponds to path (1) in Fig. 1. Most of the excited state population follows this mechanism and returns to the ground state in less than 10 fs after the excitation pulse. For the fraction of the wave packet that remains in the excited state, the torsional mode is activated after 40–100 fs, depending on the

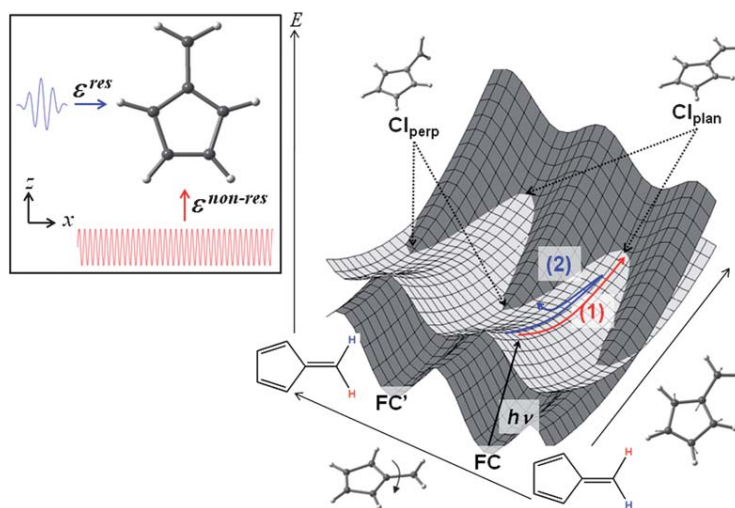


Fig. 1 Two-dimensional potential energy surface for the decay of singlet excited fulvene along the torsional and symmetric bond alternation coordinates, displaying the path for decay at (1) planar and (2) twisted conical intersection geometries. The equivalent ground state minima, related by double bond torsion, are labelled **FC** and **FC'**. Structures **CI_{plan}** and **CI_{perp}** correspond to the conical intersection stationary points on the seam where the methylene group lies in the plane of the ring and is perpendicular to the plane, respectively. The inset shows the combination of resonant pump pulse and non-resonant control pulse used in the propagations.

intramolecular vibrational energy redistribution (IVR) rate from the initially activated bond stretching mode. As a result, the wave packet samples the other regions of the seam and decays following path (2) in Fig. 1.

In this contribution we have used the NRDSE to control the excited state lifetime by modulating the topography of the seam. Thus, potential energy surface calculations show that the planar segment of the seam associated to the early decay can be made inaccessible at sufficiently intense fields. This suggests that the excited state lifetime can be prolonged under these conditions. To prove this hypothesis, we have added the non-resonant field to our four-dimensional model potential, and we have carried out MCTDH propagations with static and dynamic non-resonant strong fields. With a static field of 0.04 au (2.1×10^{10} V m⁻¹ or 1.1×10^{14} W cm⁻²), the lifetime is extended to about 40 fs, and a similar effect can be obtained with a dynamic field of 0.08 a.u. (4.1×10^{10} V m⁻¹ or 4.5×10^{14} W cm⁻²). We also discuss the main practical limitation of the approach for the present fulvene case. Thus, our model only considers two electronic states, but at high field strengths the S_2 excited state interferes with S_0 and S_1 . This indicates that more states should be included in the dynamics to make the treatment more accurate.

2 Four-dimensional model for fulvene

To describe the photophysics of fulvene with quantum dynamics it is necessary to construct a model potential of reduced dimension that reproduces the relevant regions of the potential energy surface. These are the low energy regions of the seam and the minimum energy path from the Franck–Condon structure, which is where the excited state dynamics starts, to the seam. Such a model surface, in four dimensions, has been described in detail in ref. 46. Here we summarize its main features.

The model is based on electronic structure calculations at the complete active space self-consistent field (CASSCF) level of theory, and a detailed characterization of the seam of intersection. The four coordinates are shown in Fig. 2. The initial decay

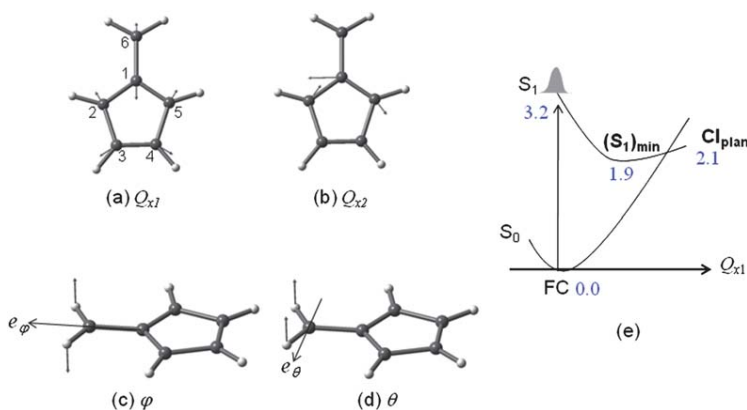


Fig. 2 Coordinates of the four dimensional model: (a) totally symmetric bond stretch, (b) non-totally symmetric bond stretch, (c) methylene torsion, and (d) methylene pyramidalization; (e) energy profile along the Q_{x1} coordinate at planar geometries (model energies in eV). e_φ and e_θ in (c) and (d) are the rotation axes of the rigid CH_2 fragment for φ and θ , respectively (see text).

takes place along the bond alternation coordinate Q_{x1} (Fig. 2a), and the corresponding energy profile is shown in Fig. 2e. The decay along Q_{x1} leads to a minimum on the excited state surface, $(S_1)_{\min}$, and further to a conical intersection with the ground state, $\mathbf{CI}_{\text{plan}}$. $\mathbf{CI}_{\text{plan}}$ belongs to an extended seam with two low energy segments along the CH_2 torsion and pyramidalization. These segments are described in our model by coordinates φ and θ , respectively. The global minimum energy CI is found along the torsion coordinate, at $\varphi = 63^\circ$, approximately. The model also contains the coupling coordinate Q_{x2} . Q_{x2} is a non-totally symmetric bond stretch coordinate approximately equal to the interstate coupling vector \mathbf{ic} along the seam. This vector is one of the branching space vectors that lift the degeneracy linearly at the intersection, together with the gradient difference \mathbf{gd} (see eqn (1)):

$$\mathbf{gd} = \nabla_{\mathbf{Q}}(E_2 - E_1) \quad (1a)$$

$$\mathbf{ic} = \langle \Phi_1 | \nabla_{\mathbf{Q}} \hat{H}_{el} | \Phi_2 \rangle \quad (1b)$$

Φ_i is the adiabatic electronic wave function for state i . The four coordinate model captures the essential details of the early excited state dynamics, since it connects the Franck–Condon structure with the seam and reproduces the main features of the seam. Thus, by including coordinates φ and θ we include the low energy seam segments. Our model also reproduces the branching space along these segments, since the \mathbf{gd} vector corresponds to combinations of Q_{x1} with φ or θ , while Q_{x2} is a good approximation to the \mathbf{ic} vector along the whole seam.

Using this model, the dynamics are carried out solving the time-dependent Schrödinger equation (eqn (6)):

$$i\hbar \frac{\partial}{\partial t} \begin{pmatrix} |\Psi_1^d(t)\rangle \\ |\Psi_2^d(t)\rangle \end{pmatrix} = (\mathbf{T} + \mathbf{W} + \mathbf{H}_{\text{int}}) \begin{pmatrix} |\Psi_1^d(t)\rangle \\ |\Psi_2^d(t)\rangle \end{pmatrix} \quad (2)$$

The calculations are carried out using the regularized diabatic states approach, where the couplings are expressed through off-diagonal potential terms of the potential matrix \mathbf{W} and the kinetic energy operator (KEO) \hat{T} is diagonal.⁴⁷ Q_{x1} and Q_{x2} are treated as mass-weighted Cartesian displacements, whereas φ and θ are curvilinear coordinates. The elements of the KEO are given by eqn (3).

$$\hat{T} = \sum_{i=1,2} \hat{T}_{Q_{xi}} + \hat{T}_{\varphi} + \hat{T}_{\theta} \quad (3a)$$

$$\hat{T}_{Q_{xi}} = -\frac{1}{2\mu_i} \frac{\partial^2}{\partial Q_{xi}^2} \quad (i = 1, 2) \quad (3b)$$

$$\hat{T}_{\xi} = -\frac{1}{2I_{\xi}} \frac{\partial^2}{\partial \xi^2} \quad (\xi = \varphi, \theta) \quad (3c)$$

where μ_i is the reduced mass of Q_{xi} , φ and θ correspond to rotations of the rigid CH_2 fragment around the e_{φ} and e_{θ} axes shown in Fig. 2c and 2d, respectively, and I_{ξ} is the moment of inertia corresponding to coordinate ξ . The details of the KEO and the approximations involved are discussed further in ref. 46.

\mathbf{H}_{int} describes the interaction between the wave packet and the external electric field. For the parametrization of the surface, it is convenient to separate \mathbf{H}_{int} in a resonant and a non-resonant term (eqn (4)):

$$\mathbf{H}_{\text{int}} = \mathbf{H}_{\text{int}}^{\text{res}} + \mathbf{H}_{\text{int}}^{\text{non-res}} \quad (4a)$$

$$\mathbf{H}_{\text{int}}^{\text{res}} = \begin{pmatrix} 0 & \mu_{12}\varepsilon^{\text{res}}(t) \\ \mu_{12}\varepsilon^{\text{res}}(t) & 0 \end{pmatrix} \quad (4b)$$

$$\mathbf{H}_{\text{int}}^{\text{non-res}} = \begin{pmatrix} \mu_1(\mathbf{Q})\varepsilon^{\text{non-res}}(t) + \frac{\alpha_1(\mathbf{Q})}{2}(\varepsilon^{\text{non-res}}(t))^2 & 0 \\ 0 & \mu_2(\mathbf{Q})\varepsilon^{\text{non-res}}(t) + \frac{\alpha_2(\mathbf{Q})}{2}(\varepsilon^{\text{non-res}}(t))^2 \end{pmatrix} \quad (4c)$$

ε^{res} and $\varepsilon^{\text{non-res}}$ are the resonant and non-resonant field components, respectively. In eqn (4b), μ_{12} is the transition dipole moment between states 1 and 2, while μ_i and α_i in eqn (4c) are the dipole moments and polarizabilities of state i , respectively. \mathbf{H}_{int} has a simple physical interpretation: Thus, the resonant field interaction that pumps the population from the ground to the excited state works through the transition dipole moment between the states, while the non-resonant interaction that shifts the potentials takes place through the dipole moment and the polarizability of the states. In our model we assume that the molecules are aligned in space during the propagation, and in this case the two components of \mathbf{H}_{int} correspond also to different spatial orientations of the pulse. Thus, in fulvene, μ_{12} is oriented along the x axis (see Fig. 1), whereas the dipole moments are oriented along the z axis. Therefore, in our model the resonant and non-resonant pulses are perpendicular to each other, as shown in Fig. 1. The model only includes the zz components of the polarizability tensor and neglects the Stark shift due to the resonant pulse, since this pulse is only applied during a short pumping period of 5 fs.

3 Parametrization of the field-dependent potential

To carry out the dynamics it is necessary to obtain the parameters of the potential matrix \mathbf{W} and the dipole moments and polarizabilities from the non-resonant field matrix $\mathbf{H}_{\text{int}}^{\text{non-res}}$. The parametrization is carried out against *ab initio* calculations. The dipole moments and polarizabilities in eqn (4c) are coordinate dependent and are not calculated explicitly. Instead, the combined set of parameters of both matrices are obtained from a single fit. To this end, we start by defining a coordinate- and field-dependent potential \mathbf{V} of the form:

$$\mathbf{V}(\mathbf{Q}, \varepsilon) = \mathbf{W}(\mathbf{Q}) + \mathbf{H}_{\text{int}}^{\text{non-res}}(\mathbf{Q}, \varepsilon) = V^0(\mathbf{Q}, \varepsilon) \mathbf{I} + \begin{pmatrix} V_{11}(\mathbf{Q}, \varepsilon) & V_{12}(\mathbf{Q}) \\ V_{12}(\mathbf{Q}) & V_{22}(\mathbf{Q}, \varepsilon) \end{pmatrix} \quad (5)$$

The terms of \mathbf{V} have a similar form to the field free potential \mathbf{W} from our previous study. They form a Taylor expansion along Q_{x1} , Q_{x2} , $\sin(\varphi)$ and θ , centred at the planar conical intersection $\mathbf{CI}_{\text{plan}}$:

$$\begin{aligned} V^0(\mathbf{Q}, \varepsilon) &= V^0(\varepsilon) + (\lambda_{x1}(\varepsilon) + \lambda_{x1,\varphi}(\varepsilon)\sin^2(\varphi))Q_{x1} \\ &+ \frac{1}{2}(\omega_{x1}(\varepsilon) + \omega_{x1,\varphi}(\varepsilon)\sin^2(\varphi))Q_{x1}^2 + \frac{1}{2}\omega_{\varphi}(\varepsilon)\sin^2(\varphi) \\ &+ \frac{1}{2}\varsigma_{\varphi}\sin^4(\varphi) + \left(\frac{1}{2}\omega_{\theta} + \frac{1}{2}\omega_{x1,\theta}Q_{x1} + \frac{1}{2}\omega_{\varphi,\theta}\sin^2(\varphi)\right)\theta^2 \\ &+ \left(\frac{1}{2}\varsigma_{\theta} + \frac{1}{2}\varsigma_{x1,\theta}Q_{x1} + \frac{1}{2}\varsigma_{\varphi,\theta}\sin^2(\varphi)\right)\theta^4 + \frac{1}{2}\omega_{x2}Q_{x2}^2 \end{aligned} \quad (6a)$$

$$V_{11}(\mathbf{Q}, \varepsilon) = -\frac{1}{2} \left[\begin{aligned} &\delta V(\varepsilon) + [\delta\kappa_{x1}(\varepsilon) + \delta\kappa_{x1,\varphi}(\varepsilon)\sin^2(\varphi)] Q_{x1} \\ &+ \frac{1}{2} [\delta\gamma_{x1}(\varepsilon) + \delta\gamma_{x1,\varphi}(\varepsilon)\sin^2(\varphi)] Q_{x1}^2 + \frac{1}{2} \delta\gamma_{\varphi}(\varepsilon)\sin^2(\varphi) \\ &+ \frac{1}{2} \chi_{\varphi} \sin^4(\varphi) + \left(\frac{1}{2} \delta\gamma_{\theta} + \frac{1}{2} \delta\gamma_{x1,\theta} Q_{x1} + \frac{1}{2} \delta\gamma_{\varphi,\theta} \sin^2(\varphi) \right) \theta^2 \\ &+ \left(\frac{1}{2} \chi_{\theta} + \frac{1}{2} \chi_{x1,\theta} Q_{x1} + \frac{1}{2} \chi_{\varphi,\theta} \sin^2(\varphi) \right) \theta^4 + \frac{1}{2} \delta\gamma_{x2} Q_{x2}^2 \end{aligned} \right] \quad (6b)$$

$$V_{22}(\mathbf{Q}, \varepsilon) = -V_{11}(\mathbf{Q}, \varepsilon) \quad (6c)$$

$$V_{12}(\mathbf{Q}) = \left(\kappa_{\varphi,\theta}^{AB} \sin^2(\varphi) + \kappa_{\varphi,\theta 2}^{AB} \sin^4(\varphi) \right) \theta + \kappa_{x2}^{AB} Q_{x2} \quad (6d)$$

The field dependence is introduced making some of the parameters in eqn (6a) and (6b) depend on $\varepsilon^{\text{non-res}}$ (the superscript is left out for simplicity). These parameters are second-order expansions of ε , and the parameters of this expansion correspond to the dipole and polarizability terms from eqn (4c). For example, the first term of the right hand side of eqn (6a) is:

$$V^0(\varepsilon) = V_0^0 + \mu^0 \varepsilon + \frac{\alpha^0}{2} \varepsilon^2 \quad (7)$$

where V_0^0 is zero because the energy at the centre of the expansion is zero. The same applies for the $\delta V(\varepsilon)$ term of eqn (6b). Similarly, the second term has the form:

$$\lambda_{x1}(\varepsilon) = \lambda_{x1,0} + \mu_{\lambda,x1} \varepsilon + \frac{\alpha_{\lambda,x1}}{2} \varepsilon^2 \quad (8)$$

The remaining terms have a similar form. This model has several simplifications with respect to the way the field is included. First, the field dependent terms along Q_{x2} and θ are neglected for simplicity. In practice, this implies that the non-resonant field produces a constant Stark shift along these coordinates. In addition, the Stark effect on the parameters of the coupling element V_{12} and the transition dipole moment μ_{12} is also neglected. Finally, we only consider the zz component of the polarizability and we neglect the Stark shift caused by the resonant pulse along the x axes, which would correspond to the xx and xz polarizability components.

The field-dependent parameters are fitted to *ab initio* calculations in the subspace formed by Q_{x1} and φ . The energy is calculated for several values of ε , where the external field along the z axis is included in a self-consistent way. In practice, this means fitting the terms of V to a three-dimensional grid of points along Q_{x1} , φ and ε . The calculations are carried out at the CASSCF/cc-pvdz level of theory, using an active space of six electrons in six orbitals, with the Gaussian program package.⁴⁸ This level of theory does not include dynamic electronic correlation. However, the comparison of the CASSCF data with complete active space second order perturbation CASPT2 calculations shows that the effect of dynamic correlation is small and can be neglected for the present purposes.⁴⁶

In the space formed by Q_{x1} and φ , the electronic states S_0 and S_1 have A and B symmetry. Because of the different symmetry, the *ab initio* potential energy surface is equal to the diabatic potential, and the *ab initio* data can be used directly for the fit. The elements of V^0 are fitted to the average of the S_1 and S_0

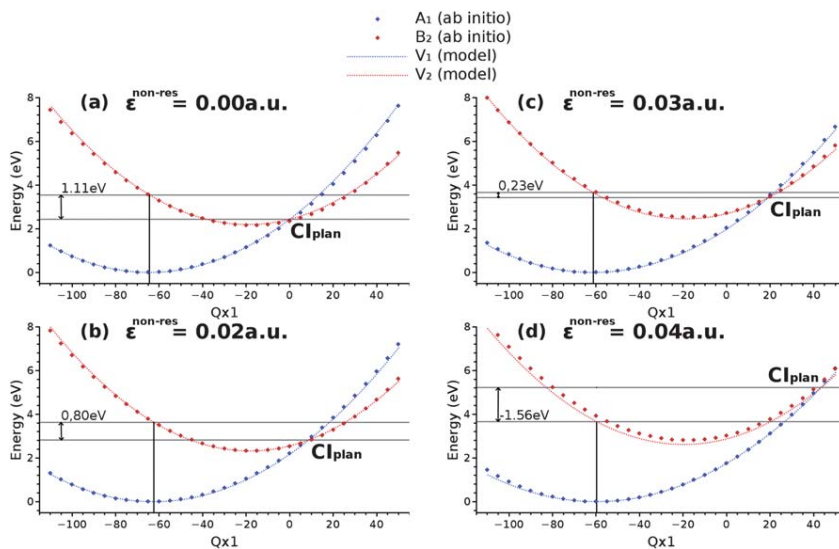


Fig. 3 Energy profile along Q_{x1} at different non-resonant field intensities (cuts for $(Q_{x2}, \varphi, \theta) = (0, 0, 0)$), including the energy difference between the vertical excitation and CI_{plan} . Blue and red diamonds: *ab initio* energies of the A_1 and B_2 states, respectively. Blue and red dashed lines: V_1 and V_2 model energies, respectively. Q_{x1} displacements in mass-weighted atomic units, energies in eV.

ab initio energies, while the elements of V_{11} are fitted to the difference between the energies of the two states. In the *ab initio* calculations, the electric field is included over a range of ± 0.04 a.u. However, at field strengths of -0.02 a.u. and lower, S_2 (of A symmetry) interferes with the S_0 and S_1 states at regions with values of φ close to 90° . At these geometries, S_2 has a large dipole moment because of a charge transfer from the methylene group to the ring, and the Stark shift is more pronounced than for the lowest pair of states. The interference of S_2 leads to discontinuities in the potential, and to facilitate the fit the corresponding points are discarded. This is the case for 805 *ab initio* points out of a total of 14190. The set of 34 parameters that depend on Q_{x1} , φ and ϵ are then fitted to the remaining 13 385 points using the nonlinear least-squares Marquardt–Levenberg algorithm implemented in Gnuplot.⁴⁹ The root mean square of residuals is 0.0024 Hartree for V_0 and 0.0032 for V_{11} . The good agreement between the model and the *ab initio* is shown below (Fig. 3) for energy cuts along Q_{x1} at different field strengths. The remaining 19 parameters of the model are taken over from ref. 46.

4 Stark effect on the potential energy surface

We start our approach to the control with an analysis of the Stark effect on the potential energy surface, focusing on the changes along the decay path. This analysis gives a preliminary idea of the field strengths that will be required to achieve a significant extension of the excited state lifetime in the propagations, and it also shows the physical origin of the shifts that will allow for the control. In Fig. 3 we plot the energy profile along Q_{x1} at different field strengths, 0.00 a.u., -0.02 a.u., -0.03 a.u. and -0.04 a.u. As the field is applied, CI_{plan} is shifted along

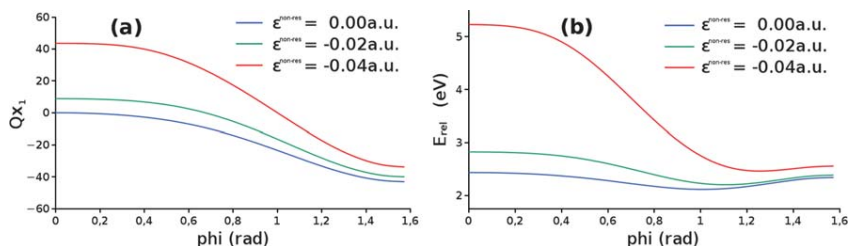


Fig. 4 (a) Locus of the V_2/V_1 seam in the (Q_{x1}, ϕ) plane (projections for $(Q_{x2}, \theta) = (0, 0)$) and (b) seam energy along ϕ , at different field strengths. $\mathbf{CI}_{\text{plan}}$ corresponds to $\phi = 0$ rad, and $\mathbf{CI}_{\text{perp}}$ to $\phi = \pi$ rad.

Q_{x1} and its energy relative to the S_1 vertical excitation energy (marked with dotted lines) increases. Thus, $\mathbf{CI}_{\text{plan}}$ lies well below the vertical excitation with no field and with a -0.02 a.u. field (1.11 and 0.80 eV, respectively). At -0.03 a.u., $\mathbf{CI}_{\text{plan}}$ lies only 0.23 eV lower than the vertical excitation, and at -0.04 a.u. it lies 1.56 eV higher in energy. The effect of the field on the topography of the extended seam is shown in Fig. 4, where we display the projection of the seam in the (Q_{x1}, ϕ) space. Thus, Fig. 4a shows the locus of the seam in this two-dimensional space, and Fig. 4b shows its energy. Both plots show that the field mainly changes the seam at planar structures, shifting the position and energy of $\mathbf{CI}_{\text{plan}}$ as discussed for Fig. 3. In contrast to this, the changes in the seam around $\mathbf{CI}_{\text{perp}}$ are small.

Overall, our results show that the potential does not respond linearly to the external field. Instead, the main changes are due to the second order terms with respect to the field, *i.e.* the polarizability. This is due to the fact that the two states are only weakly polar. This is important for our purposes because in practice the control has to be exerted with a dynamic, oscillating pulse, and in this case the dominant effect will be due to the polarizability. The energy profiles in Fig. 3 also show that the changes in the energy and position of the CI are due to the relative shifts of the two states, combined with changes in the shape of the surface. These changes are especially important for the ground state, which becomes flatter as the field is increased. This reflects the changes in the dipole moment and the polarizability along Q_{x1} and justifies the inclusion of the coordinate dependence in the dipole and polarizability parameters of our model (eqn (4)). On the basis of these results we can also expect that a field strength of -0.04 a.u. will be required to extend the lifetime of the excited state, since at this intensity the energy of the CI lies notably higher than the vertical excitation.

5 Excited state dynamics under a non-resonant field

The quantum dynamics propagations controlled by the non-resonant field have been carried out with the MCTDH approach. We have run two sets of calculations with static and dynamic non-resonant electric fields. In this section we describe the details of the propagations and the results for the two sets.

5.1 MCTDH propagation details

The MCTDH dynamics were carried with the Heidelberg MCTDH package.⁴⁵ For Q_{x1} and Q_{x2} we use a primitive basis of 48 and 25 harmonic oscillator functions,

respectively, for φ a fast Fourier transform collocation of 128 functions, and for θ a primitive basis of 25 sine functions. For the single particle basis, we have used a combined mode for Q_{x1} and φ (50 single particle functions (SPF) per diabatic state), as explained in section 4.5 of ref. 42, and 25 and 20 SPF per state for Q_{x2} and θ , respectively. The propagations, which were run over 150 fs, are well converged with respect to the number of SPF, since in all runs the maxima over time of the lowest natural weight for all modes did not exceed 0.001. The propagations were initiated relaxing the wave packet in the electronic and vibrational ground state, and exciting it to the electronic excited state with a single laser pulse of the form:

$$\varepsilon^{\text{res}}(t) = \varepsilon_0^{\text{res}} \cos(\omega^{\text{res}} t) \sin^2\left(\frac{\pi}{\tau} t\right) \quad (9)$$

In eqn (7), $\varepsilon_0^{\text{res}}$ is the maximum intensity of the resonant pulse, which was set to 0.075 a.u. ($3.9 \times 10^{10} \text{ V m}^{-1}$ or $3.9 \times 10^{14} \text{ W cm}^{-2}$) for all runs except for the run with a non-resonant dynamic pulse with maximum intensity 0.08 a.u., where $\varepsilon_0^{\text{res}}$ was set to 0.10 a.u. to achieve an initial V_2 population of 0.4. Further, $\hbar\omega^{\text{res}}$ is the excitation energy (3.6 eV), and τ the pulse duration (5 fs). The pulse was set to zero outside the $[0, \tau]$ interval. For the propagations with a dynamic non-resonant field, the field has a simple sinusoidal shape with a carrier frequency $\hbar\omega^{\text{non-res}}$ of 1 eV (eqn (8)), which corresponds to a wave length of 1239 nm:

$$\varepsilon^{\text{non-res}}(t) = -\varepsilon_0^{\text{non-res}} \sin(\omega^{\text{non-res}} t) \quad (10)$$

5.2 Propagations under static non-resonant fields

To understand the effect of the off-resonant pulse on the dynamics, we start with a set of propagations with a constant (static) field of various strengths. In Fig. 5a we show the evolution of the excited state populations (V_2 diabatic state) during the first 50 fs of three propagations with fields of 0.00, -0.02 and -0.03 a.u. In all cases, the resonant pulse takes place during the first 5 fs of the propagation (eqn (7)). During this time, the V_2 population rises from an initial value of 0.0 to a maximum value of approximately 0.4. Due to the very favourable energy profile (Fig. 3), the wave packet decays quickly to the ground state and there is a sharp drop of the population in the first 20 fs. However there are some differences between the propagations with the different fields. In the field free case, the population decreases to approximately 0.15 after a total of 20 fs (blue line). When the field is applied, the initial decay becomes

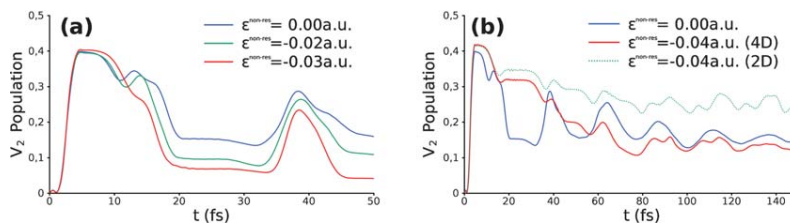


Fig. 5 V_2 population for propagations with static non-resonant fields of different intensities. (a) Non-resonant field intensity 0.00 a.u. (blue profile), -0.02 a.u. (green profile), and -0.03 a.u. (red profile). (b) Non-resonant field intensity 0.00 a.u. (blue profile), -0.04 a.u. (red profile) and -0.04 a.u. on a two-dimensional reduced model (green hashed profile, see text). Note the different time axes for (a) and (b).

more efficient, and the populations after 20 fs are approximately 0.10 and 0.08 with fields of -0.02 and -0.03 a.u., respectively. This result is somewhat counterintuitive, since the field shifts the planar conical intersection up in energy (Fig. 3), in which case a less efficient decay might be expected. However the result can be understood in terms of overlap between vibrational levels. According to the Franck–Condon principle, the V_2 vibrational level that absorbs most of the excited state population during the pump pulse will be that corresponding to the vertical excitation. Then, the $V_2 \rightarrow V_1$ population transfer rate depends in first instance on the overlap between the vibrational function of this level and that of the degenerate V_1 vibrational level. The overlap increases as the vertical excitation and conical intersection energies get closer, and it becomes maximal when both energies are equal, which occurs in our model for a field of approximately -0.032 a.u. This explanation agrees with the result that the most efficient decay is observed at a field of -0.03 a.u.

With a stronger field of -0.04 a.u., the situation is reversed and the decay is slower (Fig. 5b). Thus, the population that remains in V_2 after 20 fs is approximately 0.30, and it takes approximately 45 fs to reach a value of 0.20 (red line of Fig. 5b). This is due to the fact that the planar conical intersection lies substantially higher in energy than the vertical excitation. To illustrate this point, we compare the evolution of the wave packet on V_2 with fields of 0.00 a.u. and -0.04 a.u. for several snapshots (Fig. 6). The wave packet isodensity and the seam are plotted in red and black, respectively. The time and V_2 population of the snapshot are also displayed. Note that the wave packet is split in two halves because φ is a periodic coordinate, and the wave packet is centred initially around $\varphi = 0^\circ$. In the field free case, after 20 fs, the wave packet has traversed the seam at the planar region ($\varphi \approx 0^\circ$), and there is a substantial population decay from a maximum of 0.40 to 0.16. In contrast to this, at a field of -0.04 a.u. the wave packet does not reach the planar seam region in early times. The population decay is slower, and the population after 20 fs is 0.32. In this propagation, the wave packet has to spread along φ to reach the lower energy regions of the seam and decay to V_1 efficiently. This happens after approximately 36 fs, and at 44 fs the V_2 population is reduced to 0.21. Once the wave packet spreads along φ and accesses the seam, the control effect is lost, and the populations in the two propagations are similar. The time that the wave packet requires to spread corresponds to IVR from the initially activated Q_{x1} mode to the torsion coordinate φ , and the present value of approximately 36 fs is in good agreement with our previous study on fulvene excited state dynamics. In that case IVR took place after about 40 fs with an excitation energy of 3.5 eV.

To assess this point further, we have repeated the propagation with constant -0.04 a.u. field strength on a reduced two-dimensional potential surface, where the rotation and pyramidalization coordinates φ and θ are not included. This excludes the possibility of decay along the extended seam, since the CI is reduced to a point. The decay of the V_2 population is slower than in the four dimensional case (green line of Fig. 5b), and the population decrease at around 40 fs due to access to the twisted regions of the seam is not observed. This confirms that the main fraction of the wave packet decays at the twisted segment of the seam in the propagation under the -0.04 a.u. static field. In more general terms, it illustrates the need to include the extended seam to carry out reliable simulations of the decay.

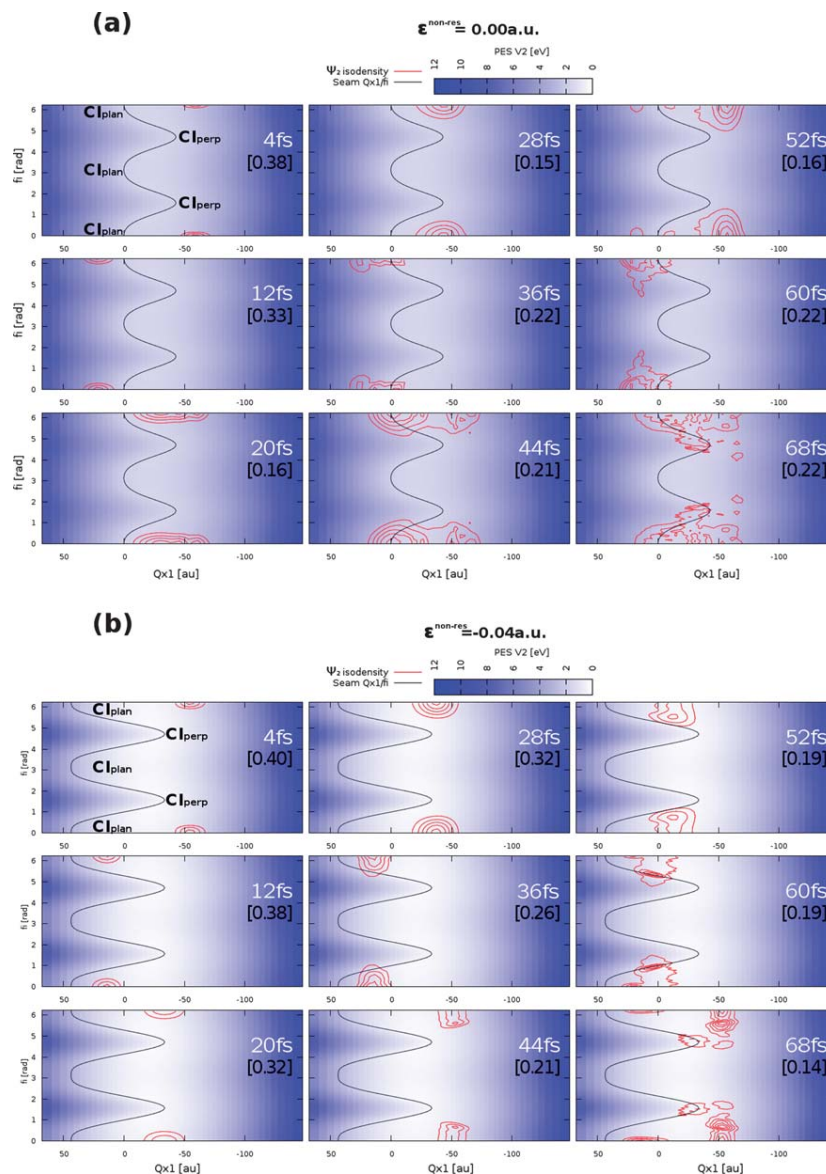


Fig. 6 Snapshots of the wave packet propagations on the V_2 model surface along Q_{x1} and φ (integrated density along Q_{x2} and θ ; coordinates in mass-weighted atomic displacements and radians, respectively), displaying the time of the snapshot and the V_2 population. Propagations carried out (a) without non-resonant field and (b) with a static non-resonant field of -0.04 a.u. Energy scale shown in the top of the figure. Wave packet density plotted in red and seam position in black. The wave packet is split in two halves because it is centred initially around $\varphi = 0^\circ$ in the periodic coordinate φ .

5.3 Propagations with dynamic non-resonant field

A realistic simulation requires the use of a dynamic non-resonant field to achieve the necessary field strengths. Thus, we have assessed the viability of our control strategy carrying out propagations with a dynamic field and a carrier wave length

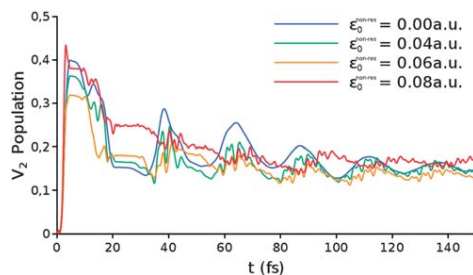


Fig. 7 V_2 population for propagations with dynamic non-resonant fields of different intensities. Maximum field intensity $\varepsilon_0^{\text{non-res}}$: 0.00 a.u. (blue profile), 0.04 a.u. (green profile), 0.06 a.u. (yellow profile), and 0.08 a.u. (red profile).

of 1239 nm, which is close to the value of 1700 nm used in experiments.¹² This corresponds to a non-resonant pulse period of approximately 4 fs. We assume that the non-resonant pulse is switched on before the resonant one and is not modified during the whole propagation. As a rule of thumb, one can estimate that the average effect on the potential of a dynamic field with maximum strength $\varepsilon_0^{\text{non-res}}$ is that of a static field with half the strength, because both have the same intensities integrated over time. Thus, we have carried out propagations using dynamic pulses with $\varepsilon_0^{\text{non-res}}$ equal to 0.04 a.u., 0.06 a.u. and 0.08 a.u. and compared them with the propagations using static fields of -0.02 a.u., -0.03 a.u. and -0.04 a.u. The results are shown in Fig. 7. With dynamic non-resonant fields of 0.04 a.u. and 0.06 a.u. maximum intensity, the V_2 populations have a similar evolution to the propagation without resonant field. Moreover, the acceleration of the decay seen with static fields of -0.02 a.u. and -0.03 a.u. is not seen with dynamic fields. This happens because the improved vibrational overlap that causes the faster decay in the static case is not a linear function of the field, and the average effect of the dynamic field on the rate is not the same as the effect caused by a static field with the same intensity integrated over time. In contrast to this, the delay of the decay observed for a dynamic field of 0.08 a.u. is similar to that observed with a static -0.04 a.u. field, although it is less pronounced. These examples show that the ‘rule of thumb’ given above to estimate the effect of a dynamic field on the basis of the static field results can indeed provide the correct general picture, since it has allowed us to predict that a significant delay of the decay would be observed with a dynamic field of maximal -0.08 a.u. intensity. However, this approximation also fails to detect subtle effects such as the acceleration due to improved vibrational overlap observed for static fields of -0.02 a.u. and -0.03 a.u.

6 Conclusions

Our work shows that it is possible to simulate the control of the photophysics of an organic molecule by shaping the topography of an extended conical intersection seam with the NRDSE. We have followed a three step approach, where we have first characterized the Stark effect on the topography of the seam. *Ab initio* calculations suggest that a field strength of 0.04 a.u. is required to increase the excited state lifetime significantly. Second, we have simulated the control with

static non-resonant pulses and find that the lifetime can be reduced with fields up to 0.03 a.u. because the overlap between the degenerate electronic excited and ground state vibrational functions is increased. In contrast to this, a field of 0.04 a.u. increases the excited state lifetime from less than 10 fs in the field free case to approximately 40 fs. Finally, in the third step we have shown that a similar reduction of the decay rate can be achieved with a dynamic, sinusoidal non-resonant pulse of 0.08 a.u. maximal strength.

In fulvene, the decay along the non-planar segment of the seam is associated with rotation of the methylene group and isomerization of the exocyclic double bond. The present results raise the question if the isomerization process can also be controlled with the NRDSE. Preliminary analyses indicate that the NRDSE on the isomerization is not so substantial, *i.e.* the fraction of fulvene that undergoes double bond isomerization before the decay is not modified much by the non-resonant field. This happens presumably because the changes on the topography of the seam at twisted methylene angles are not so pronounced than at planar geometries. Moreover, it seems that the IVR rate which induces the methylene torsion is not affected by the topological changes induced by the Stark effect. This issue will be considered in more detail in future work, where we will also consider the NRDSE on propagations with different vertical excitation energies, where the IVR rate can be modulated.

Our approach also has some limitations. The first one is the dimensionality of the reduced model surface. Our surface captures the main features of the decay because we are considering a very fast process where the excitation energy is concentrated in only a few modes. In addition, the choice of the coordinates is based on a careful analysis of the extended seam of intersection responsible for the photophysics. However, as discussed in ref. 46, the inclusion of more modes should improve the agreement of the model with the full-dimensional *ab initio* surface. It would also improve the description of the NRDSE. Thus, our model assumes implicitly that the energy shift due to the non-resonant pulse will be constant along all coordinates except Q_{x1} and φ . However, the Stark shift does change significantly along Q_{x1} and φ . This may also occur along other coordinates, which should be taken into account in a more refined model. Another limitation is due to the interference of the second excited state, S_2 , at fields of 0.02 intensity and more. At geometries where the methylene group is twisted, this state is more polar than the ground and the excited state, and becomes lower in energy. More states should be included in the simulation to take this effect into account and make the simulations more realistic. In addition, field strengths of up to 0.08 a.u., which corresponds to a power density of $4.5 \times 10^{14} \text{ W cm}^{-2}$, were needed to achieve the effects presented here. In practice, such power densities are likely to cause ionization, which makes the experimental implementation of an NRDSE based control scheme in fulvene challenging. To carry out the control experimentally, it is necessary to find molecules where the ground and excited state dipole moments and polarizabilities differ more substantially than in fulvene.

In more general terms, our work has provided us with a new insight into the relationship between the intersection topography and the dynamics. Thus, by modifying the topography with the external field we have shown that the most efficient decay occurs when the conical intersection is energetically degenerate with the Franck–Condon point. The work is also important because it shows the effect of the non-resonant field on the extended seam. The Stark shift of the potential energy

surface is not homogeneous, and as a result the topography of the seam undergoes different changes at different segments. In the present case, the largest effects are seen at planar structures. This makes it possible to control the excited state lifetime during the first 40 fs of the simulation, approximately, but the control is lost at longer times because the seam segment at twisted geometries is still accessible energetically. This demonstrates that the extended nature of the seam has to be taken into account in optical control simulations of polyatomic molecules, not only with the NRDE but probably also with other strategies.

Acknowledgements

This work has been supported by grants CTQ2008-06696 and CTQ2011-26573 from the Spanish Ministerio de Ciencia e Innovación (MICINN) and Ministerio de Economía y Competitividad (MINECO), respectively, SGR0528 from the Catalan Agència de Gestió d'Ajuts Universitaris i de Recerca (AGAUR), UNGI08-4E-003 from MICINN and the European Fund for Regional Development, and the Xarxa de Referència en Química Teòrica i Computacional de Catalunya from AGAUR. S.R.-B. thanks the MICINN for grant BES-2009-029177.

References

- 1 C. Brif, R. Chakrabarti and H. Rabitz, *New J. Phys.*, 2010, **12**, 075008.
- 2 C. Brif, R. Chakrabarti and H. Rabitz, *Adv. Chem. Phys.*, 2012, **148**, 1–76.
- 3 A. H. Zewail, in *Femtochemistry*, ed. F. C. De Schryver, S. De Feyter and G. Schweitzer, Wiley-VCH, Weinheim, Germany, 2001, pp. 1–86.
- 4 H. Stapelfeldt and T. Seideman, *Rev. Mod. Phys.*, 2003, **75**, 543–557.
- 5 T. Brixner and G. Gerber, *ChemPhysChem*, 2003, **4**, 418–438.
- 6 M. Dantus and V. V. Lozovoy, *Chem. Rev.*, 2004, **104**, 1813–1859.
- 7 V. V. Lozovoy and M. Dantus, *ChemPhysChem*, 2005, **6**, 1970–2000.
- 8 G. G. Balint-Kurti, S. Zou and A. Brown, *Adv. Chem. Phys.*, 2008, **138**, 43–94.
- 9 V. Engel, C. Meier and D. J. Tannor, in *Advances in Chemical Physics, Vol 141*, ed. S. A. Rice, 2009, vol. 141, pp. 29–101.
- 10 R. J. Levis, G. M. Menkir and H. Rabitz, *Science*, 2001, **292**, 709–713.
- 11 G. A. Worth and C. S. Sanz, *Phys. Chem. Chem. Phys.*, 2010, **12**, 15570–15579.
- 12 B. J. Sussman, D. Townsend, M. Y. Ivanov and A. Stolow, *Science*, 2006, **314**, 278–281.
- 13 D. Townsend, B. J. Sussman and A. Stolow, *J. Phys. Chem. A*, 2011, **115**, 357–373.
- 14 B. Y. Chang, H. Choi, S. Shin, S. Lee and I. R. Sola, *J. Mod. Opt.*, 2009, **56**, 811–821.
- 15 H. Choi, W.-J. Son, S. Shin, B. Y. Chang and I. R. Sola, *J. Chem. Phys.*, 2008, 128.
- 16 P. Marquetand and V. Engel, *Phys. Chem. Chem. Phys.*, 2005, **7**, 469–474.
- 17 S. Scheit, Y. Arasaki and K. Takatsuka, *J. Phys. Chem. A*, 2012, **116**, 2644–2653.
- 18 S. Belz, S. Zilberg, M. Berg, T. Grohmann and M. Leibscher, *J. Phys. Chem. A*, 2012, **116**, 11189–11198.
- 19 D. Kinzel, P. Marquetand and L. Gonzalez, *J. Phys. Chem. A*, 2012, **116**, 2743–2749.
- 20 G. W. Richings and G. A. Worth, *J. Phys. Chem. A*, 2012, **116**, 11228–11240.
- 21 F. Bernardi, M. Olivucci and M. A. Robb, *Chem. Soc. Rev.*, 1996, **25**, 321–328.
- 22 W. Domcke, D. R. Yarkony and H. Köppel, ed., *Conical Intersections: Electronic Structure, Dynamics & Spectroscopy*, World Scientific, Singapore, 2004.
- 23 W. Domcke, D. R. Yarkony and H. Köppel, ed., *Conical Intersections: Theory, Computation and Experiment*, World Scientific, Singapore, 2011.
- 24 M. Klessinger and J. Michl, *Excited States and Photochemistry of Organic Molecules*, VCH Publishers, Inc., New York, 1995.
- 25 D. R. Yarkony, *Rev. Mod. Phys.*, 1996, **68**, 985–1013.
- 26 G. J. Atchity, S. S. Xantheas and K. Ruedenberg, *J. Chem. Phys.*, 1991, **95**, 1862–1876.
- 27 A. Migani, M. A. Robb and M. Olivucci, *J. Am. Chem. Soc.*, 2003, **125**, 2804–2808.
- 28 D. R. Yarkony, *J. Chem. Phys.*, 2005, **123**, 204101.
- 29 L. Blancafort, B. Lasorne, M. J. Bearpark, G. A. Worth and M. A. Robb, in *The Jahn–Teller Effect: Fundamentals and Implications for Physics and Chemistry*, ed. H. Köppel, D. R. Yarkony and H. Barentzen, Springer, Heidelberg, Berlin, 2009, pp. 169–200.

- 30 M. Kobylecka, A. Migani, D. Asturiol, J. Rak and L. Blancafort, *J. Phys. Chem. A*, 2009, **113**, 5489–5495.
- 31 B. Lasorne, M. J. Bearpark, M. A. Robb and G. A. Worth, *J. Phys. Chem. A*, 2008, **112**, 13017–13027.
- 32 Q. Li, A. Migani and L. Blancafort, *J. Phys. Chem. Lett.*, 2012, **3**, 1056–1061.
- 33 A. Migani, L. Blancafort, M. A. Robb and A. D. Debellis, *J. Am. Chem. Soc.*, 2008, **130**, 6932–6933.
- 34 F. Sicilia, M. J. Bearpark, L. Blancafort and M. A. Robb, *Theor. Chem. Acc.*, 2007, **118**, 241–251.
- 35 C. S. M. Allan, B. Lasorne, G. A. Worth and M. A. Robb, *J. Phys. Chem. A*, 2010, **114**, 8713–8729.
- 36 D. Asturiol, B. Lasorne, G. A. Worth, M. A. Robb and L. Blancafort, *Phys. Chem. Chem. Phys.*, 2010, **12**, 4949–4958.
- 37 D. Mendive-Tapia, B. Lasorne, G. A. Worth, M. J. Bearpark and M. A. Robb, *Phys. Chem. Chem. Phys.*, 2010, **12**, 15725–15733.
- 38 K. R. Asmis, M. Allan, O. Schafer and M. Fulscher, *J. Phys. Chem. A*, 1997, **101**, 2089–2095.
- 39 P. J. Domaille, J. E. Kent and M. F. Odwyer, *Chem. Phys.*, 1974, **6**, 66–75.
- 40 J. E. Kent, P. J. Harman and M. F. Odwyer, *J. Phys. Chem.*, 1981, **85**, 2726–2730.
- 41 M. J. Bearpark, F. Bernardi, M. Olivucci, M. A. Robb and B. R. Smith, *J. Am. Chem. Soc.*, 1996, **118**, 5254–5260.
- 42 M. H. Beck, A. Jackle, G. A. Worth and H. D. Meyer, *Phys. Rep.*, 2000, **324**, 1–105.
- 43 H. D. Meyer, U. Manthe and L. S. Cederbaum, *Chem. Phys. Lett.*, 1990, **165**, 73–78.
- 44 H.-D. Meyer, F. Gatti and G. A. Worth, ed., *Multidimensional Quantum Dynamics: MCTDH Theory and Applications*, WILEY-VCH, Weinheim, Germany, 2009.
- 45 G. A. Worth, M. H. Beck, A. Jackle and H. D. Meyer, *The MCTDH Package, Version 8.2(2000)*, University of Heidelberg, Heidelberg, Germany. H.-D. Meyer, Version 8.3(2002), Version 8.4 (2007). See <http://mctdh.uni-hd.de>.
- 46 L. Blancafort, F. Gatti and H. D. Meyer, *J. Chem. Phys.*, 2011, **135**, 134303.
- 47 H. Köppel, J. Gronki and S. Mahapatra, *J. Chem. Phys.*, 2001, **115**, 2377–2388.
- 48 M. J. Frisch, G. W. Trucks, H. B. Schlegel, G. E. Scuseria, M. A. Robb, J. R. Cheeseman, G. Scalmani, V. Barone, B. Mennucci, G. A. Petersson, H. Nakatsuji, M. Caricato, X. Li, H. P. Hratchian, A. F. Izmaylov, J. Bloino, G. Zheng, J. L. Sonnenberg, M. Hada, M. Ehara, K. Toyota, R. Fukuda, J. Hasegawa, M. Ishida, T. Nakajima, Y. Honda, O. Kitao, H. Nakai, T. Vreven, J. A. Montgomery Jr., J. E. Peralta, F. Ogliaro, M. J. Bearpark, J. J. Heyd, E. Brothers, K. N. Kudin, V. N. Staroverov, T. Keith, R. Kobayashi, J. Normand, K. Raghavachari, A. Rendell, J. C. Burant, S. S. Iyengar, J. Tomasi, M. Cossi, N. Rega, J. M. Millam, M. Klene, J. E. Knox, J. B. Cross, V. Bakken, C. Adamo, J. Jaramillo, R. Gomperts, R. E. Stratmann, O. Yazyev, A. J. Austin, R. Cammi, C. Pomelli, J. W. Ochterski, R. L. Martin, K. Morokuma, G. Zakrzewski, G. A. Voth, P. Salvador, J. J. Dannenberg, S. Dapprich, A. D. Daniels, O. Farkas, J. B. Foresman, J. V. Ortiz, J. Cioslowski and D. J. Fox, *Gaussian 09, Revision C.01*; Gaussian, Inc.: Wallingford, CT, 2010.
- 49 T. Williams, C. Kelley, H.-B. Bröker and E. A. Merritt, *Gnuplot, Version 4.2*, 2007.

Chapter 6

Results and discussion

Hereinafter the principal results of the chapters 4 and 5 are summarized. The principal aim of this thesis is the theoretical modelling of ES, proposing new tools for searching MECI and new strategies to control fulvene photorotation. As stated in the objectives chapter, the thesis is clearly separated in two parts. For this reason, in this chapter, the results will be analysed separately in two different sections.

6.1 New Conical Intersection Optimization algorithm: Double Newton-Raphson

The first objective of the thesis is to obtain a new tool for studying ES: a new MECI algorithm. CIs are essential to understand the photochemical processes in ES. Finding the MECI is the first step in the study of the intersection seam and ES. For this goal, there are several algorithms. Nowadays, the most used one is the CG. But it is not the most efficient one. For this reason, the first objective is to improve the currently available algorithms, proposing a new MECI algorithm with a better approach to the seam.

Borrowing the ideas for reaching the degeneracy of CG (equation 2.43) and the composed step of CS (equation 2.45), DNR is conceived. DNR

is a double minimization of two functions,

$$f_1 = \varepsilon_{IS} \quad f_2 = (\Delta\varepsilon^2) \quad (6.1)$$

one for each MECI condition. Each function is optimized with the Newton-Raphson algorithm. Therefore, the total DNR step is the sum of the two optimization steps, as in the CS case, Δq_{IS} and Δq_{BS} . The steps are the following ones:

$$\Delta q_{IS} = -(\mathbb{H}_{IS})^{-1} g_{IS} \quad \Delta q_{BS} = -(\mathbb{H}_{BS})^{-1} g_{BS} \quad (6.2)$$

where Δq_{IS} has the same form and components as CS (equation 2.45) and the g_{BS} is borrowed from f penalty function of CG (equation 2.43),

$$g_{BS} = \frac{1}{|\mathbf{x}_1|} \nabla (\Delta\varepsilon^2) = 2\Delta\varepsilon^2 \hat{\mathbf{x}}_1 \quad (6.3)$$

where $\hat{\mathbf{x}}_1$ is the normalized \mathbf{x}_1 . Strictly, the g_{BS} does not have the normalization term, but in CG algorithm it improves the convergence. The Hessians, in both cases, are obtained with the BFGS update method with their respective gradients.

DNR has been implemented in a Gaussian Development Version program.⁷¹ Several points will be commented of this implementation. The first one is related with the coordinates of the system. A set of internal redundant coordinates is usually used in optimization, because it improves the number of optimization cycles. However, the gradients are usually calculated in Cartesian coordinates and they need to be projected (section 2.2.3). In projected gradient algorithms, the gradient is also projected. Unfortunately, the projection and transformation do not obey the commutative property. Therefore, the projected gradient and \mathbf{x}_1 are not orthogonal in redundant coordinates if the transformation is done after the projection, as shown by Equation 6.4.

$$(g_{IS}^{\text{cart}})^T \mathbf{x}_1^{\text{cart}} = g^{\text{red}} \mathbb{B}^T \mathbb{G}^{-T} \mathbb{G}^{-\mathbb{B}} \mathbf{x}_1^{\text{red}} \quad (6.4)$$

The $\mathbb{B}^T \mathbb{G}^{-T} \mathbb{G}^{-\mathbb{B}}$ should be the unitary matrix to retain the orthogonality of $g^{\text{red}} \mathbf{x}_1^{\text{red}}$ but it is not the case. The orthogonality between the

first order BS and the g_{IS} is basic in the projected gradient algorithms, for this reason the best option is to transform the BS modes and the gradient into redundant coordinates and do the projection in redundant coordinates. This incompatibility affects all projected gradient algorithms. For this reason all algorithms that are tested have been adopted with a correct implementation.

The second issue affects the IS Hessian. The IS Hessian (section 2.2.4) is obtained by BFGS update along the optimization with the projected gradient. In each step, it is projected to avoid that the N-R steps go along the BS modes. The resulting matrix has two zero eigenvalues corresponding to the directions of the BS. To avoid problems in the inversion of N-R, these eigenvalues are increased artificially, following the idea of ref.⁴² (equation 2.34).

$$\tilde{\mathbb{H}}_{IS} = \mathbb{P}\mathbb{H}_{IS}\mathbb{P} + \alpha(\mathbb{I} - \mathbb{P}) \quad (6.5)$$

Furthermore, the BS Hessian is characterized to have near zero eigenvalues. For this reason in our implementation of DNR, the eigenvalues smaller than $2 \cdot 10^{-4}$ are artificially increased with high values. The initial Hessians used in DNR are the initial parametrized diagonal Hessian of the Gaussian program.

Finally, there is a tendency for the first order BS vectors to mix near the degeneracy. The mixture of states when they are near in energy interchanges x_1 and x_2 , causing arbitrary changes in the direction of g_{BS} . These changes affect principally the updated BS Hessian and extend the effects along the optimization. A way to mitigate this problem is to switch from DNR to CS, using the CS as first order approximation of DNR. An energy criterion is used to switch the algorithms. We call the algorithms with the switch DNR-CS. This improvement of DNR produces important benefits in some examples, such as the MECI of azulene, shown in figure 6.1. In the figure, the evolution of the angles χ , the angle between the previous x_1 and the new one, is shown. In step 7, the angle changes its direction by approximately 75° , and the energy difference increases in the following step. In that point, the CS is activated in DNR-CS. This reduces the step number from 48 to 21, because the BS Hessian is updated with bad gradients from step 7.

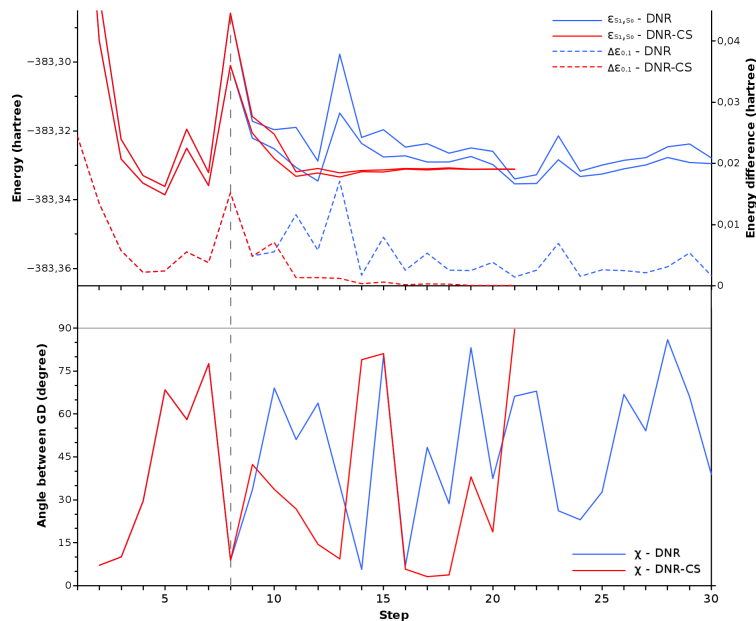


Figure 6.1: Course of MECI searches with DNR algorithms for azulene. Blue lines are pure DNR algorithm and red lines are the hybrid DNR-CS. In the top plot, the full lines are the energy of the GS and ES in fulvene in the optimization steps; hashed lines are the energy difference between the two states. In the second graph the χ angles between x_1 of the two consecutive steps are plotted.

A test-set of eleven well-know MECI, chosen from different works of the literature, is used in DNR-CS. The results were compared with the other two projected gradient algorithms, CG and CG-CS implemented in a Gaussian development version program by us. Our implementations of CG and CG-CS avoid the problem with redundant coordinates. The average results can be read in Table 6.1, where the average number of cycles and the average final energy difference is showed. Overall, the hybrid DNR-CS is the most efficient of the tested algorithms. It reaches the MECI in, approximately, 15% fewer steps than CG-CS and 30% than CG. CG-CS and DNR also obtain better convergence with respect the energy of the final point.

The averages give a clear message about the efficiency of each al-

Table 6.1: Averages of MECI searches with CG, CG-CS and DNR algorithms, including the distance from starting point, number of cycles and energy difference.

	Dist. [\AA] ^a	Method	Cycles	$\Delta\varepsilon[\text{a.u.}]^b$
Average	2.10	CG	41	-0.0000813
		CG-CS	29	-0.0000142
		DNR	23	-0.0000099

^a Distance in \AA from the starting point to the converged MECI geometry, calculated in Cartesian. ^b Energy difference between GS and ES ($\varepsilon_1 - \varepsilon_2$).

Table 6.2: Average of number of steps required to reach degeneracy threshold of 0.005 and 0.001 a.u. and the relative energy of S_1 with respect to the MECI for the eleven test cases, with DNR-CS, CG-CS and CG algorithms.

Method	Thres. 5.10^{-4} a.u.		Thres. 10^{-4} a.u.	
	Steps ^a	$\varepsilon_{rel}[\text{a.u.}]^b$	Steps ^a	$\varepsilon_{rel}[\text{a.u.}]^b$
CG	9	0.0383	5	0.0115
Average CG-CS	9	0.0387	5	0.0302
DNR	7	0.0381	6	0.0194

^a Optimization steps required to reach the energy degeneracy within given threshold. ^b Energy of ES at this point, relative to the MECI.

gorithm: DNR-CS algorithm obtains better degeneracy with fewer steps. Almost all cases follow the average result. For example, we plot the optimizations of acrolein and benzene, in figure 6.2. The MECI acrolein optimization (figure 6.2.a) is a clear example of the convergence problem of the CG algorithm, the default algorithm in Gaussian. The incorrect Hessian results in the loss of degeneracy in steps 32 and 43, and the energy difference is increased for several steps. On the other hand, CG-CS has some problems too in the final part of the optimization. CS is a first order approximation of the energy difference and, sometimes, this fact extends the number of steps for reaching the degeneracy. The benzene example (figure 6.2.b) shows that the approach to the seam of DNR is more efficient than the CG and, thus, it converges in only 16 steps with smaller absolute energy.

In this case, CG and CG-CS have a similar convergence because they share the major part of the optimization.

The better approach to the seam is illustrated in table 6.2. In the table, the average of cycles required to reach the different levels of degeneracy, 0.005 a.u. and 0.001 a.u., are presented with the energy of ES relative to the MECI. The first one is the energy gap where the CG-CS algorithm switches from CG to CS, so the value is the same. On average, DNR-CS can reach the energy gap 0.005 earlier than CG (and CG-CS), with 2 steps of difference. The smaller energy gap is reached in the same number of steps by DNR-CS and CG-CS, but the relative energy of DNR-CS is lower: it is closer to the MECI. Overall, this data shows the better efficiency of the DNR-CS algorithm.

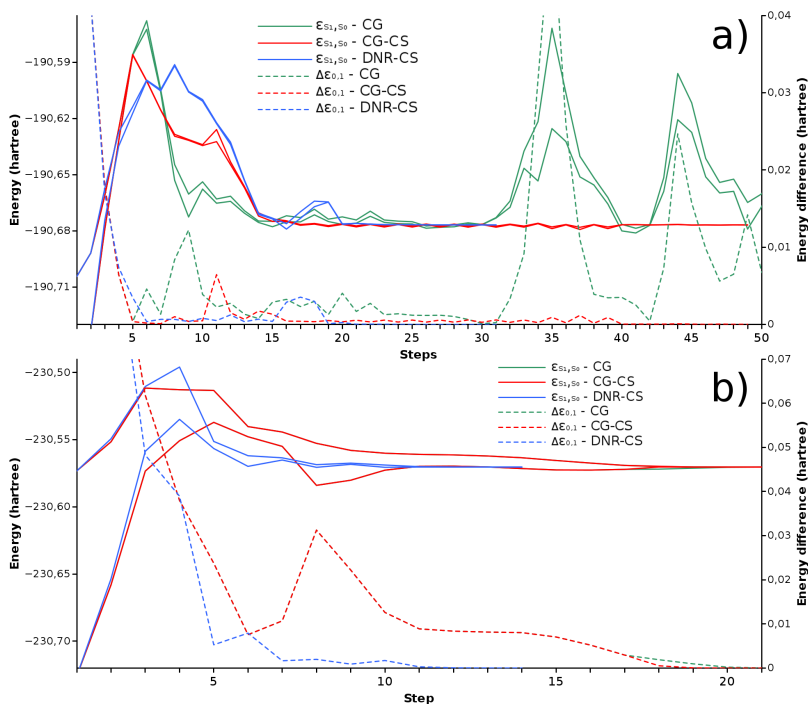


Figure 6.2: Energies of ES and GS (full lines, left axis) and energy difference (dashed lines, right axis) in steps of the MECI optimization of acrolein (a) and benzene (b) with CG, CG-CS and DNR-CS algorithms. Energies are in hartrees

6.1.1 MECI optimization algorithm inside ONIOM Scheme

Finding MECI in a fully quantum calculations was solved in the previous section. However, large systems, such as crystals, proteins or DNA, are usually out of reach for the *ab initio* calculations. For these cases, hybrid methods, such as ONIOM, are an alternative for obtaining the potential energy of the systems when the excitation is localized in a small fragment. For this reason, the adaptation of MECI algorithms inside hybrid methods is important. In this direction, Bearpark and co-workers⁷² implemented the CG algorithm inside the ONIOM scheme.

Following the steps of this CG implementation, one of the objectives of the thesis is to adapt the three projected gradient algorithms in ME-ONIOM scheme and combine it with microiterations (see section 2.3.3 for more information).

Using the ONIOM excited state approximation, the first order BS vectors can be obtained from the high level calculation:

$$\mathbf{x}_1^{ONIOM} = (\mathbf{x}_1)_{model}^{High} J \quad (6.6)$$

$$\mathbf{x}_2^{ONIOM} = (\mathbf{x}_2)_{model}^{High} J \quad (6.7)$$

where J is the Jacobian transformation, needed if there are LA in the model. Thus, the gradient of the IS from two states can be obtained using the projector built with the ONIOM BS vectors.

$$g_{IS}^{ONIOM} = \mathbf{P}^{ONIOM} g_j^{ONIOM} = \mathbf{P}^{ONIOM} g_i^{ONIOM} \quad (6.8)$$

Therefore, the formulation of the three algorithms does not change practically. The steps of the three methods are the following ones:

ONIOM CG:

$$\Delta q_{CG}^{ONIOM} = \mathbb{H}^{-1} \left(g_{IS}^{ONIOM} + 2(\Delta \varepsilon)_{model}^{high} \mathbf{x}_1^{ONIOM} \frac{1}{|\mathbf{x}_1^{ONIOM}|} \right) \quad (6.9)$$

ONIOM CS:

$$\begin{aligned}\Delta q_{IS,CS}^{ONIOM} &= \mathbb{H}_{IS}^{-1} g_{IS}^{ONIOM} \\ \Delta q_{BS,CS}^{ONIOM} &= \Delta \varepsilon_{model}^{high} \frac{1}{|x_1^{ONIOM}|^2} x_1^{ONIOM}\end{aligned}\quad (6.10)$$

ONIOM DNR:

$$\begin{aligned}\Delta q_{IS,CS}^{ONIOM} &= \mathbb{H}_{IS}^{-1} g_{IS}^{ONIOM} \\ \Delta q_{BS,CS}^{ONIOM} &= 2\mathbb{H}_{BS}^{-1} \left((\Delta \varepsilon)_{model}^{high} x_1^{ONIOM} \frac{1}{|x_1^{ONIOM}|} \right)\end{aligned}\quad (6.11)$$

The three projected gradient algorithms inside ME-ONIOM have been implemented in the Gaussian development Version program, following the previous equation steps. All implementation issues commented in the previous sections have been applied. Microiterations have been implemented too for the three algorithms. Within ME-ONIOM and following the ONIOM excited state approximation, the low level steps do not affect the CI conditions and the microiteration scheme can be applied in the following straightforward formula, where the microiteration steps are a simple minimization.

$$\Delta q_{MECI}^{ONIOM} = \begin{pmatrix} \Delta q_{model}^{MECI} \\ 0 \end{pmatrix} + \begin{pmatrix} 0 \\ \sum \Delta q_{rest}^{min} \end{pmatrix}\quad (6.12)$$

First of all, a test set of eighteen molecules was used in the three algorithms with microiterations. Three model systems are used and some

Table 6.3: Averages of number of cycles of MECI searches with CG, CG-CS and DNR algorithms inside ME-ONIOM with 18 systems.

Method	Average
CG	28
CG-CS	26
DNR-CS	28

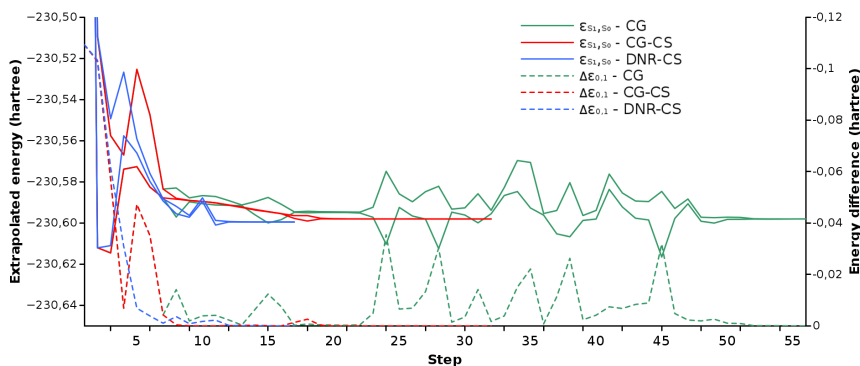


Figure 6.3: Course of MECI searches with CG, CG-CS and DNR-CS algorithms for tritert-butylfulvene. Full lines are the energy of the two states and hashed lines is the energy difference. Energies in hartree.

substituents in the low level layer are added for forming seventeen different molecules. The last test molecule is Pro-Vitamin D, used in the previous ONIOM MECI algorithm implementation.⁷² The average results can be read in the table 6.3. In contrast with fully quantum calculations, there is not an optimal algorithm. There are several cases where DNR-CS presents some problems and other cases when it is the most efficient algorithm. These two kinds of cases are discussed with the figures 6.3 and 6.4, where the extrapolated energy profiles during the optimization of tritert-butylfulvene and hexaphenylbutadiene with the different algorithms are plotted. In figure 6.3, DNR-CS reaches the degeneracy faster than the other algorithms and obtains the MECI in less cycles, whereas CG loses the degeneracy several times. The DNR-CS problem is presented in figure 6.4. During the approach to the seam, the extrapolated energy of the DNR-CS optimization increases by 0.8 hartree. This increase is consequence of a series of consecutive large BS steps. The BS step does not consider the low-level atoms (equation 6.11) and can cause close contacts between them, increasing the energy. This energy problem affects specially the LAH because they are only optimized by macroiteration steps but they have an important energy contribution of the low level calculation. To illustrate

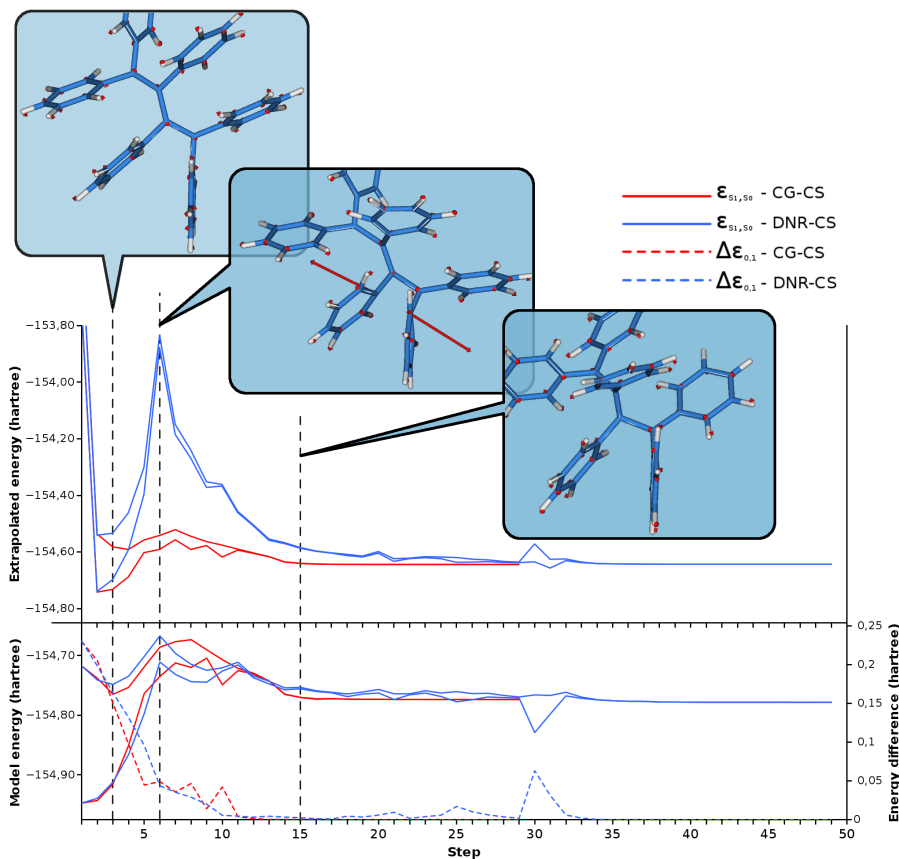


Figure 6.4: Course of MECI searches with CG-CS and DNR-CS algorithms for hexaphenylbutadiene. The structures are from DNR-CS and the red vectors are the forces each point. Full lines are the extrapolated and QM model energy in each step, and dashed is the energy difference. Energies in hartree.

this point, the structures and the ONIOM forces of the excited state ($-g_{ES}^{ONIOM}$) of steps 3, 6, and 15 are shown in figure 6.4. In the maximum of the extrapolated energy, step 6, two LAH are in close contact and they have very large forces. This problem is especially important in cases with big substituents in the link atoms (phenyl derivatives) or cyclic systems (Pro-vitamin D). In the CG algorithm, this problem is not so important because the steps take also the gradient of the real

Table 6.4: Relative energy of the critical points of DPDBF inside the totally frozen crystal cage, with respect to the minimum. Values in eV.

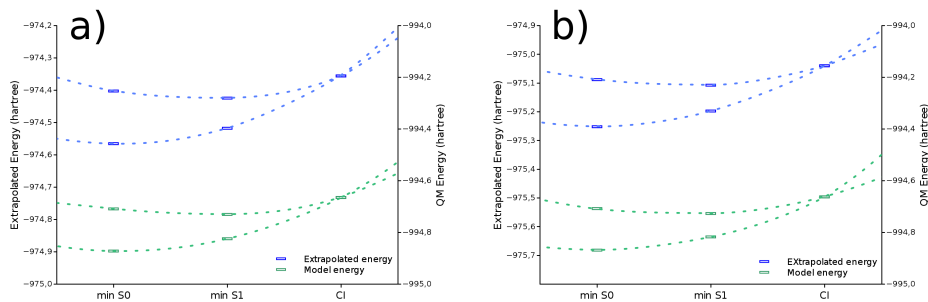
Structure	Model Energy		Extrapol. Energy	
	S_0	S_1	S_0	S_1
Minimum S_0	0.0000	4.4196	0.0000	4.4196
Minimum S_1	1.2748	3.8279	1.2901	3.8435
MECI	5.6150	5.6151	5.7052	5.7053

Table 6.5: Relative energy of the critical points of the DPDBF inside crystal cage with one free solvation layer, with respect to the minimum. Values in eV

Structure	Model Energy		Extrapol. Energy	
	S_0	S_1	S_0	S_1
Minimum S_0	0.0000	4.3913	0.0000	4.3913
Minimum S_1	1.4144	3.8648	1.2901	3.9417
MECI	5.6307	5.6311	5.7052	5.7805

system into account.

The second part of the test is to show the potential of this implementation. The critical points for the radiationless deactivation, ground and excited state minima and the MECI, of the diphenyl dibenzofulvene (DPDBF) inside its own crystal are calculated. DPDBF presents an interesting property: the molecule is fluorescent in crystal form

**Figure 6.5:** Energy profile of GS and first ES of DPDBF inside its own crystal, with totally frozen crystal (a) and free first layer (b). Energies in hartree.

but not in solution, where there is an energetically accessible CI.⁷³ The partial charges of this system are small so the ME scheme can be applied safely. Two kinds of environments are used to calculate the critical points: first, a totally frozen cage, where the crystal environment cannot move; and, second, with a free solvation layer where the first layer of molecules that surround the model are allowed to relax. The energy profiles are shown in figure 6.5 and the relative energy of the critical points are in tables 6.4 and 6.5. In both cases, the MECI is found with the DNR-CS algorithm. The main difference between the two environments is the relaxation energy of the free solvation layer, about 0.68 a.u. of stabilization energy. This difference is produced by small changes from the crystal structure to the UFF stable structure, distributed in all bonds. There is also a small difference in the relative energy of the minimum of S_1 , but in this case, it is somewhat counterintuitive because one may expect that the unfrozen environment stabilizes the distorted structure of S_1 . This probably indicates that the crystal cannot adapt to the changes of the model in the excited state with the UFF method.

6.2 Photophysics under Stark effect

The second big aim of the thesis is the application of the PES studies for obtaining new control strategies in photochemistry, the direct application of the last section, where new tools for studying PES were obtained.

In this section, a new non-resonant Stark effect control strategy for fulvene photorotation is proposed. In recent years, the control was achieved using a non-resonant field. An electric field shifts PES through the Stark effect.^{74,75} However, intense fields are necessary for obtaining the relevant effect and only electromagnetic radiation can reach these intensities. For this reason, this kind of control is known as non-resonant dynamic Stark effect (NRDSE) control. Experimentally, the most successful example of control using NRDSE is the photodissociation of IBr, where an infrared laser can change the probabilities

of different reaction channels.⁷⁴ From the point of view of the theory, several studies have achieved control in diatomic molecules^{76–79} or, most recently, in polyatomic ones.^{80,81}

A new control strategy using NRDSE is developed in this section. We aim to simulate the control of the lifetime of fulvene using NRDSE, preceded by resonant excitation. Thus, two laser pulses are used for controlling fulvene. Fulvene and their photophysics have been studied extensively. In the introduction chapter (section 1.2.2), the most important features of fulvene photophysics are discussed, such as the principal modes in fulvene photo-deactivation, the decay ways or the electronic states involved. The radiation absorption process leads to a non-stationary state. TDSE needs to be solved for simulating the photophysics of fulvene and its control correctly. MCTDH is the most efficient way to solve the TDSE (section 2.4.1). However, MCTDH cannot consider all modes of fulvene. For this reason, the simulations were carried out in a two state 4D model previously used,²⁷ where the four dimensions are the principal modes described in the Introduction (section 1.2.2) and the two states are S_0 and S_1 . Thus, the TDSE of this model system is the following.

$$i\hbar \frac{\partial}{\partial t} \begin{pmatrix} \psi_1(q, t) \\ \psi_2(q, t) \end{pmatrix} = \hat{H} \begin{pmatrix} \psi_1(q, t) \\ \psi_2(q, t) \end{pmatrix} \quad (6.13)$$

where $\psi_1(q, t)$ and $\psi_2(q, t)$ are the time-dependent nuclear wave function of S_0 and S_1 electronic state of fulvene. They depend on the time (t) and the four spatial dimensions ($q = \{Q_{x1}, Q_{x2}, \varphi, \theta\}$). The energy operator (\hat{H}) is divided in three terms.

$$\hat{H} = \hat{T} + \hat{W} + \hat{H}_{int} \quad (6.14)$$

where \hat{T} is the kinetic energy operator for the four dimensions, \hat{W} is the diabatic potential energy of the nucleus and \hat{H}_{int} describes the interaction between the system and external fields. In this system, there are two kinds of interactions: resonant (\hat{H}_{int}^{res}) and non-resonant (\hat{H}_{int}^{n-res}). The resonant interaction operator uses the first order approximation and, thus, it is based on the dipole transition moment. It

has the following form:

$$\hat{H}_{int}^{res} = \begin{pmatrix} 0 & \mu_{12}\epsilon^{res}(t) \\ \mu_{12}\epsilon^{res}(t) & 0 \end{pmatrix} \quad (6.15)$$

where $\epsilon^{res}(t)$ is the resonant field function. Our model assumes that the system is aligned with respect to the fields during the propagation. The non-resonant interaction operator is basically the Stark effect and modifies the potential energy, so the form of the matrix operator is:

$$\hat{H}_{int}^{n-res} = \begin{pmatrix} \hat{H}_{11}^{n-res}(q, \epsilon) & 0 \\ 0 & \hat{H}_{22}^{n-res}(q, \epsilon) \end{pmatrix} \quad (6.16)$$

where the components depend on the ϵ , the non-resonant field. Each state has its own Stark effect. We assume that the couplings are independent from the resonant field, so the non-diagonal terms of \hat{H}_{int}^{n-res} are zero. On the other hand, we define a new field-dependent potential operator:

$$\hat{V}(q, \epsilon) = \hat{W}(q) + \hat{H}_{int}^{n-res}(q, \epsilon) \quad (6.17)$$

This new operator substitutes the potential energy and non-resonant interaction operators and simplifies the parametrization problem.

6.2.1 Parametrization

To carry out quantum dynamics it is necessary to obtain the potential matrix function (\hat{W}), in our model, \hat{V} . As the real form is unknown, this matrix needs to be parametrized and fitted with *ab initio* calculations in different positions and fields. The following form is proposed for the matrix operator \hat{V} :

$$\hat{V}(q, \epsilon) = V^0\mathbb{I} + \begin{pmatrix} V_{11}(q, \epsilon) & V_{12}(q) \\ V_{12}(q) & -V_{11}(q, \epsilon) \end{pmatrix} \quad (6.18)$$

where the terms of the matrix are similar to the field free potential (\hat{W}), previously used.²⁷ These terms form a Taylor expansion along the four

coordinates centred at the CI_{plan} . But, in this case, the Q_{x1} and φ parameters of the expansion are re-expanded in function of the field.

$$par(\epsilon) = par_0 + \mu_{par}\epsilon + \frac{\alpha_{par}}{2}\epsilon^2 \quad (6.19)$$

Therefore, the dipole moments and polarizabilities are included inside the parameters (total dipole moment and polarizabilities of the system are not calculated explicitly), obtaining a set of 34 parameters. The field dependent terms along Q_{x2} and θ are neglected for simplicity. In practice, we assume that the Stark effect produces a constant shift along this coordinates. Finally, we only consider the zz components of the polarizability.

The parameters are fitted to *ab initio* calculations, carried out at the CASSCF(6,6)/cc-pvdz level. This level is sufficient for describing correctly the ES. Furthermore, the states S_0 and S_1 have A and B symmetry, respectively, and they can be used as diabatic potential energy directly from the *ab initio* calculations. The fitting includes points with non-resonant field in the range of ± 0.04 a.u. However, at strong fields, S_2 is close in energy and interferes with the other states. In these cases, these points are discarded. Thus, the set of parameters are fitted with 13385 points using the nonlinear least-squares Marquardt-Levenberg algorithm implemented in gnuplot⁸² to obtain the matrix potential energy. The root mean square of residuals is 0.0024 a.u. for V_0 and 0.0032 a.u. for V_{11} . The good agreement between *ab initio* and the model energy is showed in figure 6.6, where *ab initio* and fitted model energies profiles along Q_{x1} are plotted.

The same figure shows that the Stark effect modifies differently the energies of the FC and the CI_{plan} . The difference between them is increased with the non-resonant external field until -0.04a.u., where the CI_{plan} lies 1.56 eV higher in energy than FC vertical excitation. Therefore, the main decay of ES of fulvene is shifted with the field. We can predict that the main decay path can be deactivated with the field and it makes possible the activation of the other decay path, such as rotation. Thus, fulvene photorotation can be controlled.

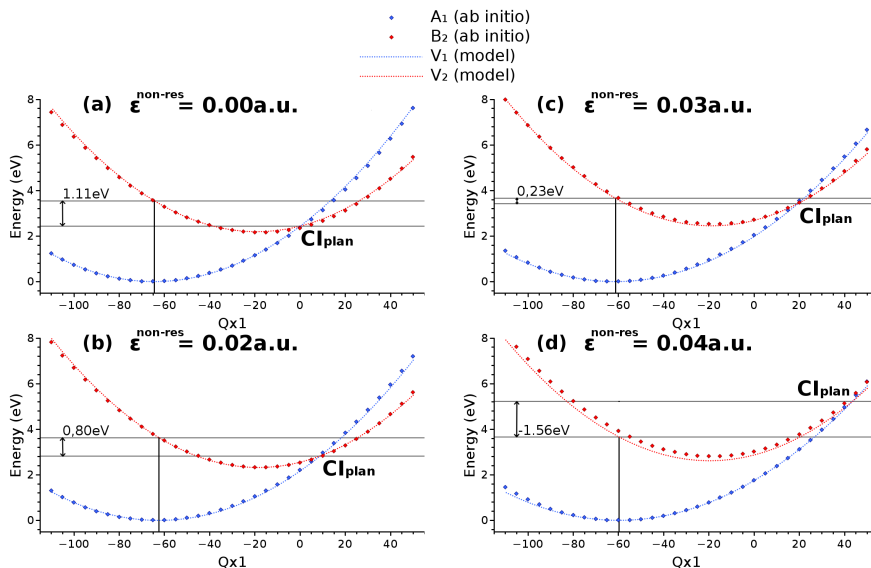


Figure 6.6: Energy profile along Q_{x1} at different non-resonant field intensities, including energy difference between the vertical excitation and the CI_{plan} . Dots are the *ab initio* energies of the A and B states. Dashed lines are the energies of the model. Q_{x1} displacements in mass-weighted atomic units, energies in eV.

6.2.2 Quantum dynamic simulations

We used the MCTDH package⁶⁹ to propagate the system over 150 fs. The propagation starts in an initial relaxed system, in the electronic and vibrational ground state. At the beginning of the propagation, for 5fs, the pulse with the following form excites the system:

$$\epsilon^{res}(t) = \epsilon_0^{res} \cos(\omega^{res} t) \sin^2\left(\frac{\pi}{\tau} t\right) \quad (6.20)$$

where ϵ_0^{res} was set to 0.10 a.u., $\hbar\omega^{res}$ is the excitation energy (3.6eV) and τ is the pulse duration (5fs).

Propagations under static non-resonant fields

To understand the effects of the external field on the dynamics, we started the study with a set of propagations with a constant(static) field of various strengths.

$$\epsilon(t) = \epsilon_0 \quad (6.21)$$

In figure 6.7 are plotted the propagations of 0.00, -0.02, -0.03 and -0.04 a.u.. During the resonant pulse (5fs) the population of S_1 rises from 0 to a maximum value (approximately 0.4). In the first three propagations population decay quickly to ground state in the first 20 fs. However, there are some differences between them: when the field is applied, the initial decay becomes more efficient. This result is somewhat counterintuitive since the CI_{plan} , the main decay way, is increasing in energy with the field. However, the result can be understood in terms of Fermi's Golden Rule (section 1.1.1). The overlap increases when the vertical excitation get close at CI_{plan} , thus the transition rate increases. It becomes maximum when these two values are the same, at -0.03 a.u., approximately.

With -0.04a.u. field, the situation is reversed and the decay is slower. The population remains in S_1 after 20 fs and it takes 45 fs to decay to half this value. In this case, the CI_{plan} is high in energy from FC point and fulvene cannot reach that region. the time to decay to S_0 in this

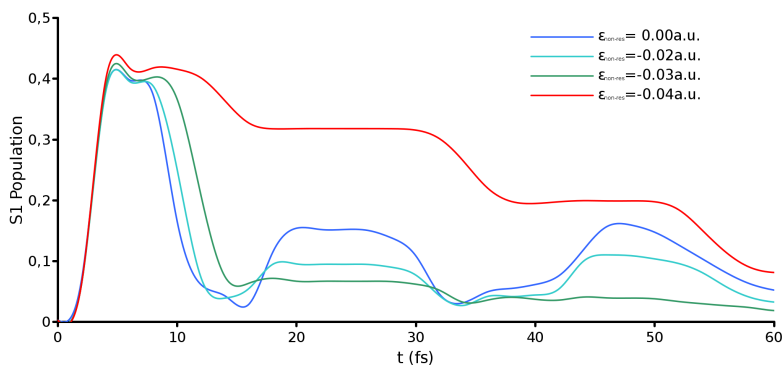


Figure 6.7: S_1 population for the propagations with static electric field of different intensity.

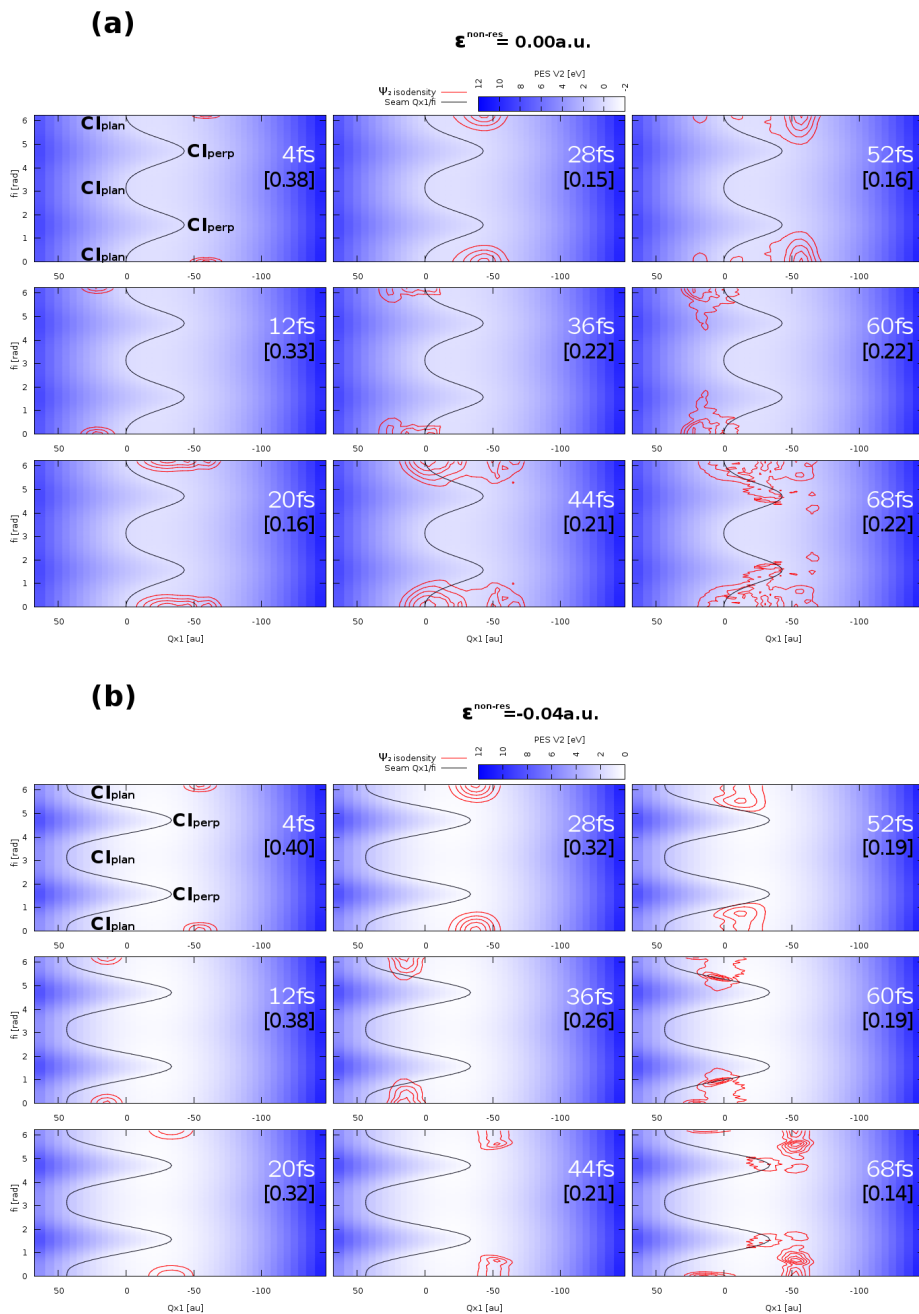


Figure 6.8: Snapshots of the wave packet propagations on the V_2 surface along the Q_{x1} and φ coordinates, displaying the time and the population of V_2 . Propagations carried out (a) without non-resonant field and (b) with a static non-resonant field of -0.04a.u. Wave packet density is plotted in red and the seam position in black.

case is in agreement with the time necessary for IVR from reference,²⁷ the calculated time to activate the φ rotation mode.

To illustrate this point, figure 6.8 shows the evolution of the wavepacket in the diabatic excited state, V_2 , in the field-free case and under -0.04 a.u. field for several snapshots. The wave packet isodensity and the seam are plotted. The population of V_2 is displayed in every snapshots. In the field free case, the wave packet has traversed the planar region of the seam twice in 20 fs. For this reason, the population of V_2 decays from 0.38 to 0.16. In contrast, in -0.04 field case, the main part of the wave packet does not reach the planar seam in the first 20 fs. In consequence, its population practically does not decay. The populations start to decay in 36 fs, when the wave packet can reach the non-planar region of the seam.

Propagations under dynamic non-resonant fields

A realistic simulation requires the use of a dynamic non-resonant field because lasers are the unique way to achieve the necessary field strengths. Thus, we performed simulations where the non-resonant field changes with the time.

$$\epsilon(t) = -\epsilon_0 \sin(\omega t) \quad (6.22)$$

The dynamic Stark control is done by a laser of wave length of 1239 nm. This pulse starts before the simulation and never stops. The results of these control simulations with NRDSE are shown in figure 6.9. We carry out propagations with ϵ_0 values of 0.04a.u., 0.06a.u. and 0.08a.u. because we estimated that the field needs the double strength to obtain the same results of static fields. This is partially true. The 0.08 a.u. case obtains similar results to the -0.04 static external field, but the estimation fails in the other two. In these cases, a rapid decay is not seen and an increase of the lifetime of V_2 is shown.

Therefore, our model simulations shows that it is possible to control the fulvene photorotation with NRDSE, changing the lifetime of ES. A further possibility of control would be given modulating the phase between the two lasers, which we have not explored yet. However,

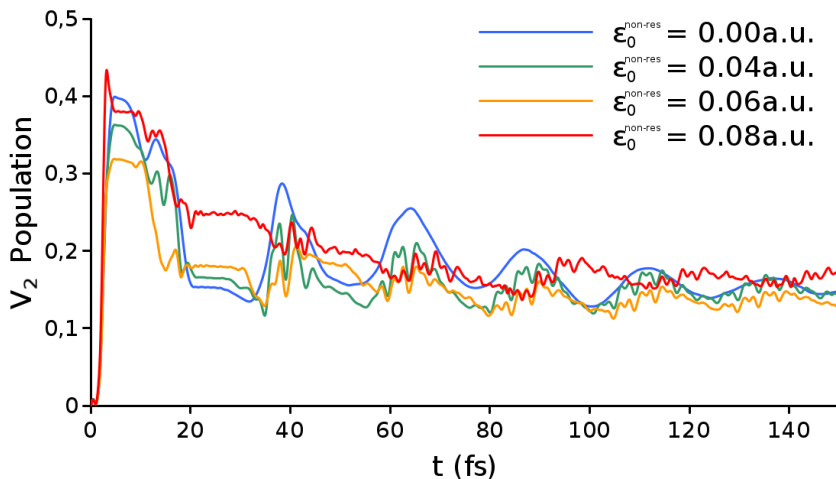


Figure 6.9: V_2 population for the propagations with dynamic non-resonant electric field of different intensity.

our approach has some limitations. The first one is the dimensionality of the model. Our model captures the principal behaviour of the fulvene decay, because this process is very fast and the excitation energy is concentrated in only a few modes. However, the inclusion of more modes must improve the connection between the model and reality.⁸³ The inclusion of the Stark effect in only two dimensions can be improved, however the Stark shifts affect principally the Q_{x1} and φ coordinates. Another limitation of the model is that only two states are included. More states should be included because S_2 interferes at fields larger than to 0.02 a.u.. Finally, really strong fields ($4.5 \cdot 10^{14}$ W cm⁻²) were needed to achieve the control. In practice, such power densities cause ionization. For this reason, it makes the experimental implementation of this control scheme in fulvene challenging. To carry out the control experimentally, it is necessary to find systems where the polarizabilities of the two states differ more substantially than in fulvene.

Chapter 7

Conclusions

The main conclusions of this thesis are collected in this chapter and briefly summarized.

In the first part of the thesis, starting from the existing MECI projected gradient algorithms, CG and CG-CS, a new CI algorithm optimization was devised to improve the approach to the seam, called DNR-CS. The DNR step is composed of two N-R steps, one for each space, IS and BS. The IS step minimizes the energy in the IS and BS step leads to the degeneracy. Each step has a separate Hessian that is updated for each cycle. The use of the IS Hessian avoids losing the degeneracy. On the other hand, the BS Hessian improves the approach to the seam with respect to CG, because the Hessian takes the second order degeneracy lifting effects into account. However, the mixture of the states in the degeneracy interchanges the x_1 and x_2 vectors and the BS Hessian can be affected by this fact. For this reason, CS is used when the BS Hessian becomes ill-defined, in the hybrid DNR-CS algorithm.

The projected gradient algorithms, DNR-CS, CG-CS and CG, were compared with a test set of eleven compounds with well-know MECI. Our comparison shows that the new DNR-CS is the most efficient algorithm because it reduces the number of optimization cycles. In all cases, DNR-CS obtains the global MECI. Moreover, the degeneracy is

reached with less steps than the two other algorithms and the energy is closer to the MECI.

In the second part of this thesis, the three projected gradient CI optimization algorithms were implemented inside the ONIOM scheme. The implementation is done using the ONIOM excited state approximation, where the MECI optimization steps do not have any important change in ONIOM. Within ME-ONIOM and following this approximation, the microiterations were also implemented in a straightforward way.

A test set is used to compare the behaviour of the three algorithms in the ONIOM scheme. On average, the algorithms have the same efficiency. The DNR-CS algorithm presents problems with bulky substituents in the LA, being the CG-CS algorithm the preferable option in these cases. In the remaining cases, the DNR-CS algorithm has a good performance.

The potential of our implementation to locate MECI in crystals of organic molecules, where the excitation is centred on a single molecule, is shown for the case of DPDBF.

Finally, in the last part of this thesis, a new strategy for the control of the photorotation of fulvene has been proposed. Using the existing knowledge of the decay mechanism, we proposed a new strategy based on the NRDSE, where two lasers were used, one for exciting the molecule and the other one for inducing the Stark effect with a non-resonant electric field that shifts the PES.

Starting with a previously used 4D model, a new model system that includes the external field was proposed. The new model system was used to simulate the new control strategy with quantum dynamic simulations.

The simulations of the new control strategy were done, where two lasers are used to control the fulvene photorotation. Simulations with different fields showed that it is possible to increase the lifetime of the first ES from 10 to 40 fs, with a dynamic electric field. However, strong fields (0.08 a.u.) were needed to achieve a satisfactory control.

Bibliography

- 1 Hilborn, R. C. *arXiv preprint physics/0202029* **2002**,
- 2 Klessinger, M.; Michl, J. **1995**,
- 3 Born, M.; Oppenheimer, R. *Annalen der Physik* **1927**, *389*, 457–484.
- 4 Franck, J.; Dymond, E. G. *Trans. Faraday Soc.* **1926**, *21*, 536–542.
- 5 Condon, E. *Phys. Rev.* **1926**, *28*, 1182–1201.
- 6 Fermi, E. *Nuclear Physics.*; University of Chicago Press, 1950.
- 7 Dirac, P. A. M. *Royal Society of London Proceedings Series A* **1927**, *114*, 243–265.
- 8 Teller, E. *Journal of Physical Chemistry* **1937**, *41*, 109–116.
- 9 Asturiol, D.; Lasorne, B.; Worth, G. A.; Robb, M. A.; Blancafort, L. *Phys. Chem. Chem. Phys.* **2010**, *12*, 4949–4958.
- 10 Bender, C. F.; Dunning Jr, T. H.; Schaefer III, H. F.; Goddard III, W. A.; Hunt, W. J. *Chemical Physics Letters* **1972**, *15*, 171–178.
- 11 Ben-Nun, M.; Martinez, T. J. *Chemical physics letters* **1998**, *298*, 57–65.
- 12 Quenneville, J.; Martinez, T. J. *The Journal of Physical Chemistry A* **2003**, *107*, 829–837.

- 13 Petrongolo, C.; Buenker, R. J.; Peyerimhoff, S. D. *The Journal of Chemical Physics* **1982**, *76*, 3655–3667.
- 14 Merer, A.; Mulliken, R. S. *Chemical Reviews* **1969**, *69*, 639–656.
- 15 Snyder, P.; Schatz, P.; Rowe, E. *Chemical physics letters* **1984**, *110*, 508–512.
- 16 RicHard-59(wikipedia.org), Retinal Cis and Trans. 2012; <http://commons.wikimedia.org/wiki/File:RetinalCisandTrans.svg>, Creative Commons Attribution-Share.
- 17 Yoshizawa, T.; Wald, G. **1963**,
- 18 Migani, A.; Robb, M. A.; Olivucci, M. *Journal of the American Chemical Society* **2003**, *125*, 2804–2808.
- 19 Polli, D.; Altoè, P.; Weingart, O.; Spillane, K. M.; Manzoni, C.; Brida, D.; Tomasello, G.; Orlandi, G.; Kukura, P.; Mathies, R. A. *Nature* **2010**, *467*, 440–443.
- 20 Domaille, P.; Kent, L.; O'Dwyer, M. *Chemical Physics* **1974**, *6*, 66–75.
- 21 Kent, J. E.; Harman, P. J.; O'Dwyer, M. F. *The Journal of Physical Chemistry* **1981**, *85*, 2726–2730.
- 22 Asmis, K. R.; Allan, M.; Schafer, O.; Fülcher, M. *The Journal of Physical Chemistry A* **1997**, *101*, 2089–2095.
- 23 Sicilia, F.; Bearpark, M. J.; Blancafort, L.; Robb, M. A. *Theoretical Chemistry Accounts* **2007**, *118*, 241–251.
- 24 Dreyer, J.; Klessinger, M. *The Journal of chemical physics* **1994**, *101*, 10655–10665.
- 25 Bearpark, M. J.; Bernardi, F.; Olivucci, M.; Robb, M. A.; Smith, B. R. *Journal of the American Chemical Society* **1996**, *118*, 5254–5260.

- 26 Mendive-Tapia, D.; Lasorne, B.; Worth, G. A.; Robb, M. A.; Bearpark, M. J. *The Journal of chemical physics* **2012**, *137*, 22A548.
- 27 Blancafort, L.; Gatti, F.; Meyer, H.-D. *The Journal of chemical physics* **2011**, *135*, 134303.
- 28 Szabo, A.; S. Ostlund, N. *Modern Quantum Chemistry*; Dover Publications, INC., 1982.
- 29 Skodje, R. T.; Truhlar, D. G.; Garrett, B. C. *The Journal of Chemical Physics* **1982**, *77*, 5955–5976.
- 30 Billing, G. D.; Mikkelsen, K. V.; Truhlar, D. G. *Physics Today* **1996**, *49*, 74.
- 31 Baer, M.; Billing, G. D. *Advances in Chemical Physics, The Role of Degenerate States in Chemistry*; John Wiley & Sons, 2003; Vol. 124.
- 32 Fletcher, R. *Practical methods of optimization*; John Wiley & Sons, 2013.
- 33 Schlegel, H. B. *Wiley Interdisciplinary Reviews: Computational Molecular Science* **2011**, *1*, 790–809.
- 34 Murtagh, B. A.; Sargent, R. W. H. *Computer Journal* **1972**, *13*, 185–194.
- 35 Broyden, C. *J. Inst. Math. Appl.* **1970**, *6*, 76–90.
- 36 Fletcher, R. *Comput Journal* **1970**, *13*, 317–322.
- 37 Goldfarb, D. *Math. Comput.* **1970**, *24*, 23–26.
- 38 Shanno, D. *Math. Comput.* **1970**, *24*, 647–657.
- 39 Fletcher, R.; Powell, M. J. *The Computer Journal* **1963**, *6*, 163–168.

- 40 Bofill, J. M. *Journal of Computational Chemistry* **1994**, *15*, 1–11.
- 41 Hehre, W.; Radom, L.; Schleyer, P.; Pople, J. *Ab Initio Molecular Orbital Theory*; New York: John Wiley Sons, 1986.
- 42 Peng, C.; Ayala, P. Y.; Schlegel, H. B.; Frisch, M. J. *Journal of Computational Chemistry* **1996**, *17*, 49–56.
- 43 Pulay, P.; Fogarasi, G.; Pang, F.; Boggs, J. E. *Journal of the American Chemical Society* **1979**, *101*, 2550–2560.
- 44 Pulay, P.; Fogarasi, G. *The Journal of chemical physics* **1992**, *96*, 2856.
- 45 Frisch, M. J. et al. Gaussian 09 Revision D.01. Gaussian Inc. Wallingford CT 2009.
- 46 Manaa, M. R.; Yarkony, D. R. *The Journal of chemical physics* **1993**, *99*, 5251.
- 47 Ciminelli, C.; Granucci, G.; Persico, M. *Chemistry – A European Journal* **2004**, *10*, 2327–2341.
- 48 Bearpark, M. J.; Robb, M. A.; Bernhard Schlegel, H. *Chemical physics letters* **1994**, *223*, 269–274.
- 49 Sicilia, F.; Blancafort, L.; Bearpark, M. J.; Robb, M. A. *Journal of Chemical Theory and Computation* **2008**, *4*, 257–266.
- 50 Anglada, J. M.; Bofill, J. M. *Journal of Computational Chemistry* **1997**, *18*, 992–1003.
- 51 Roothaan, C. C. J. *Reviews of modern physics* **1951**, *23*, 69.
- 52 Schmidt, M. W.; Gordon, M. S. *Annual review of physical chemistry* **1998**, *49*, 233–266.
- 53 Roos, B. O. *Advances in Chemical Physics: Ab Initio Methods in Quantum Chemistry Part 2, Volume 69* **1987**, 399–445.

- 54 Andersson, K.; Malmqvist, P. A.; Roos, B. O. *J. Chem. Phys* **1992**, *96*, 1218.
- 55 Andersson, K.; Malmqvist, P. A.; Roos, B. O.; Sadlej, A. J.; Wolinski, K. *Journal of Physical Chemistry* **1990**, *94*, 5483–5488.
- 56 Rappé, A. K.; Casewit, C. J.; Colwell, K.; Goddard Iii, W.; Skiff, W. *Journal of the American Chemical Society* **1992**, *114*, 10024–10035.
- 57 Svensson, M.; Humbel, S.; Froese, R. D.; Matsubara, T.; Sieber, S.; Morokuma, K. *The Journal of Physical Chemistry* **1996**, *100*, 19357–19363.
- 58 Dapprich, S.; Komáromi, I.; Byun, K. S.; Morokuma, K.; Frisch, M. J. *Journal of Molecular Structure: THEOCHEM* **1999**, *461*, 1–21.
- 59 Morokuma, K.; Wang, Q.; Vreven, T. *Journal of chemical theory and computation* **2006**, *2*, 1317–1324.
- 60 Vreven, T.; Morokuma, K.; Farkas, Ö.; Schlegel, H. B.; Frisch, M. J. *Journal of computational chemistry* **2003**, *24*, 760–769.
- 61 Vreven, T.; Byun, K. S.; Komáromi, I.; Dapprich, S.; Montgomery, J. A.; Morokuma, K.; Frisch, M. J. *Journal of Chemical Theory and Computation* **2006**, *2*, 815–826.
- 62 Chung, L. W.; Hirao, H.; Li, X.; Morokuma, K. *Wiley Interdisciplinary Reviews: Computational Molecular Science* **2012**, *2*, 327–350.
- 63 Hratchian, H. P.; Parandekar, P. V.; Raghavachari, K.; Frisch, M. J.; Vreven, T. *The Journal of chemical physics* **2008**, *128*, 034107.

- 64 Murphy, R. B.; Philipp, D. M.; Friesner, R. A. *Journal of Computational Chemistry* **2000**, *21*, 1442–1457.
- 65 Bearpark, M. J.; Ogliaro, F.; Vreven, T.; Boggio-Pasqua, M.; Frisch, M. J.; Larkin, S. M.; Morrison, M.; Robb, M. A. *Journal of Photochemistry and Photobiology A: Chemistry* **2007**, *190*, 207–227.
- 66 Meyer, H.-D.; Pelaez-Ruiz, D. Introduction to MCTDH, lecture notes. http://www.pci.uni-heidelberg.de/tc/usr/mctdh/lit/intro_MCTDH.pdf, 2011, Revised 2014.
- 67 Meyer, H.-D.; Manthe, U.; Cederbaum, L. S. *Chemical Physics Letters* **1990**, *165*, 73–78.
- 68 Manthe, U.; Meyer, H.-D.; Cederbaum, L. S. *The Journal of chemical physics* **1992**, *97*, 3199–3213.
- 69 Beck, M. H.; Jäckle, A.; Worth, G.; Meyer, H.-D. *Physics reports* **2000**, *324*, 1–105.
- 70 Wang, H.; Thoss, M. *The Journal of chemical physics* **2003**, *119*, 1289–1299.
- 71 Frisch, M. J. et al. Gaussian development version Revision h.13. Gaussian Inc. Wallingford CT 2009.
- 72 Bearpark, M. J.; Larkin, S. M.; Vreven, T. *The Journal of Physical Chemistry A* **2008**, *112*, 7286–7295.
- 73 others,, et al. *The Journal of Physical Chemistry C* **2007**, *111*, 2287–2294.
- 74 Sussman, B. J.; Townsend, D.; Ivanov, M. Y.; Stolow, A. *Science* **2006**, *314*, 278–281.
- 75 Townsend, D.; Sussman, B. J.; Stolow, A. *J. Phys. Chem. A* **2011**, *115*, 357–373.

- 76 Chang, B. Y.; Shin, S.; Santamaria, J.; Sola, I. R. *The Journal of chemical physics* **2011**, *134*, 144303.
- 77 Chang, B. Y.; Choi, H.; Shin, S.; Lee, S.; Solá, I. R. *Journal of Modern Optics* **2009**, *56*, 811–821.
- 78 Marquetand, P.; Engel, V. *Physical Chemistry Chemical Physics* **2005**, *7*, 469–474.
- 79 Scheit, S.; Arasaki, Y.; Takatsuka, K. *The Journal of Physical Chemistry A* **2011**, *116*, 2644–2653.
- 80 Belz, S.; Zilberg, S.; Berg, M.; Grohmann, T.; Leibscher, M. *The Journal of Physical Chemistry A* **2012**, *116*, 11189–11198.
- 81 Richings, G. W.; Worth, G. A. *The Journal of Physical Chemistry A* **2012**, *116*, 11228–11240.
- 82 Williams, T.; Kelley, C.; many others, Gnuplot 4.4: an interactive plotting program. <http://gnuplot.sourceforge.net/>, 2010.
- 83 Blancafort, L.; Gatti, F.; Meyer, H.-D. *The Journal of chemical physics* **2011**, *135*, 134303.